

**Functionalization of brush-like polymer modified  
surfaces by scanning probe lithography for biological  
screening applications**

Zur Erlangung des akademischen Grades eines

**DOKTORS DER NATURWISSENSCHAFTEN**

(Dr. rer. nat.)

von der KIT-Fakultät für Chemie und Biowissenschaften

des Karlsruher Instituts für Technologie (KIT)

genehmigte

**DISSERTATION**

von

M.Sc. Bingquan Yang

Dekan: Prof. Dr. Hans-Achim Wagenknecht

Referent: PD Dr. Dr. Michael Hirtz

Korreferentin: Prof. Dr. Annie Powell

Tag der mündlichen Prüfung: 19.07.2022



## Acknowledgements

As time goes by, I have spent four years in Germany, and now it's time to finish my PhD at KIT. During my life at KIT in Karlsruhe, I have learned many new techniques and knowledge as well as made many friends. I will never forget the people I have met, the roads I have walked and the view I have seen here. The wonderful life I have experienced here will go deep into my heart forever.

I would like to express my heartfelt thanks to my supervisor, PD. Dr. Dr. Michael Hirtz, who gives me the opportunity to work in the group of Scanning Probe Lithography for Biomaterials and Bioelectronics under his guidance. He always provides me with a neat working space and vest freedom in terms of my research work at INT. I appreciate that Michael is always open in mind to question discussion. His passion and enthusiasm for research inspire me to bravely go through the tough jungle and reach the side of success. Michael is the best supervisor I have ever had so far. His fruitful knowledge and constructive ideas assist me in establishing the frame of my PhD project. Honestly, there would be no possibility of finishing my doctoral work without Michael's great support and kind help. Thank you very much, Michael!

Furthermore, I would like to give my sincere gratitude to Prof. Annie K. Powell, who has helped me a lot during my study at KIT. She is knowledgeable and has a rigorous attitude toward scholarship and kind and friendly nature. I really appreciate that she has shown high interest in my doctoral work. The time spent with her was amazing and enjoyable. Thank you very much, Annie!

Especially my sincere gratitude would go to Dr. Ravi Kumar. Ravi is a kind and friendly person. In spite of his busy schedule, he is always available for discussions and suggestions. I will never forget that it was Ravi who taught me how to use the machines at INT and who guided me in my first experiment at INT. Additionally, he helped me a lot not only in my work but also in my life. Thank you, Ravi!

I would like to give my sincere thanks to Dr. Kristina Riehemann and Prof. Harald Fuchs, who gave me great help when I was in Muenster and taught me the protocol of macrophage isolation and culture. I also owe my appreciation to Dr. Sylwia Sekula-Neuner, who helped

me a lot in bio-experiments and bio-staffs. Furthermore, I want to express my gratitude to Dr. Cesar Rodriguez-Emmenegger, Mariia Vorobii and Dr. Yangxin Wang, without their help, it would be really hard to synthesize the antifouling polymer brushes.

I would like to acknowledge my lab-mates and colleagues at INT. And we had a great and unforgettable time at INT. Thank you, Dr. Eider Berganza Eguiarte, Dr. Mahdi Dadfar, Dr. Hui-Yu Liu, Dr. Ravi Kumar, Navid Hussain, Chunting Zhong, Wenwu Yang, Srivatsan K. Vasantham, Mohammad Jan Nazami. The time spent with you was great fine, and hopefully, we can meet or work together in the future in some places.

I would like to express my thanks to all my collaborators at KIT for their help in my work and life. My special appreciation would go to Dr. Simone Dehm and Dr. Uwe Bog for instrument instructions. I appreciate my great thanks to Dr. Andreas Schäfer and Dr. Eric Sauter, who helped me with the XPS measurements.

I would like to give my gratitude to my parents and thank them for giving me the freedom to accomplish my dream. Without their support, I couldn't complete my PhD.

At last, I would like to acknowledge China Scholarship Council (CSC), and thanks for giving me the opportunity to go abroad and funding me for my doctoral project. Moreover, I also thank Karlsruhe House of Young Scientist (KHYS) for granting me to visit ETH in Switzerland.

## Zusammenfassung

In dieser Dissertation werden verschiedene Oberflächenmodifizierungsverfahren zusammen mit der Oberflächenkontaktlithografie (microchannel cantilever spotting,  $\mu$ CS) eingesetzt, um verschiedene Biochips für Biosensoren und biomedizinische Anwendungen zu entwickeln. Zu diesem Zweck werden Glasobjektträger zunächst mit verschiedenen funktionellen Einheiten modifiziert, z. B. mit einer selbstorganisierten Monoschicht (self-assembled monolayer, SAM) aus Alkinen und Polymerbürsten mit reaktiven Epoxid- oder Azidgruppen, die durch "grafting to" bzw. "grafting from" Verfahren hergestellt werden. Darauf folgend werden verschiedene molekulare Tinten mittels  $\mu$ CS auf die Chips strukturiert und verschiedene Tinten-Substrat-Kombinationen (Click-Reaktionen zwischen ihnen) demonstriert. Zudem wird die Effizienz in Bio-Screening und die Bio-Detektion durch Fluoreszenzbildgebung bewertet.

Um die Bindungseffizienz von Cyclooctinazid auf einfache und bequeme Weise zu bewerten, wurden in dieser Doktorarbeit verschiedene DBCO/BCN-Derivate, die entweder mit einem Fluorophor oder einer Biotin-Komponente verknüpft sind, mittels Rastersondenlithographie (scanning probe lithography, SPL) auf azid-tragenden Antifouling-Polymerbürsten (AAPBs) strukturiert. Die AAPBs bestehen aus zwei Bausteinen, einem Antifouling-Bodenblock, der unspezifische Proteinkontaminationen während der Inkubation auch ohne vorherige Blockierungsschritte vermeiden kann, und einem azid-funktionalisierten Oberblock, der über SPAAC-Reaktionen (strain-promoted azide-alkyne cycloaddition) an Alkine binden kann. Die Bewertung der Bindungseffizienz wird auf geordneten Arrays mit einem regulären Fluoreszenzmikroskop durchgeführt. Beide Cyclooctine zeigen eine zuverlässige Bindungsleistung mit AAPBs auf SPL-funktionalisierten Flächen. DBCO zeigt jedoch eine höhere Oberflächendichte der molekularen Immobilisierung gemäß den Proteinbindungsversuchen. Allgemein können diese Ergebnisse als Anleitung für die Auswahl geeigneter Cyclooctyne zur Kopplung mit Aziden dienen, welche für das Design von Biosensoren oder Bio-Plattformen nützlich sein kann.

Im Weiteren, wurde zudem ein neuartiger und einfacher fluoreszenz-basierter Immunosensor für die direkte Bestimmung von  $\alpha$ -Fetoprotein (AFP) zur Diagnose des hepatozellulären Karzinoms (HCC) entwickelt. Hierfür wurden DBCO-NHS-Ester-Arrays, die für die Verankerung von AFP-Antikörpern durch kovalente Amidbindungen (direkte Bindungsstrategie) verwendet werden, mittels SPL auf AAPBs strukturiert. Die DBCO-NHS-Arrays binden sanft und effizient durch SPAAC-Reaktion an AAPBs, gefolgt von der Aufnahme von Anti-AFP durch eine spezifische und direkte Bildung von Amidbindungen (NHS/Amino) zum Nachweis von fluoreszenzmarkiertem AFP. Die Ergebnisse zeigen, dass die direkte Strategie (NHS/Antikörper/AFP) für den AFP-Nachweis gut funktioniert und sogar empfindlicher ist als die indirekte Strategie (Biotin/Streptavidin/Biotin/Antikörper/AFP), was möglicherweise auf den kompakten Herstellungsprozess zurückzuführen ist. Insgesamt zeigt der vorgeschlagene kostengünstige und zuverlässige Fluoreszenz-Immunosensor ein ausgeprägtes Potenzial für klinische und diagnostische Anwendungen zum AFP-Nachweis.

Diamant-verwandte Materialien mit Autophotolumineszenz sind mittlerweile ein wesentliches Instrument bei der Konstruktion von Biosonden und Biosensoren für die Fluoreszenzbildgebung. Die Diamantoberfläche ist jedoch anfällig für Verunreinigungen durch biologische Medien und Makromoleküle in komplexen Proben oder sogar lebenden Systemen, was die Fluoreszenzemission beeinträchtigt und zu einem geringeren Signal-zu-Rauschen-Verhältnis führt, mit eingegrenzter Limitation der Anwendungen. Eine neue proteinabweisende und klickbare reaktive Polymerbürste wurde entwickelt, um die unspezifische Proteinadhäsion zu beseitigen und die Immobilisierung von mit spezifischen Erkennungselementen und/oder Fluorophoren verbundenen Verbindungen zu ermöglichen. Die Polymerbürsten bestehen aus zwei verschiedenen Segmenten, einem Antifouling-Segment aus Poly(N-(2-hydroxypropyl)-methacrylamid) (HPMA) und einem Segment aus Poly(propargylacrylamid) (AlkMA) mit Alkin-Endgruppen, welches die Klick-Funktionalität bereitstellt. Die Antifouling-Eigenschaften und die klickbare Reaktivität der Polymerbürsten werden mit selektiven Proteinbindungsassays auf mit  $\mu$ CS geschriebenen Mikromustern nachgewiesen. Es wird demonstriert, dass sich die Polymerbürste erfolgreich an die Diamantoberfläche anlagert und die (ungewollte) Proteinanhaftung effizient hemmt, wodurch das Signal-zu-Rauschen-Verhältnis verbessert wird.

In-vitro-Studien über Gen-Editierung und -Expression sind in hohem Maße von DNS-Mikrochips abhängig. Jedoch sind herkömmliche Chips teuer und anspruchsvoll. Hierbei beeinflussen unter anderem die Oberflächeneigenschaften von DNS-Biochips die allgemeine Effizienz der DNS-Hybridisierung. Daher wurden im Rahmen dieser Dissertation drei reaktive Substanzen mit unterschiedlicher Oberflächentopographie und -zusammensetzung für die Konstruktion von DNS-Sensorplattformen untersucht: Goldbeschichtetes Silizium, mit Poly(bisphenol A-co-epichlorhydrin) (PBAG) modifizierte Substrate und SAMs aus DBCO-funktionalisierten Objektträgern. Die gezielte DNS-Immobilisierung in Verbindung mit SPL bietet eine kostengünstigere und leichter zugängliche Möglichkeit zur Herstellung von Sonden-Mikroarrays, die sich leicht mit einem Mikroskop auslesen lassen. Alle drei Plattformen zeigen eine zuverlässige Fähigkeit zur DNS-Detektion, aber die Proteinbindungsassays zeigen, dass die DNS-Hybridisierung auf der mit PBAG modifizierten Oberfläche eine höhere Effizienz aufweist. Die Ergebnisse haben erhebliche Auswirkungen auf das Verständnis der Wechselwirkungen zwischen der DNS-Hybridisierungseffizienz und den Oberflächeneigenschaften von Substraten sowie auf die Herstellung von DNA-Biosensoren mit hohem Durchsatz.

## Abstract

In this dissertation, different surface modification techniques are employed in combination with microchannel cantilever spotting ( $\mu$ CS) to design different biochips for bioscreening and biomedical applications. For these purposes, glass slides are modified with different functional moieties, e.g., self-assembled monolayer (SAM) of alkyne and polymer brushes bearing clickable reactive groups fabricated by “grafting to” or “grafting from” approaches. Furthermore, different inks are patterned to the chips via  $\mu$ CS, and different ink-substrate combinations (click reactions in between them) are demonstrated, as well as the bio-screening and bio-detection are evaluated by fluorescent imaging.

To easily and conveniently evaluate the binding efficiency of cyclooctyne/azide, different derivatives of DBCO/BCN (dibenzocyclooctyne/bicyclononyne) linked to either a fluorophore or a biotin-moiety are patterned on azide-bearing antifouling polymer brushes (AAPBs) via  $\mu$ CS. The AAPBs are composed of two building blocks, an antifouling bottom block, which can avoid unspecific protein contamination during incubation without any advancing blocking steps; and an azide functionalized top block, which can bind to alkynes via strain-promoted alkyne-azide cycloaddition (SPAAC) reactions. The assessments of binding efficiency are conducted on ordered arrays with a standard fluorescent microscope. Both cyclooctynes demonstrate reliable binding performance with azide moieties at  $\mu$ CS patterned area, but DBCO shows a higher surface density of molecular immobilization according to the protein binding assays. Herein, we provide a reference for choosing appropriate cyclooctyne to couple with azides that can be useful for the design of biosensors or bio-platforms.

A novel and facile fluorescent immunosensor is designed by direct anchoring of antibodies for the determination of  $\alpha$ -fetoprotein (AFP) for diagnosis of hepatocellular carcinoma (HCC). DBCO-NHS ester capture arrays, which are used for anchoring AFP-antibody through covalent amide bonds (direct binding strategy), are patterned on AAPBs by  $\mu$ CS. The DBCO-NHS ester arrays can mildly and efficiently bind to AAPBs via SPAAC reaction followed by grabbing anti-AFP via forming of amide bonds (HNS/amino) for detection of fluorescently labeled AFP specifically and directly. For comparison,

DBCO-Biotin is spotted on AAPBs to construct sandwich structures (biotin/streptavidin/biotin-antibody) for AFP detection (indirect binding strategy). The results show that the direct and indirect strategies both work well for AFP detection, and also provide that the direct strategy (NHS/antibody/AFP) is more sensitive than the indirect strategy (biotin/streptavidin/biotin-antibody/AFP), which is perhaps benefitting from the compact fabrication process of the direct strategy. Overall, the proposed cost-effectively and reliably fluorescent immunosensor exhibits great potential in clinical and diagnostic applications for AFP detection.

Diamond-related materials with auto-photoluminescence are an essential tool in the construction of bioprobes and biosensors in fluorescence imaging. However, the diamond interface is susceptible to contamination by biological media or macromolecules in complex samples or even living systems, thus impairing its emission of fluorescence and leading to a low signal-to-noise ratio, broadly limiting applications. A new protein-repellent and clickable reactive polymer brush is designed to abolish unspecific protein adhesion and enable immobilization of recognition-element and fluorophore-linked compounds. The polymer brushes have two different segments, an antifouling poly(N-(2-hydroxypropyl)-methacrylamide) (HPMA) segment and an alkyne terminated poly(propargylacrylamide) (AlkMA) segment providing the click-functionality. The antifouling properties and clickable reactivity of the polymer brushes are demonstrated with selective protein binding assays on micropatterns written by  $\mu$ CS. Significantly, the polymer brush is successfully attached on the diamond surface and efficiently inhibits protein pollution, improving the signal-to-noise ratio.

In-vitro studies, gene editing and expression are highly dependent on DNA microchips, however, conventional chips require sophisticated and expensive manufacturing processes. The surface characteristics of DNA biochips generally affect the DNA hybridization behaviors. Therefore, three reactive substances possessing different surface topographies and compositions are involved in construction DNA sensing platforms, namely, gold-coated silicon, poly(bisphenol A-co-epichlorohydrin) (PBAG) grafting polymer, and SAM of DBCO-functionalized slides. Herein, DNA directed-immobilization (DDI) together with  $\mu$ CS offers a cheaper and more accessible way to construct DNA probe microarrays, which

can be easily read out with a fluorescent microscope. All of these three platforms behave a reliable ability for DNA detection, but the PBAG-modified surface exhibits a higher hybridization efficiency either at a short probe (22mer) hybridized with a short target (22mer) system or at two short targets (both are 22mer) hybridized with a long probe sequence (44mer) system. The results have significant implications for better understanding of the interactions between the DNA hybridization efficiency and the surface properties of substrates and inform the fabrication of high-throughput DNA biosensors.

## Contents

<b>Acknowledgements</b> .....	I
<b>Zusammenfassung</b> .....	III
<b>Abstract</b> .....	VI
<b>Contents</b> .....	IX
<b>Chapter 1 – Introduction</b> .....	1
1.1 Approaches for surface modification .....	1
1.1.1. Self-assembled monolayers (SAMs) .....	3
1.1.2. Polymer-based modifications .....	5
1.2. Fouling phenomena and polymer-based antifouling strategies .....	6
1.2.1. General concept of fouling phenomena .....	6
1.2.2. Approaches and mechanisms of anti-biofouling .....	7
1.2.3. Surface grafting strategies of polymer brushes .....	11
1.3. Brief review of click chemistry .....	12
1.4. Scanning probe lithography (SPL) .....	16
1.5. Thesis objectives and overview .....	19
<b>Chapter 2 – Screening of high-efficient cyclooctyne on azide-bearing antifouling polymer brushes (AAPBs)</b> .....	22
2.1. Introduction .....	22
2.2. Results and discussions .....	25
2.2.1. Physical and chemical characterization of the polymer brushes .....	25
2.2.2. Antifouling property characterization .....	31
2.2.3. Fluorescent inks patterning for printing and reaction parameters test .....	32
2.2.4. Protein binding on DBCO- and BCN-Biotin arrays .....	38
2.3. Summary .....	41
<b>Chapter 3 – A fluorescent immunosensor for <math>\alpha</math>-fetoprotein (AFP) detection</b> .....	42
3.1. Introduction .....	42
3.2. Results and discussions .....	45
3.2.1. Immobilization of DBCO-derivative capture arrays on AAPBs .....	45

---

3.2.2. Construction of antibody arrays .....	45
3.2.3. Detection of fluorescently labeled AFP .....	47
3.2.4. Sensitivity evaluation of the immunosensor .....	50
3.3. Summary .....	52
<b>Chapter 4 – Signal-to-noise ratio improvement on diamond surfaces in fluorescence imaging by methacrylate-based polymer brush coating .....</b>	<b>53</b>
4.1. Introduction .....	53
4.2. Results and discussions .....	55
4.2.1. Evaluation of antifouling properties and reactivity of the polymer brushes ...	55
4.2.2. Evaluation of antifouling properties and reactivity of the polymer brushes ...	59
4.2.3. Applying the polymer brush coatings to diamond surface .....	66
4.3. Summary .....	69
<b>Chapter 5 – Fabrication of different sensing platforms for DNA hybridization .....</b>	<b>70</b>
5.1. Introduction .....	70
5.2. Results and discussions .....	73
5.2.1. Characterization of the sensing platforms .....	73
5.2.2. DNA hybridization on different platforms .....	78
5.2.3. Protein binding assay on hybridized DNA patterns .....	83
5.3. Summary .....	86
<b>Chapter 6 – Thesis summary and outlook .....</b>	<b>87</b>
<b>Chapter 7 – Experimental section .....</b>	<b>90</b>
7.1. Materials and chemicals .....	90
7.2. Equipments for experiment .....	93
7.2.1. Patterning by microchannel cantilever spotting ( $\mu$ CS) .....	93
7.2.2. Water contact angle (WCA) .....	93
7.2.3. Film thickness measurement .....	93
7.2.4. Atomic force microscopy (AFM) .....	94
7.2.5. X-ray photoelectron spectroscopy (XPS) .....	94
7.2.6. Fluorescent microscopy .....	94
7.3. Experimental methods .....	95

---

7.3.1. Screening of high-efficient cyclooctyne on azide-bearing antifouling polymer brushes (AAPBs) .....	95
7.3.2. A fluorescent immunosensor for $\alpha$ -fetoprotein (AFP) detection .....	97
7.3.3. Signal-to-noise ratio improvement on diamond surfaces in fluorescence imaging by methacrylate-based polymer brush coating .....	99
7.3.4. Fabrication of different sensing platforms for DNA hybridization .....	100
<b>References</b> .....	103
<b>Appendix</b> .....	118
Appendix A: List of abbreviations .....	118
Appendix B: List of figures .....	121
Appendix C: List of tables .....	131

## Chapter 1 – Introduction

### 1.1. Approaches for surface modification

Normally, people desire materials not only to possess excellently physical or chemical properties in bulk aspects but also with appropriate surface performances to meet some special requirements, especially in biological applications, e.g. bio-sensing, bio-screening, tissue engineering, and drug delivery.<sup>[1]</sup> However, it is rare that a pristine material shows excellent properties in bulk and on the surface simultaneously. Surface modification is one of the best choices for manipulating materials, such as enhancing their surface properties or introducing novel functions, therefore widespread in many fields (Figure 1.1), e.g., antifouling,<sup>[2, 3]</sup> antibacterial,<sup>[4, 5]</sup> cell manipulating,<sup>[6, 7]</sup> DNA immobilization,<sup>[8, 9]</sup> biosensors,<sup>[10]</sup> and anymore.<sup>[11-13]</sup>

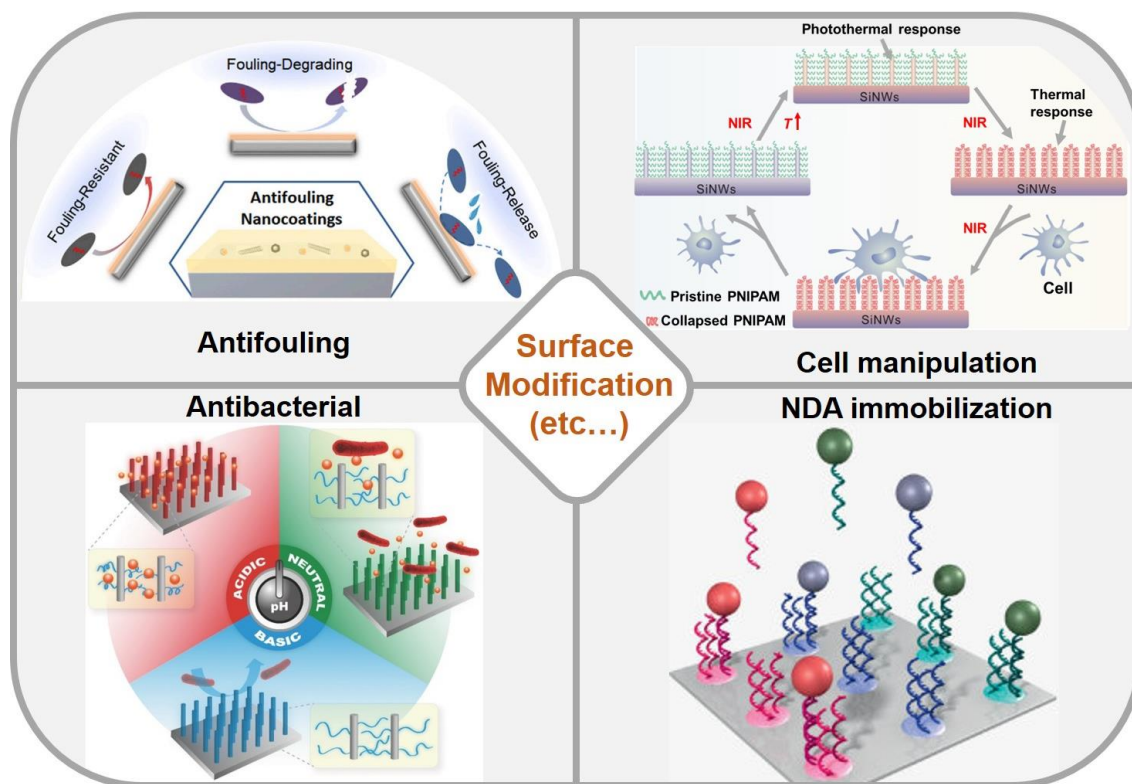


**Figure 1.1.** Applications of modified surfaces.

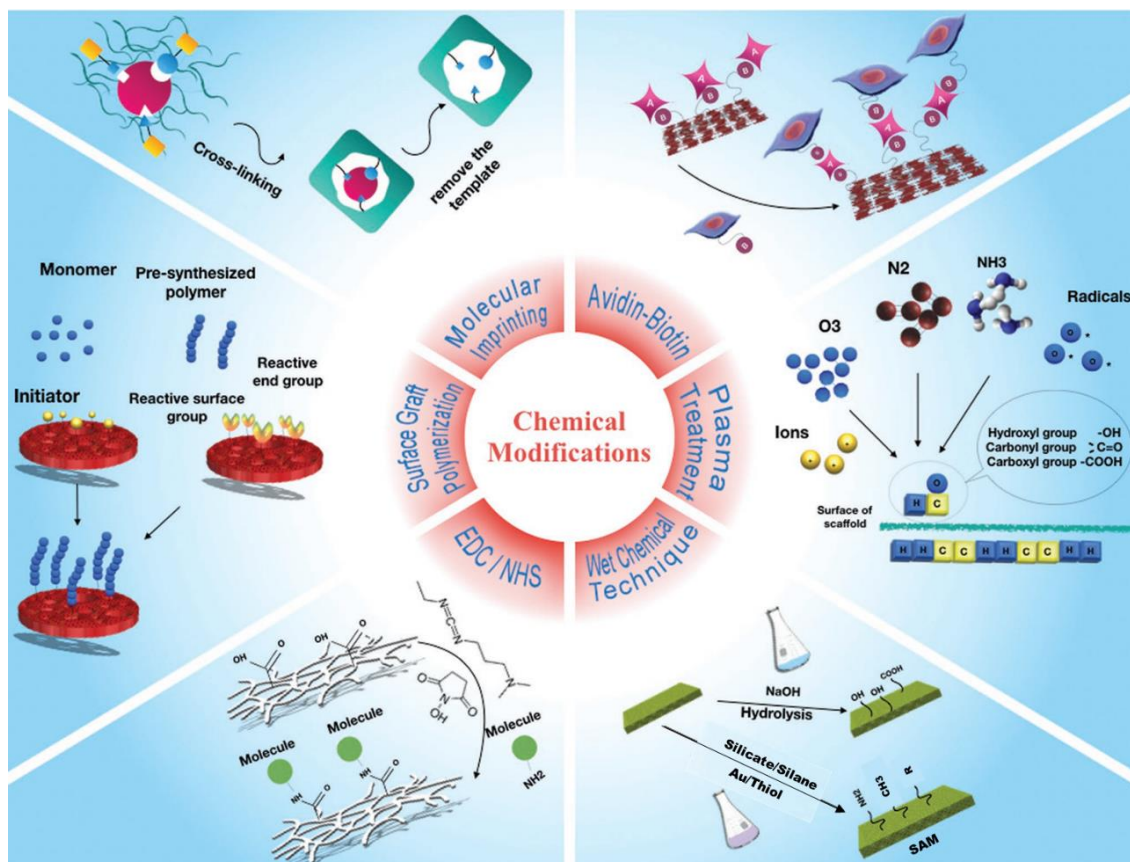


**Figure 1.2.** Schematic representation of different chemical modification techniques for surface characteristics modulation.<sup>[14]</sup>

Surface modification is defined as a process that surface morphology, structure, and composition of material would be changed after coating or modifying the surface by using chemical, physical or biological techniques, but remaining its bulk properties.<sup>[14-16]</sup> Chemical modification involves introducing molecules or materials via forming of chemical bonds on interfaces and endowing desirably reactive groups.<sup>[17, 18]</sup> Physical methods always depend on mechanical grinding or mixing, radiation, and ultrasonication to prepare composite materials.<sup>[15]</sup> Biological modifications usually do not refer to toxic reagents or harsh conditions, e.g., enzymatic linking,<sup>[19]</sup> but limit their applications, therefore.<sup>[20]</sup> Among these techniques, chemical modification has attracted much attention in many fields, due to its durability, stability, extensive application, and biocompatibility.<sup>[14, 21-23]</sup> More precisely, in biological studies, chemical modification techniques usually are employed to introduce biomolecules or bio/nanomaterials onto the interface of substrates

through grafting functional moieties (silanization or grafting polymer brushes) or changing existing functional species (substitution or oxidation or reduction) (**Figure 1.2**).<sup>[14, 24]</sup>

In this thesis, the work was implemented based on self-assembled monolayers and polymer brushes, therefore this brief introduction of modification approaches is mainly focusing on these two aspects.

### 1.1.1. Self-assembled monolayers (SAMs)

Molecular self-assembly from a liquid phase, e.g., self-assembled monolayers (SAMs), as a popular wet chemical method for surface modification is facile and allows the integration of biological and organic components to achieve a variety of biological functions.<sup>[25, 26]</sup> Generally, SAMs are a class of two-dimensional nanomaterials formed by chemical modification on various solid-phase interfaces.<sup>[27, 28]</sup> The SAMs consist of densely assembled molecules which usually bear functional groups at the terminal, e.g. –NH<sub>2</sub>, –SH, –CH<sub>3</sub>, epoxy, alkene, alkyne, and more,<sup>[27, 29, 30]</sup> thus changing the morphology in microscale or nanoscale as well as tailoring the surface composition and properties. Therefore, SAMs are broadly applied in sensors,<sup>[31]</sup> electronics,<sup>[32]</sup> tribology,<sup>[33]</sup> and antifouling surfaces.<sup>[34]</sup>

There are two classes of commonly used SAM systems, silanization-based agents and thiolation-based agents, and the representative surface modification processes of these two regimes are shown in Figure 1.3. The thiol-containing molecules are usually used on gold-coated surfaces by forming Au–S bonds.<sup>[35, 36]</sup> However, metal-based surfaces can emit plasmon, which has considerable influence on fluorophores and even quenches them. Therefore, the thiol/gold systems are rarely used in fluorescent imaging or detection. Compared to the sulfur-containing monolayers, the silane-based molecules normally assemble to silicate interfaces, e.g., glass and silicon oxide materials, which are less expensive and commonly used in optics and electronics.<sup>[37]</sup> Moreover, to get densely packed SAMs, the silicate surfaces need to be hydroxylated as pretreatment, which aim is to seed silanol groups on the surface and then introduce silane coupling agents to form SAMs.<sup>[27]</sup> The driving force of surface silanization is the in situ generation of polysiloxane, which has the ability to link the surface silanol groups (–SiOH) via Si–O–Si bonds or even self-polymerize between adjacent molecules.<sup>[27]</sup> Frequently, the silane-based monolayers

are more stable and durable due to the employed agents being equipped with di- or tri-valent anchoring units (e.g., trichloro-, trimethoxy-, or triethoxysilanes), which can result in a lateral polymerization of the molecular networks attached to the surface and enhance the stability of the monolayers.<sup>[27]</sup> Besides, a few other SAM anchoring moieties have been developed and used for some special conditions including phosphates, carboxylates, catechols, alkenes, and alkynes, and more (Figure 1.4).<sup>[37]</sup>

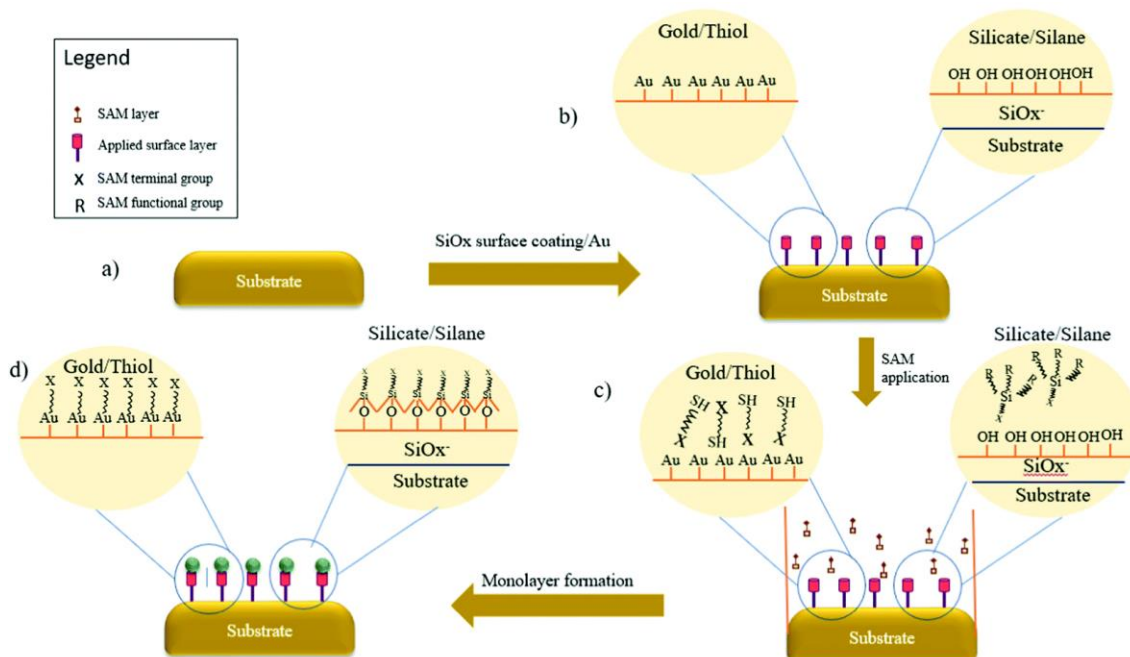


**Figure 1.3.** Schematic drawing of SAMs forming with various reactive terminals.<sup>[25]</sup> a) Substrate selection, b) substrates pre-treatment, coating with gold or hydroxylation, c) self-assembled process, d) formed SAMs.



## 1.2. Fouling phenomena and polymer-based antifouling strategies

### 1.2.1. General concept of fouling phenomena

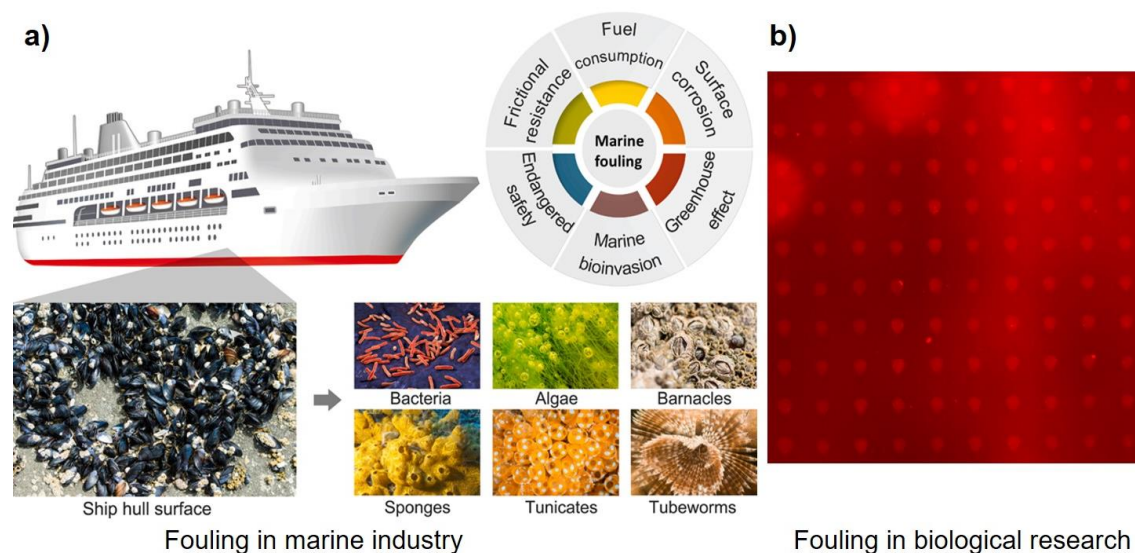


**Figure 1.5.** a) Schematic representations of different biofouling and their adverse effects on the marine industry.<sup>[39]</sup> b) Unspecific protein (streptavidin-Cy3) fouling on glass slides, the dot spots are the target area, and the other area are fully covered with the fouling protein (showing in red color).

In real life or research, contaminants are everywhere, materials from the environment in micro- or nano-scales, e.g., small creatures, microorganisms, particles, proteins, macromolecules, and other impurities adsorb to a surface actively or passively and then negatively impact the stability and functionality of the surface, these unwanted contaminants are commonly called fouling.<sup>[40-42]</sup> In shipping industry, some small marine creatures, e.g., bacteria, fungus, alga, and shellfish prefer to adhere to the ship hull, which would increase corrosion and fuel consumption, and accelerate the greenhouse effect (Figure 1.5a).<sup>[43]</sup> Data shows that the related marine industries have to spend at least US \$ 15 billion annually on the biofouling issues.<sup>[39]</sup> Moreover, additional fuel consumption would produce more greenhouse gases, which are the primary global warming sources. In biology and healthcare applications, for example, in bio-sensing processes (Figure 1.5b), unspecific protein fouling can cause high background or low signal-to-noise ratio which then affect the determination of final results; as well as fouling increases health risks, such

as inducing the spread of infectious diseases and bacterial attachment and colonization, and raising rates of implant rejection.<sup>[39]</sup> Therefore, fouling is a global problem in various fields that needs endeavors from all over the world to find meaningful manners for eliminating or impairing it.

### **1.2.2. Approaches and mechanisms of anti-biofouling**

Virtually, since the fouling issues were noticed by human beings, the study of antifouling or self-cleaning technics has never ceased. After centuries of development and deep understanding of the fouling process, researchers found that the fouling highly depends on the surface properties, such as microtexture, wettability, and surface energy.<sup>[40, 44, 45]</sup> Hence, plenty of antifouling strategies based on changing of surface characteristics by film coatings have been proposed including surface topography construction (e.g., micro- or nano-structures),<sup>[39, 46]</sup> surface chemistry modification (e.g., SAMs or grafting polymers),<sup>[2, 47]</sup> biological modification (e.g., inert proteins, enzyme-based agents),<sup>[48]</sup> metal coatings (e.g., Cu and Pb),<sup>[40]</sup> hybrid coatings,<sup>[49]</sup> and many more.<sup>[50]</sup> Normally, these kinds of coatings can be classified into three categories, i.e., fouling resistant, fouling release, and fouling degrading (Figure 1.6).<sup>[3]</sup> Fouling resistant involves coatings including PEGylated and zwitterionic polymer brushes, which have the ability to form a hydration layer or eliminate charge accumulation on the surface and by this prevent the adhesion of proteins or molecules.<sup>[51, 52]</sup> Fouling release coatings usually permit weak adhesion of the pollutants that are easily removed or cleaned by external forces. This class includes, e.g., silicones, fluoropolymers, and other hydrophobic or amphiphilic coatings.<sup>[53, 54]</sup> While, fouling degrading coatings achieve their antifouling properties through degrading or killing of the organic foulants when they try to approach the functionalized surfaces, e.g, antimicrobial peptides and quaternary ammonium polymers.<sup>[4, 55, 56]</sup> Biocidal coatings especially can kill organisms by destroying their cell membranes and degrading their secreted bio-adhesive, or even damaging the extracellular matrix.<sup>[57]</sup> Thus biocidal coatings are widely used in food packaging and marine shipping.

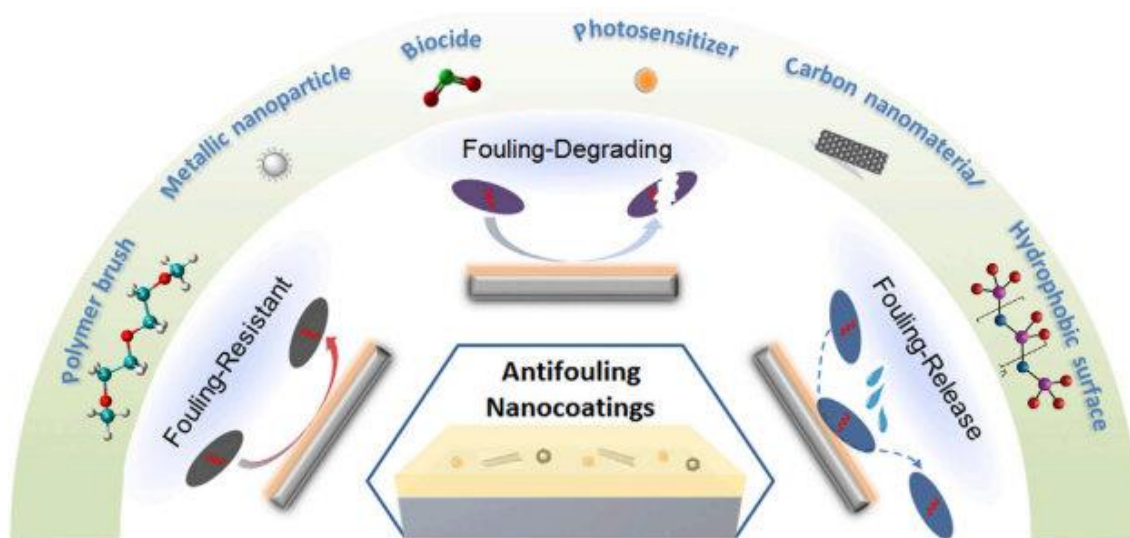


**Figure 1.6.** Schematic drawing of the three main antifouling strategies.<sup>[3]</sup>

The earliest antifouling coatings are metal-based systems, e.g., copper-, silver-, lead-, and mercury-based, which have been applied for centuries, while due to the toxicity and pollution of the environment with these heavy metals, they have been already banned worldwide.<sup>[58]</sup> Moreover, due to indiscriminate sterilization of the biocidal coatings, any organisms would be killed at the surface either useful or harmful, and in some cases, the dead microbial debris might serve as a breeding ground for microorganism colonization.<sup>[59]</sup> Therefore, it is indispensable to develop environmentally friendly solutions to create non-toxic or low-toxic antifouling coatings, especially in healthcare and clinic applications. In recent decades, polymer-based antifouling resistant coatings have exhibited pronounced advantages in resisting biofouling, due to them being ecofriendly, biocompatible, durable, and facile to process. Polymer brushes are a layer of polymers on material interfaces, which can be created in a few nanometers thickness, transforming the nature of materials synchronously.<sup>[60]</sup> Furthermore, their interfacial characteristics, as well as the antifouling properties, are easily manipulated via tuning of interior architectures or surface terminals.

In clinical applications, the main reason for foulants adhesion is protein dehydration, which can be ascribed to the declined energy barrier between proteins and materials.<sup>[48]</sup> More specifically, the closely approaching between protein and material surface would induce discharging of water molecules, thus reducing the energy barrier and then leading to dehydration of protein and resulting biofouling finally.<sup>[61]</sup> Practically, using blocking

agents (e.g., bovine serum albumin, fetal bovine serum, goat serum, and casein) is a common way to resist nonspecific protein fouling in biological research.<sup>[48, 62]</sup> It is generally assumed that these inert proteins function to prevent further adsorption only after they occupy the unreactive space entirely and resulting in an interface resembling an anti-metamorphic system.<sup>[63]</sup> However, in some cases, the efficiency of the specific receptors or the reactive sites needed to do post-treatment would be impaired by these proteins, and they can even cause undesired responses on their own. Therefore, a platform carrying fouling repellency while bearing simultaneously functional moieties to allow the covalent bonds would be highly desirable. In this condition, the focus has mainly shifted toward polymer-based antifouling coatings, as they are biocompatibility, ease to customize and process, non-toxic, and exhibit excellent antifouling properties. Practically, polymer brushes as a material class refers to geometry structures in which polymer chains are densely and tightly tethered to surfaces by one terminal and perpendicularly stretching out, therefore tailoring the physicochemical properties of the surfaces as well as the antifouling properties.<sup>[64]</sup> As shown in Figure 1.7, the possible mechanisms of repelling unspecific protein adsorption by polymer brushes can be classified into four categories, i.e., forming of hydration layer, electrostatic repulsion, steric repulsion, and constructing of micro/nano-topography.<sup>[2]</sup>

The hydration layer theory is also known as the water barrier principle. In real examples, the hydrophobic interaction is a factor in fouling generation. In this respect, studies attempt to structure hydrophilic interfaces to avoid hydrophobic interactions and impair fouling tendency.<sup>[2]</sup> On a hydrophilic surface, the water molecules would severely compete to foulants and then form a water barrier on the surface which hinders the fouling through dehydration mechanisms.<sup>[65]</sup> The formed hydration layer between proteins and substances plays an important role in the mechanism of antifouling, therefore, the hydration ability of the polymer coatings normally is regarded as a key performance indicator to evaluate the antifouling properties of the material. Relying on this theory the polyethylene glycol (PEG) based polymer brushes are incorporated on material interfaces to attain antifouling characteristics.<sup>[66]</sup> Remarkably, the PEGylated brushes are normally deemed as a class of gold standard interfaces for resisting the adsorption of numerous proteins. PEG combines

almost all the general advantages of the polymer-based coatings, such as non-toxicity, water-solubility, biocompatibility, low immunogenicity, and facile processing.<sup>[40]</sup>

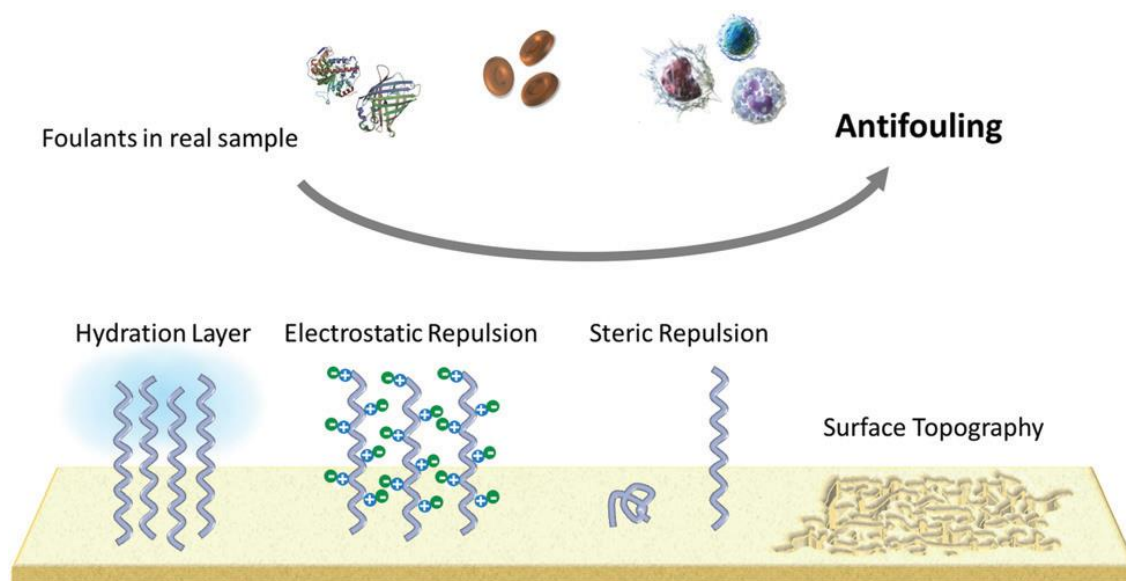


**Figure 1.7.** Schematic mechanisms of protein repellency of polymer-based antifouling coatings.<sup>[2]</sup>

Zwitterionic polymers, such as phosphocholine, sulfobetaine, and carboxylbetaine, contain an equal number of opposite charges and exhibit excellent anti-contamination behaviors.<sup>[65, 67, 68]</sup> Commonly, ions in aqueous situation would be charging and accumulating on the surface of the material which then accepts foulants charged oppositely. While, zwitterionic materials usually configure into neutral coatings on interfaces because the equivalent cationic and anionic species both exist in their backbones,<sup>[69, 70]</sup> thus avoiding charge aggregation and electrostatic attraction to charged proteins, and thereby enabling antifouling properties.<sup>[71]</sup>

As of our knowledge, steric repulsion is usually not regarded as an individual principle to explain antifouling mechanisms.<sup>[49, 72]</sup> Commonly, it suits for some polymers containing long chains, e.g., some bottlebrushes, while many water-soluble polymers have the ability to form a hydration layer and show steric repulsion simultaneously.<sup>[49, 73]</sup> Detailedly, when pollutants try to approach a polymer surface, the flexible long chains in the polymer scaffold would be compressed and generate steric repulsion, therefore exhibiting anti-pollution effects.<sup>[40, 66]</sup> As the thickness and length of polymer chains determine the

antifouling properties, polymers possessing longer chain segments would overlay bigger space on the surface and exhibit better anti-pollution effects.

Designing of micro/nano-structural coatings on material interfaces has been applied for self-cleaning and low-adhesive bio-applications.<sup>[74, 75]</sup> The structured coatings are commonly applied to material surfaces via physical approaches, and without altering the material's bulk natures and surface chemistry. Coatings bearing polymer structures in micro- or nano-scales (usually at the same dimension level as proteins or macromolecules) change the surface wettability, thus manipulate pollutants' adhesion behaviors.<sup>[58]</sup> Such structures often have the ability to entrap air in between the small features, resulting in a super-hydrophobic surface and exhibiting of self-cleaning capacity.<sup>[76]</sup> In order to accomplish maximum protection and surface area contact, microorganisms tend to settle on structures that are bigger than the scales of themselves.<sup>[74]</sup> However, small feature arrays can hinder the settlement of microorganisms by implementing size restrictions.<sup>[39]</sup>

### **1.2.3. Surface grafting strategies of polymer brushes**

Over the past decades, various kinds of methods for grafting polymers to the surfaces have been developed, and researchers also demonstrated that the grafted polymers possess brilliant durability and versatility.<sup>[77, 78]</sup> Generally, these grafting methods can be divided into two types, i.e., “grafting to” and “grafting from”,<sup>[79, 80]</sup> as pictured in Figure 1.8. Regarding the “grafting to” strategy, the pre-synthesized polymers would attach to a pre-functionalized surface covalently or physically.<sup>[64]</sup> Notably, the way of “grafting to” always encounters steric hindrance inevitably, which results in low grafting density and unmanageable layer thickness. Comparably, the “grafting from” strategy is achieved by in-situ polymerization of target monomers starting from an initiated surface, normally containing initiator SAMs, which provides a densely packing on the surface and allow accurately controlling of chain end and film thickness.<sup>[81]</sup>

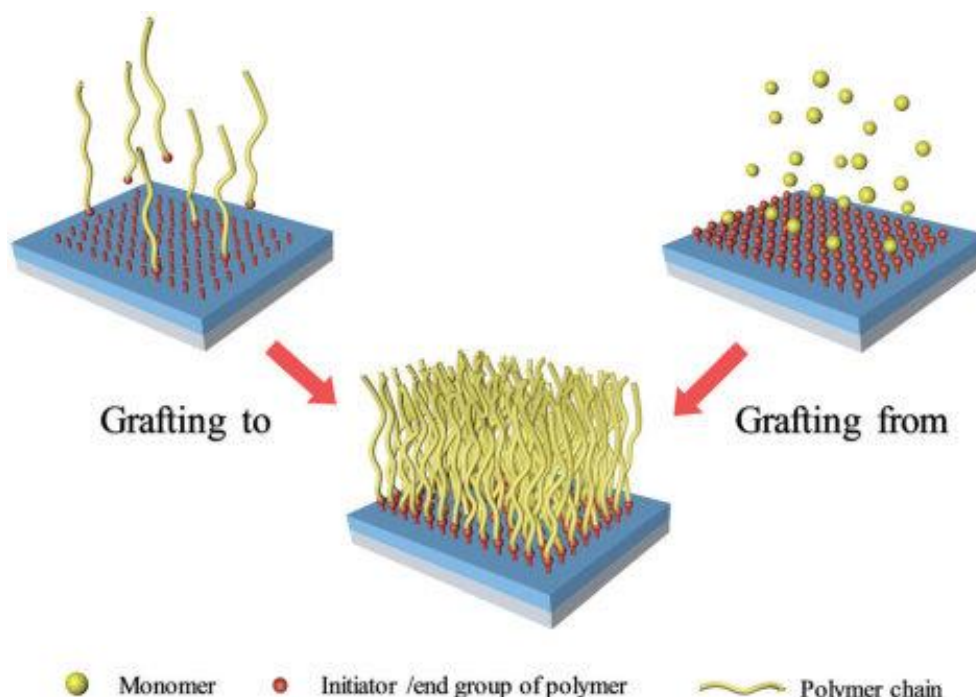


**Figure 1.8.** Schematic drawing of “grafting to” and “grafting from” fabrication strategies for surface-grafting polymers.<sup>[82]</sup>

As aforementioned, the “grafting from” approach has become the most extensively utilized technique to modify polymer brushes to material surfaces, due to its advantages in controlling polymer structures and compositions. In particular, the “grafting from” strategy is a bottom-up approach, and the anchored initiator for surface-initiated polymerization (SIP) on the material’s surface is a vital link for polymer grafting.<sup>[83]</sup> Several SIP methods have been developed to date, e.g., atomic transfer radical polymerization (ATRP), reversible addition-fragmentation transfer (RAFT), and other.<sup>[84]</sup> Among these methods, ATRP is in particular attractive because it allows precise control over polymer architecture, composition, molecular weight and film thickness, and also facilely access to copolymers and hierarchical copolymers.<sup>[85]</sup>

### 1.3. Brief review of click chemistry

Click chemistry was firstly defined by Scharless groups in 2001, and with an example for coupling organic and bioorganic molecules by Cu-catalyzed alkyne-azide 1,3-dipolar cycloaddition (CuAAC).<sup>[86]</sup> Click chemistry normally refers to a class of reactions that exhibit fabulous efficiency, chemoselectivity, enormous compatibility with functional

groups, and easily isolated products.<sup>[87]</sup> Consequently, click chemistry has been admitted as a universal agent in the modification of various molecules, especially complex natural products, providing enhanced properties or new functions for chemical biology, drug discovery, bio-imaging, and polymer synthesis.<sup>[88]</sup> After decades of development, several kinds of click reactions have been reported and widely applied in many fields, such as addition reactions, 1'3-dipole cycloadditions, and nucleophilic ring-opening reactions.<sup>[89]</sup> Among these reactions, the 1'3-dipole cycloadditions involving azides and alkynes have been commonly used as synthetic and coupling tools in organic and biological chemistry. To date, several metal catalysts have been developed to promote cycloaddition reactions between linear alkynes and azides, such as copper, ruthenium, and iridium (Figure 1.9). In the alkyne-azide cycloaddition (AAC) reactions, different catalyst normally works for different alkyne, e.g., Cu<sup>I</sup> works for terminal alkynes, Ru<sup>II</sup> preferably activates internal alkynes, and Ir<sup>I</sup> shows a high affinity to thioalkynes.<sup>[90]</sup> Researchers also studied the AAC reaction behaviors in the absence of the catalyst. Reports proved that the poor electrophile state of alkyne hardly is changed in the uncatalysed conditions, thus the existing high energy barrier restrains the reaction rate, even with a high temperature (110°C).<sup>[91]</sup> Among these AAC reactions, CuAAC is the one generally studied, as its accessible catalyst and fast reaction rate. The mechanism of CuAAC has been subject to extensive investigations, and the well-recognized principle is shown in Figure 1.10. Density functional theory calculations and kinetic studies exhibit that the CuAAC undergoes a stepwise process.<sup>[91-93]</sup> As proposed, the stepwise catalytic cycle begins with the formation of a copper(I)-acetylide  $\pi$ -complex (step 1). Followed by, azide is activated by coordination to Cu, and then forms a dicopper species with Cu<sup>I</sup>-acetylide (step 2). In the third step, a unique six-membered Cu metallo-ring is formed by the reaction between the nucleophilic copper alkynyl compound and the electrophilic organic azide, thus introducing the first C–N bond. After that, a triazole-copper derivative is generated through condensation of the six-membered metallo-ring (step 4) and forming the second C–N bond thereby. Finally, the [2 + 3] cycloaddition circle is wrapped up while the catalyst is regenerated after the protonation process (step 5).

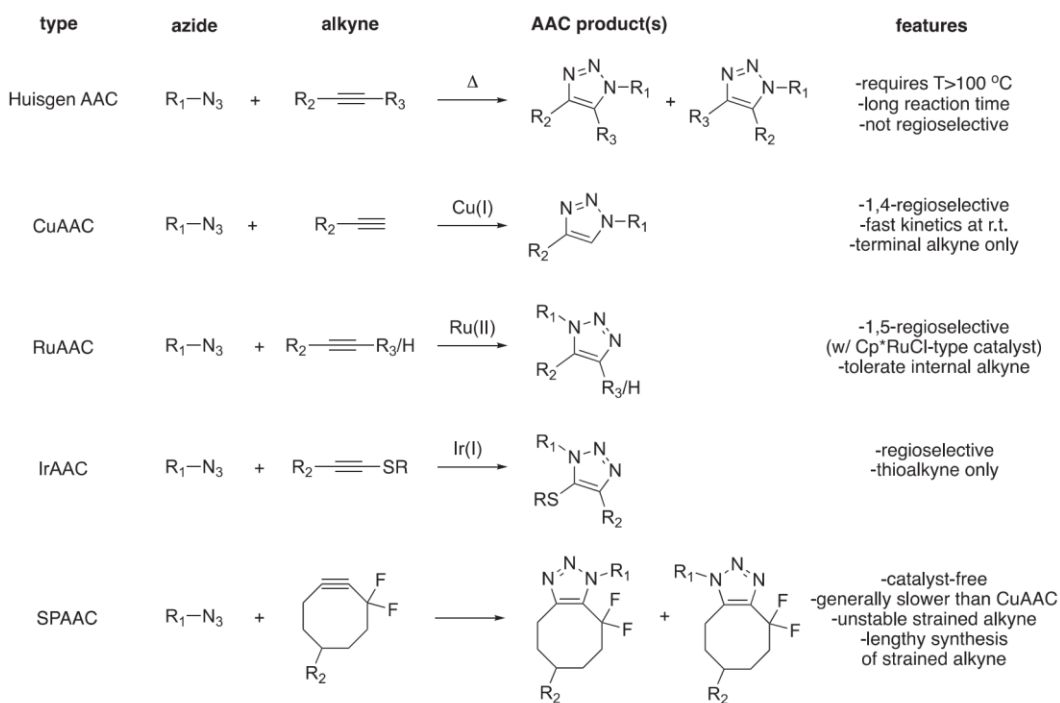


**Figure 1.9.** Different types of alkyne-azide cycloaddition (AAC) reactions.<sup>[90]</sup>

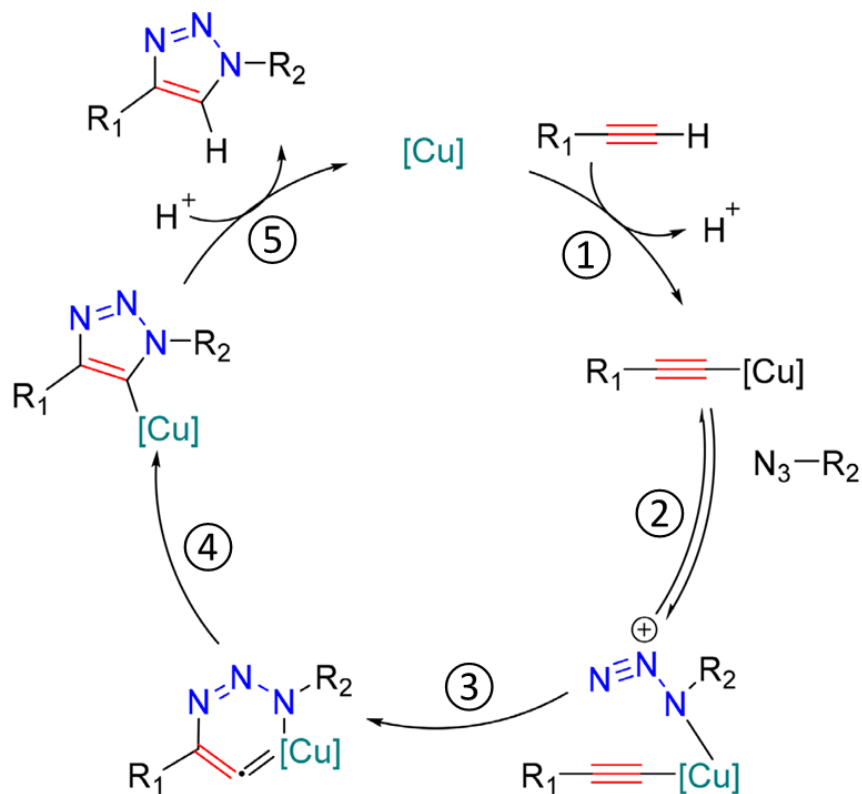


**Figure 1.10.** Mechanism scheme of CuAAC.<sup>[94]</sup>

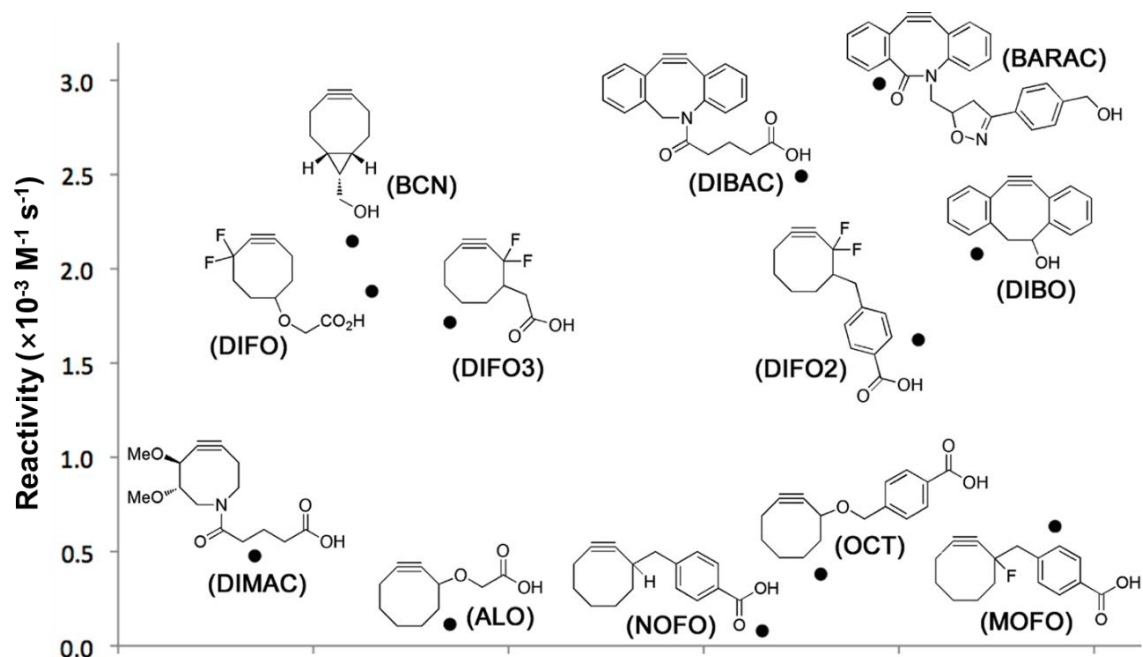


**Figure 1.11.** Reactivity chart of various strained alkyne reagents for SPAAC.<sup>[95]</sup>

In spite of the elegant advantages shown by CuAAC reactions, the toxic catalyst and easy oxidation of Cu(I) ions limit the universal adoption in biological and clinical applications. Therefore, the strain-promoted alkyne-azide cycloaddition (SPAAC) is a gold branch of 1,3-dipole cycloadditions.<sup>[96-98]</sup> As reported, the SPAAC related to kinds of strained cyclooctynes which have a high affinity to azido derivatives, has been proved no need for harmful catalysts and is more biocompatible and bio-orthogonal, therefore drawn much attention by chemists and biologists. Cyclooctyne is the smallest isolatable cyclic alkyne and has a moderate ring strain.<sup>[95]</sup> The first cyclooctyne derivative (OCT) used for SPAAC was reported in 2004 by the Bertozzi group.<sup>[99]</sup> This molecule proved that it was possible to create metal-free conditions for AAC reaction, even though the reaction rate was much lower. After that, numerous cyclooctyne derivatives with strengthened reactivities have been reported (Figure 1.11), e.g., by fluorination,<sup>[100]</sup> by  $sp^2$ -hybridization of ring atoms,<sup>[101]</sup> and by fusing of cyclopropane moieties.<sup>[102]</sup> For example, the introduction of two adjacent fluorine atoms to generate a difluorinated cyclooctyne (DIFO) that shows around a 40-fold rate enhancement compared with OCT.<sup>[103]</sup> Dibenzoazacyclooctyne (DBCO, also known as DIBAC) bearing two fused benzene rings and substituted one of the saturated carbons in the cyclooctyne ring by a nitrogen atom

exhibits high reactivity with a second-order rate constant of  $3.1 \times 10^{-1} \text{ M}^{-1} \text{ s}^{-1}$ .<sup>[104]</sup> Notably, the DBCO is accessible through nine steps for synthesis with a high yield of 41%. Additionally, bicyclononyne (BCN) is also a remarkable ring-strained alkyne that is fused with a cyclopropane and can be obtained in a straightforward process with a high yield of 61%.<sup>[102]</sup> Among these kinds of cyclooctynes, DBCO and BCN are the two representative and popular ring-strained alkynes for aryl-containing variants and saturated systems, respectively, due to they are synthetic accessibility, sufficient reactivity, and higher selectivity.

#### 1.4. Scanning probe lithography (SPL)

Thus far, numerous technologies have been reported for surface site-specific functionalization or grafting structures in nanoscale or microscale, such as scanning probe lithography (SPL), photo-lithography, electron beam lithography, inkjet printing, and 3D-printing, and more.<sup>[105]</sup> Compared with other lithographic approaches, SPL-based techniques possess splendid advantages, as SPL has the ability to achieve structures or patterns with ultrahigh-resolution and facile compatibility with substrates (either can be soft or hard materials), therefore, SPL has become an outstanding candidate for lithography aimed in applications for biological detection at molecular and cellular level (Figure 1.12).<sup>[106]</sup> After decades of development, a variety of lithography techniques based on SPL have been come up with (Figure 1.12),<sup>[107]</sup> e.g., dip-pen nanolithography (DPN), polymer pen lithography (PPL), beam-pen lithography (BPL) and microchannel cantilever spotting ( $\mu$ CS). Among these methods, DPN and  $\mu$ CS are the two more popular techniques in surface science. DPN (Figure 1.13a and b), while finding precursors in earlier works,<sup>[108, 109]</sup> was introduced by Mirkin group firstly in 1999. As principle, DPN employs an atomic force microscopy (AFM) probe coated with target ink as a “pen” to write desired material on a substrate through a meniscus between them. To date, DPN has been identified owning the ability to transfer various molecules or materials<sup>[105]</sup> (e.g., alkanethiols, DNA, proteins, polymers, and nanoparticle) to many surfaces, promoting the development of surface chemistry and biology to some extent. In view of the writing process, DPN needs to ink the AFM tip in advance and therefore, the coated ink is of limited volume, therefore continuous and large-scale writing is difficult. In  $\mu$ CS (Figure 1.13c and d), instead of the

AFM probe a surface patterning tool (SPT) is employed. As shown in Figure 1.13c, a reservoir is equipped on the SPT which is behind and connecting to the microchannel, consequently, spotting or writing in larger length scales is possible. While implementing lithography, an actuator carries a substrate approaching the apex of the inked microchannel and the ink would transfer to the substrate by capillary forces. On the whole, the SPL-based technologies exhibit great potential for fabricating multiplexed, programmable, and commercial array-based sensing biochips.

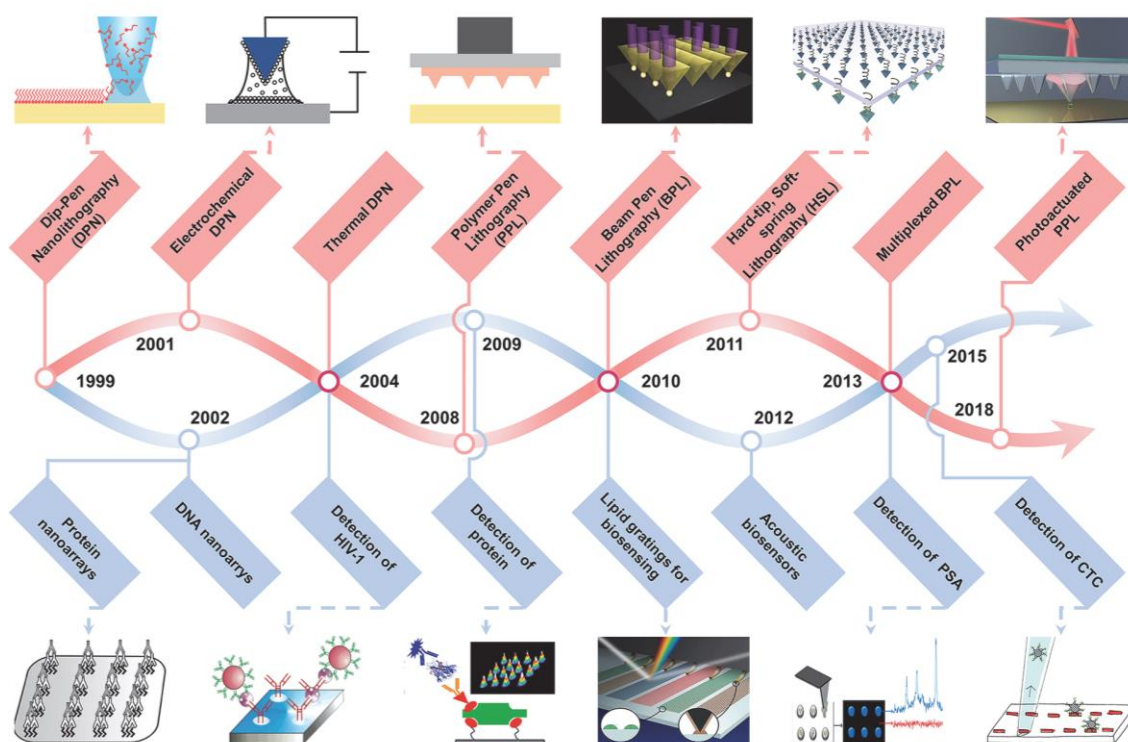


**Figure 1.12.** Timeline and milestones of development and biosensing applications of SPL-based techniques.<sup>[110]</sup>

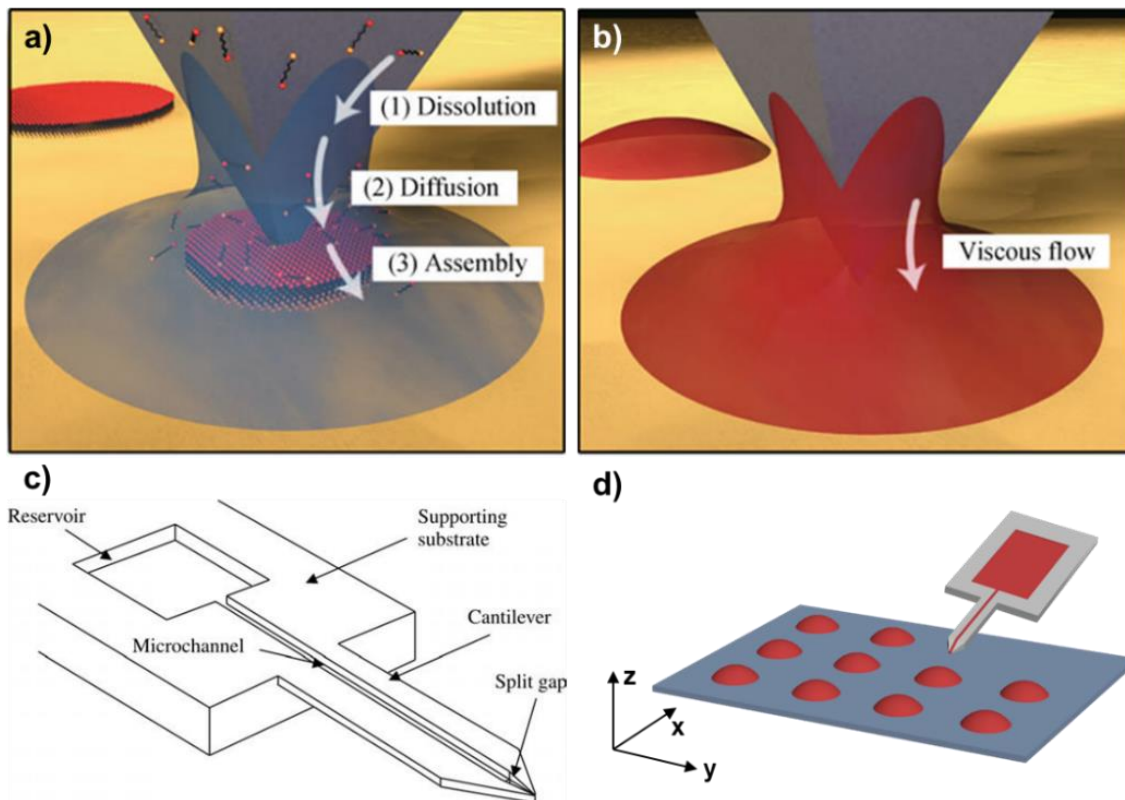


**Figure 1.13.** Schematic diagrams of the mechanisms and processes of scanning probe lithography, a) and b) ink transfer processes in DPN methodology for diffusive molecular inks and liquid inks, respectively;<sup>[108]</sup> c) surface patterning tool (SPT),<sup>[111]</sup> d) process of microchannel cantilever spotting ( $\mu$ CS) with a surface patterning tool.

## 1.5. Thesis objectives and overview

Chemical functionalization generally can endow desired properties on the material surface, such as specific molecular recognition or antifouling characteristics, which are crucial in biosensing or bioscreening applications. Actually, the biosensor can be deemed as a platform that can convert the invisible information of a special biomarker to a readable signal selectively and efficiently. Therefore, surface treatment, which aims to bear bioreceptors properly, is critical for a sensor platform construction. In this thesis, platforms modified with different functional layers are prepared for biochips fabrication. Polymer-based materials are a class of remarkable candidates for serving as biosensor surfaces due to their excellent properties in biocompatibility, the resistance to unspecific protein adhesion, high density of reactive sites, and ease of function customization. Recently, microarray techniques have become an important bioreceptor anchoring strategy for high-throughput analysis. Therefore, the  $\mu$ CS technology was employed in this thesis to immobilize bioreceptors to sensing platforms together with click reactions, which are mild, non-toxic, and high yielding. On the whole, polymer-based substrates were synthesized and employed in this thesis for fabricating biosensor platforms, which were patterned with target inks by  $\mu$ CS for DNA and protein detection.

SPAAC reactions have become an indispensable tool in bioorthogonal conjugation and surface immobilization. Numerous researches have focused on enhancing the reactivity of cyclooctynes, while a facile method for evaluating the binding efficiency of cyclooctyne-azide based immobilization without any sophisticated facilities is still missing. In chapter 2, a “grafting from” polymer, azide-bearing antifouling polymer brush (AAPB), was prepared for constructing a biosensor for high-reactive molecule screening. The polymer brushes own two building blocks, (I) poly(OEGMA) located at the bottom, showing excellent antifouling properties, and (II) azide functionalized poly(GMA) placed on the top for binding to cyclooctynes via SPAAC reactions. This co-block structure avoids blocking steps by protein blockers and exhibits chemically active moieties simultaneously. While comparing the reaction efficiency of azide/DBCO and azide/BCN through fluorescently labelled protein coupling experiments by fluorescent imaging, the DBCO derivative shows

a higher binding density to azide moieties. Thus a high-efficient molecule, DBCO-containing, was screened by this polymer-brush-based biochip.

$\alpha$ -fetoprotein (AFP) is an important biomarker for hepatocellular carcinoma (HCC) diagnosis in clinical applications. Searching for a suitable biosensor for facilely and conveniently detection of AFP has become an efficient manner for enabling HCC treatment at an early stage. In chapter 3, according to the results obtained in chapter 2, a DBCO derivative (DBCO-NHS ester) was patterned to AAPB substrates to fabricate a biosensor for AFP detection. The specific anti-AFP was directly immobilized to DBCO-NHS ester capture arrays through the formation of amide bonds, which is defined as a “direct strategy”. Consequently, the anti-AFP arrays were able to detect fluorescently labelled AFP and easily evaluated by fluorescent imaging. The results show that the direct strategy works well for AFP detection, and also provide that the direct strategy (NHS/antibody/AFP) is more sensitive than the traditionally indirect strategy (biotin/streptavidin/biotin-antibody/AFP), which is perhaps benefitting from the compact fabrication process of the biosensor.

Diamond-related materials, especially fluorescent nanodiamonds, are non-toxic, biocompatible and self-fluorescent materials, thus widespread with many applications, e.g., biomedicine, biosensing and bioimaging. However, the unmodified diamond materials are still highly restricted due to their poor dispersibility in media, weak fluorescence and low signal-to-noise ratio as biosensors. Therefore, in chapter 4, we aim to use a methacrylate-based alkyne-bearing polymer brush coating to modify the diamond surface, reduce its fluorescent background, and improve its signal-to-noise ratio. The methacrylate-based polymer brush consists of two segments, poly(N-(2-hydroxypropyl)-methacrylamide) (HPMA) and poly(propargylacrylamide) (AlkMA). Poly(HPMA) is a hydrophilic polymer which can lower the unfavorable nonspecific protein adhesion on the surface. Poly(AlkMA) is employed to introduce alkyne moieties to the copolymer structure. Thus the copolymer can easily react to azide-derivatives to bind biomolecules for selective sensing targets or add fluorophores to increase fluorescence. All in all, we aim to obtain diamond-based biochips with low background noise, high sensitivity, and high resolution in fluorescence imaging based on this methacrylate-based polymer brush modification.

In DNA detection, the surface morphology and compositions normally affect the hybridization efficiency. In chapter 5, we aim to search for one suitable biosensor platform for high-efficient DNA hybridization from three differently modified surfaces. For doing so, a gold-coated silicon substrate, a DBCO-modified surface (cycloalkyne SAM), and a PBAG-modified surface (“grafting to” polymer) were prepared and served as sensing platforms together with Au-S bond, thiol/yne coupling, and thiol/epoxy reaction in  $\mu$ CS spotted microarrays, which contain thiolated DNA probes, for DNA sensor fabrication. After that, the DNA hybridization efficiency was assessed with a fluorescent microscope on these three platforms. The SH-oligomer probes all work well for DNA hybridization on these three platforms. While performing protein binding assays, the DNA hybridization shows a higher efficiency on the PBAG-based sensing platform. In this way, a suitable biosensor platform for high-efficient DNA hybridization was selected.



**Figure 1.14.** Schematic representation of the thesis overview.

## Chapter 2 – Screening of high-efficient cyclooctyne on azide-bearing antifouling polymer brushes (AAPBs)\*

### 2.1. Introduction

Recently, surfaces possessing both resistance to protein adhesion and reactive groups to undergo covalent functionalization have drawn much attention in biological researches, especially examples based on click chemistry approaches. Since the advent of click reactions at the beginning of 21<sup>st</sup> century,<sup>[86]</sup> these reactions are consistently a vital link in the process of biosensing, bioscreening, drug delivery, and bio-functionalization.<sup>[112-115]</sup> Particularly, the strain-promoted alkyne-azide cycloaddition (SPAAC) is an outstanding member of this class owing to its excellent chemical stability, non-toxic and mild reaction conditions, and high coupling efficiency for bio-orthogonal conjugations.<sup>[116-119]</sup> Benefitting from the activation by ring strain in the structure of cyclooctynes, the SPAAC reactions have circumvented the need for toxic catalysts (e.g. Cu<sup>I</sup>) and offer a fast rate for binding with azides, which is favorable for biochemistry, in particular for studies involving living cells.<sup>[120, 121]</sup>

Commonly, azide derivatives are used as bio-tags in biochemistry due to easy integration with biomolecules, e.g., in metabolic labelling for living cells with azido functionality,<sup>[122, 123]</sup> postsynthetic modification<sup>[124, 125]</sup> and in-vitro enzymatic transfer.<sup>[126, 127]</sup> Attention has been placed on enhancing the reactivity of cyclooctynes – being the other half in SPAAC – as part of the reactive probes in bio-conjugations. After the first recognition of the potential in the combination of cyclooctyne with bio-conjugation by Bertozzi and coworkers in 2004,<sup>[99]</sup> click chemistry has entered a new metal-free era. Plenty of research groups have contributed to advance the use of cyclooctynes in order to enhance the reactivity toward azides, for the purpose of enlarging the utility and enhancing the reactivity of the SPAAC. Several cyclooctyne variants have been developed for bio-conjugations (Figure 1.11), which can be roughly classified into two types, i.e., aryl-containing variants and saturated systems.<sup>[90, 95, 128]</sup> The two most commonly used representatives of each type are dibenzocyclooctyne (DBCO)<sup>[104]</sup> and bicyclononyne (BCN)<sup>[102]</sup>, respectively. Currently

available cyclooctynes were mostly developed to enhance the reactivity to azides via modulation either by fluorination,<sup>[100, 103]</sup> sp<sup>2</sup>-hybridization of ring atoms,<sup>[129]</sup> or by fusion to cyclopropane.<sup>[102]</sup> DBCO and BCN are commonly used for SPAAC in bio-conjugations because of their relatively simple synthesis with sufficient yield and great coupling efficiency. Other cyclooctynes have comparatively low reactivity or a tedious synthetic procedure.<sup>[101, 102, 104, 130, 131]</sup>

As a whole, SPAAC is an effective and crucial tool in the development of bio-research and bio-applications, e.g., in biosensors or for surface modification in biological experiments, but there is still a lack of facile and generalized ways for studying the relative coupling efficiency between cyclooctynes and azides, since the known reports all rely on expensive and complex facilities to obtain the rate constant for comparison. The use of polymer brushes to encode different functionalities alongside their structure such as antifouling properties, functional groups for further functionalization and many more which include copolymers,<sup>[132-134]</sup> block copolymers,<sup>[135-138]</sup> and terpolymers<sup>[139]</sup> were reported. In 2010, the DBCO functionalized brushes for orthogonal functionalization of the surface with azide containing molecules were presented.<sup>[140]</sup> They developed an azide-containing antifouling polymer brush that can be functionalized using DBCO-conjugated biomolecules while not impairing the antifouling properties.<sup>[141]</sup> This served to facilitate the detection of target proteins in blood plasma. Here, DBCO or BCN derivatives acted as bio-receptors. More recently, another report proved that the site-specific immobilization of cyclooctynes on azide-modified polymer brushes via printing of microarrays was possible.<sup>[63]</sup> Utilizing lithographic approaches makes it feasible to investigate the difference in binding efficiency of conjugations between DBCO/azide and BCN/azide through quantified fluorescence measurements with a fluorescence microscope using a compound linked to the same binding motif (here biotin) to be able to attach the exact same type of fluorescent protein, avoiding changes in the fluorophore emission profile that could affect a fluorescent moiety directly on the DBCO or BCN molecule (Figure 2.1). To elucidate this approach and quantify the different reactivity, we synthesized azide-bearing antifouling polymer brushes (AAPBs) by “grafting from” strategy as the lithography substrate, and then immobilized various DBCO and BCN derivatives via  $\mu$ CS. To obtain a high number of functional groups, side-chain functionalization was implemented on the

polymer brushes.<sup>[142]</sup> Additionally, to minimize side effects on antifouling due to the thickness of the top block, the thickness of the top layer was synthesized to only about 8 nm, following our previous work.<sup>[141]</sup> Generally, the polymer brushes consist of two building blocks: the bottom block is an inert layer [poly(OEGMA)], highly-protein repelling and therefore does not require any blocking steps in the performed specific protein binding studies; the top block is a reactive layer functionalized with azide groups [poly(GMA)-N<sub>3</sub>], which can participate in the SPAAC reactions. Based on these properties, a protein binding assay was implemented to obtain an accurate and quantitative comparison of immobilization efficiency, as well as confirming the feasibility of intended applications for these polymer brushes in microarray-based bioscreening for the two SPAAC regimes.

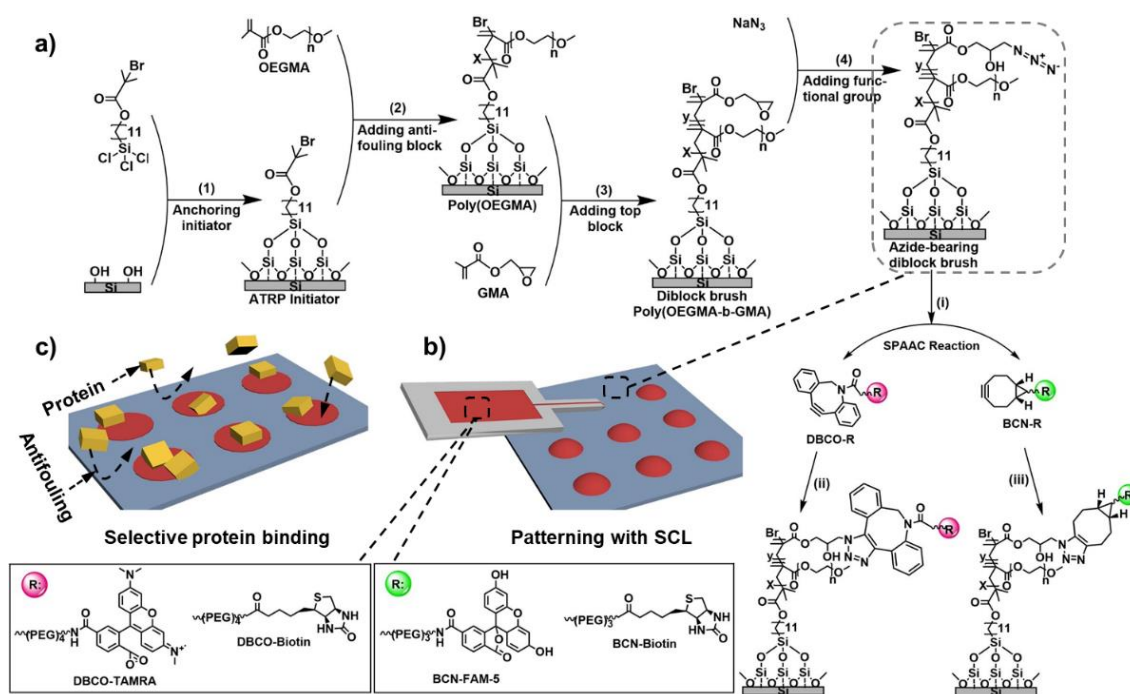


**Figure 2.1.** Schematic drawing of a) the growth process and chemical binding strategies for coupling to the AAPBs. b) Schemes of capturing arrays spotted by  $\mu$ CS to the polymer brush surface for (c) selective protein coupling. The insets show the DBCO and BCN derivatives used in the site-specific functionalization.<sup>[143]</sup>

## 2.2. Results and discussions

### 2.2.1. Physical and chemical characterization of polymer brushes

Interfaces combining reactive and antifouling properties, possessing adjustable reactive sites and remarkable capabilities of protein repellency are playing a significant role in constructing platforms for label-free biosensing, and other biological researches.<sup>[50, 132, 144, 145]</sup> Polymer brushes, especially those with hierarchical architectures, are a remarkable candidate to meet the aforementioned needs. Generally, the excellent self-cleaning performance benefiting from the densely packed non-fouling molecules and the adjustable reactive groups at the polymer chain end can provide customizable terminals for satisfying diverse demands. Typically, azides are a sort of widely used substances to introduce such activated sites for binding biomolecules or analytes based on SPAAC reactions. In this chapter, the AAPBs were utilized to repel un-specific proteins and react with ring-strained alkynes.

**Table 2.1.** Static water contact angle (WCA), thickness and roughness reports of the films of the surfaces.

Items	WCA [°]	Roughness [Ra, nm]	Thickness [nm]*
Silicon	--	--	0 (reference)
Glass (plasma-treated)	0	0.159 ± 0.021	--
Initiator (SAM)	81.2 ± 2.8	0.216 ± 0.029	1.8 ± 0.2
Poly(OEGMA)	46.5 ± 2.2	0.351 ± 0.043	24.3 ± 0.5
Poly(OEGMA- <i>b</i> -GMA)	50.2 ± 3.1	0.595 ± 0.107	32.7 ± 0.6
Poly(OEGMA- <i>b</i> -GMA)-N <sub>3</sub>	66.7 ± 1.9	0.613 ± 0.096	31.5 ± 0.4

Every mean value with standard deviation was computed from three measurements at random positions. WCA and roughness measurements were conducted on glass samples. The WCA of freshly plasma-treated glass surface was extremely low and beyond the measurement limitation, therefore we roughly recognized it at zero. \*Silicon wafers modified with polymer brushes were prepared in parallel with glass samples were used for thickness measurements in dry conditions with an ellipsometer.

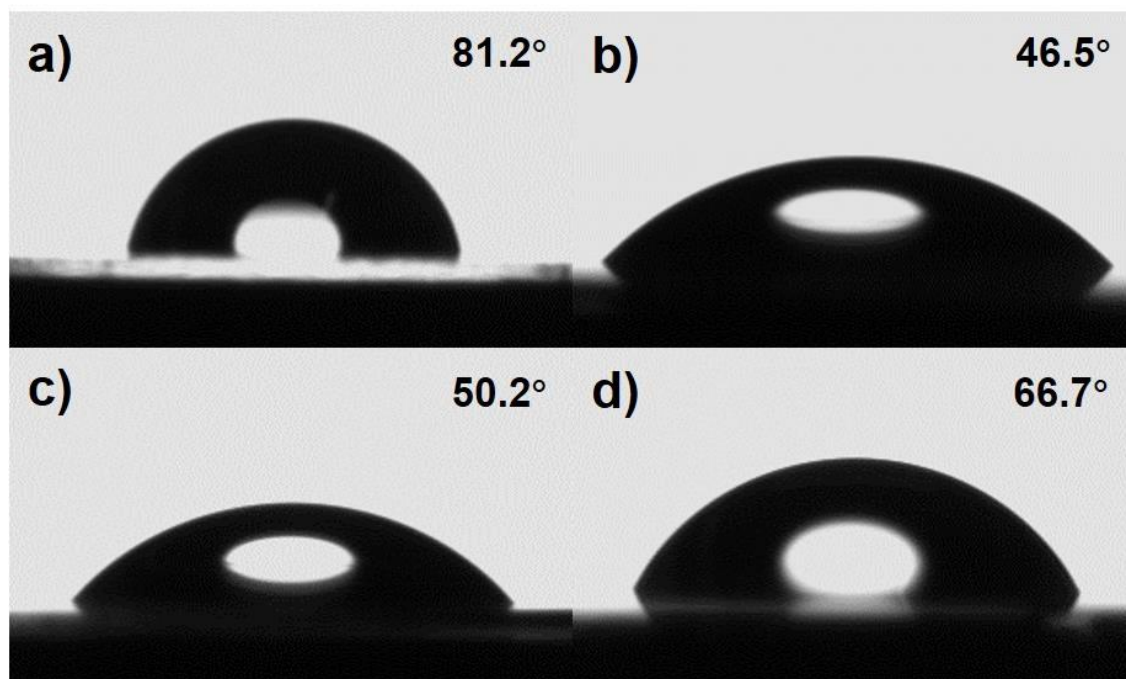


**Figure 2.2.** Static WCA of the surfaces in the sequential growing steps of polymer brushes. a) ATRP initiator, b) poly(OEGMA), c) poly(OEGMA-*b*-GMA), d) poly(OEGMA-*b*-GMA)-N<sub>3</sub>.<sup>[143]</sup>

Patterning molecular arrays on substrates with  $\mu$ CS is strongly impacted by surface properties, therefore wettability and roughness of the surface in each state of growing the polymer brushes were investigated and the successful chemical functionalization was also monitored. For this, the static water contact angle (WCA) measurements, ellipsometric thickness, AFM, and x-ray photoelectron spectroscopy (XPS) were conducted. WCA testing is a facile and effective way to study the altering of the surface wettability induced by changes in the chemical surface state. On this ground, the static WCA was performed for the substrates in each modification step, and the corresponding results are shown in Table 2.1 and Figure 2.2. Initially, the formation of a self-assembled monolayer (SAM) of the silane ATRP-initiator on a fresh oxygen plasma-treated substrate leads to a sudden rise in water contact angle from 0 to 81.2° as well as is identified clearly by the C 1s and Br 3d XP spectra (details below in XPS section). For inspection of the SAM quality, thickness and morphology measurements were conducted with ellipsometry and AFM on silicon (prepared in parallel with the glass specimens) and glass substrates, respectively. As shown in table 2.1 the thickness is 1.8 nm, and the corresponding AFM image (Figure 2.3a)

exhibits the uniform and smooth topography of the surface. All in all, the results above demonstrate successful SAM formation. With reference to the SAM, the WCA on the surface with the bottom block [poly(OEGMA)] drops sharply, as expected by the introduction of the hydrophilic polymer side chains. While the wettability slightly changed on the copolymer surface [poly(OEGMA-*b*-GMA)], A possible reason could be the similar backbone of poly(GMA) and poly(OEGMA). On the introduction of the azide groups to the polymer brush, the WCA converted back to a higher value, indicating that the functionalization was successful. The moderate hydrophilicity of the completed substrate offers a stable interface to adhere ink dots spotted by  $\mu$ CS (where very low WCA would make the printed spots spread and merge together with adjacent ones, finally destroying the patterned arrays).

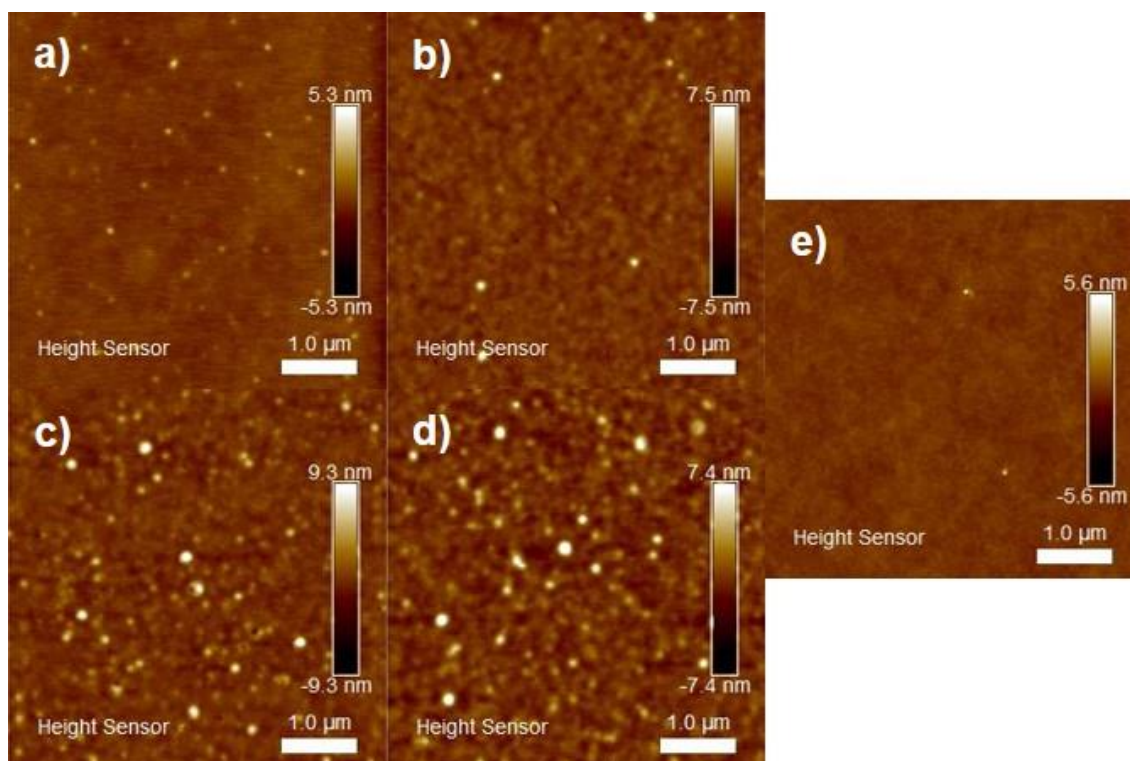


**Figure 2.3.** Surface topography of glass-based specimens at various stages within the polymer brush growth process imaged by AFM with tapping mode. a) ATRP initiator, b) poly(OEGMA), c) poly(OEGMA-*b*-GMA), d) poly(OEGMA-*b*-GMA)-N<sub>3</sub>, e) bare glass. Corresponding roughnesses are given in Table 2.1. All scale bars equal 1  $\mu$ m.<sup>[143]</sup>

In parallel with the inspection of the WCA, measurements of surface topography were implemented to survey the variation in roughness, further corroborating the development of polymer brushes. Generally,  $\mu$ CS works best on smooth interfaces, as large roughness may cause difficulties for ink transfer and for constructing ordered dot arrays. Figure 2.3 shows AFM images of surfaces at the different stages during the process of polymer brush growing. As can be seen, after grafting of ATRP initiator the surface morphology barely changes compared to a bare glass surface (Figure 2.3e), the surface morphology remains smooth and the mean roughness ( $R_a$ ) is  $(0.216 \pm 0.021)$  nm. The synthesis of the first layer of the bilayer polymer brushes induced a significant increase in roughness ( $R_a$ , from  $(0.216 \pm 0.021)$  nm to  $(0.351 \pm 0.029)$  nm), caused by the generation of sequential and well-oriented compact structures of poly(OEGMA) on the SAM initiator surface, indicating that the antifouling block was successfully grafted. Similarly again, a further increase in roughness ( $R_a$ , from  $(0.351 \pm 0.029)$  nm to  $(0.595 \pm 0.107)$  nm) indicated successful chain extension with GMA molecules and formed the copolymer poly(OEGMA-*b*-GMA). However, the image also shows that the overall homogeneous and rather a smooth interface was maintained even as the former step changed roughness. In the last preparation step, after azido functionalization of the terminal groups, the roughness stays constant ( $R_a$ , from  $(0.595 \pm 0.107)$  nm to  $(0.613 \pm 0.096)$  nm), which is also expected as of the small size of the added azido group, thus the terminal change in brush structure is not much varying the surface morphology.

XPS was employed to thoroughly characterize and identify the chemical compositions of the diblock polymer brushes, and the results are illustrated in Figure 2.4 and 2.5. First, the silane initiator formed a SAM of 1.8 nm on a freshly treated substrate. As illustrated in Figure 2.4, a peak appears at 70.1 eV over the scan of Br 3d region, which means the bond Br–C exists, thus confirming the formed SAM. Moreover, as plotted in Figure 2.5a-1, a strong peak appears at 284.5 eV and is attributed to C–C and C–H in the scaffold of the alkane of the initiator. Additionally, the C–O and O=C–C within the ester group induce two relatively weak peaks at 286.0 and 288.5 eV, respectively. The scale distribution of the three peaks originating from the initiator is consistent with its chemical structure that the bonds C–C and C–H occupy the major quotient in the structure, but only one ester group exists. The acquired XPS data of the antifouling block is shown in Figure 2.5a-2.

The addition of macromolecular [poly(OEGMA)] adds mass of C–O all along the side chains of the polymer and raises the proportion of C–O within the structure, therefore leading to a predominant signal at 286.0 eV. In addition, the signal at 288.5 eV can be attributed to the contribution of O=C–C in the methacrylate backbone. Consequently, the area ratio between the (C–O) and (C–C, C–H) is approximately 2.33. Above the approximately 22 nm layer of poly(OEGMA) a layer of poly(GMA) with about 8 nm thickness was grown. Layers of the same magnitude have been shown to possess excellent properties for conjugation and protein repellence, though the relative thicknesses of each layer might deviate to some extent by blending between the two blocks.<sup>[63]</sup> Figure 2.5a-3 depicts the XP spectrum of the copolymer [poly(OEGMA-*b*-GMA)] collected in C 1s region. By contribution from the grafted poly(GMA) block, the intensity of the signal of all the sorts of covalent bonds in the copolymer structure is strengthened. Accordingly, the area ratio of (C–O):(C–C, C–H) drops to 1.59. Figure 2.5a-4 and Figure 2.5b-4 picture the XP spectra of azido functionalized copolymer in the C 1s and N 1s region, respectively. The epoxide groups were attacked by NaN<sub>3</sub> dissolved in DMF and a ring-opening reaction took place, therefore endowing azido groups to the polymer brush. As envisioned, there was no signal recorded in the N 1s region from copolymers [poly(OEGMA-*b*-GMA)] before functionalization with the azide. According to a previous report,<sup>[131]</sup> high energy x-ray beams can destroy the structure of polymers and degrade the azido groups gradually, this is a plausible reason to explain the small signal that appears at 399.4 eV in Figure 2.5b-4. Peaks at 401.0 and 404.6 eV are an accurate signal feedback of azido moieties, confirming the terminal substitution and formation of azide-bearing antifouling polymer brushes.

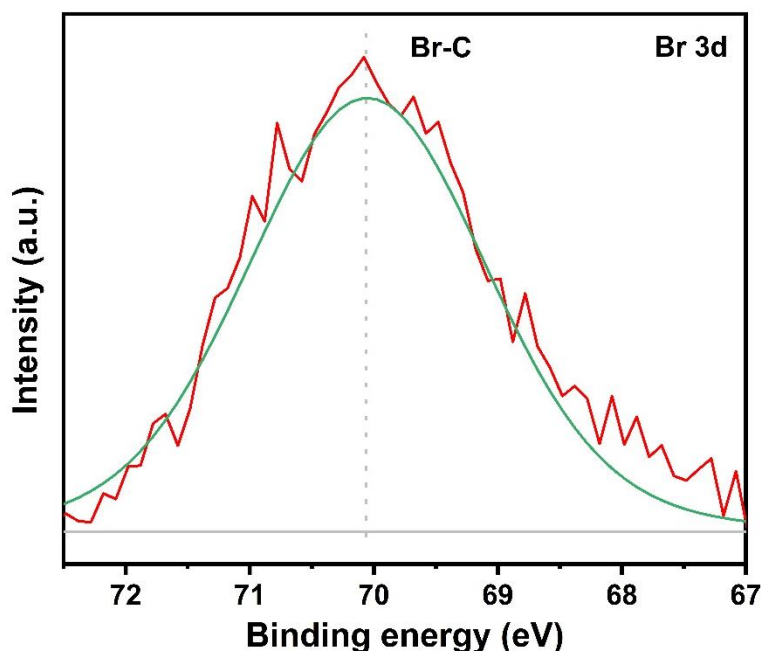


Figure 2.4. XP Spectrum of SAM initiator at Br 3d region.<sup>[143]</sup>

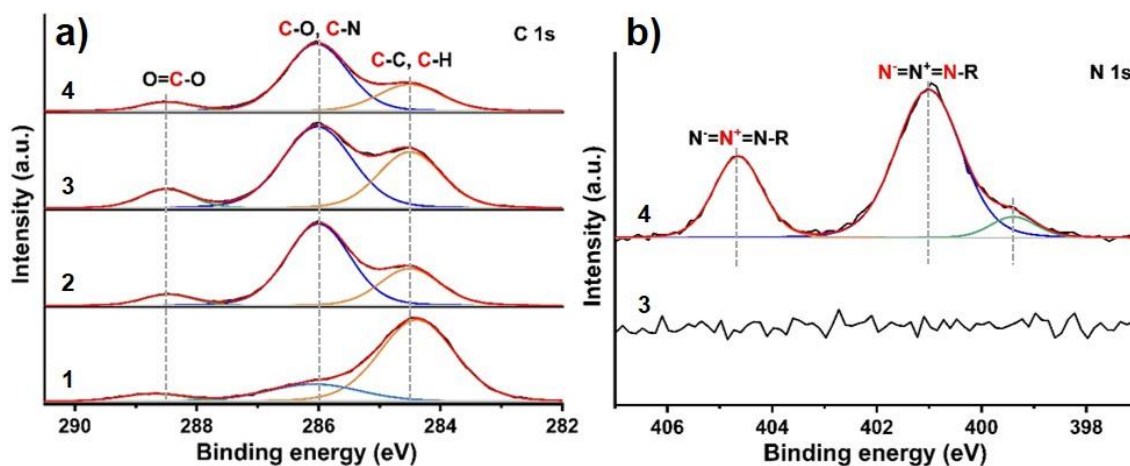
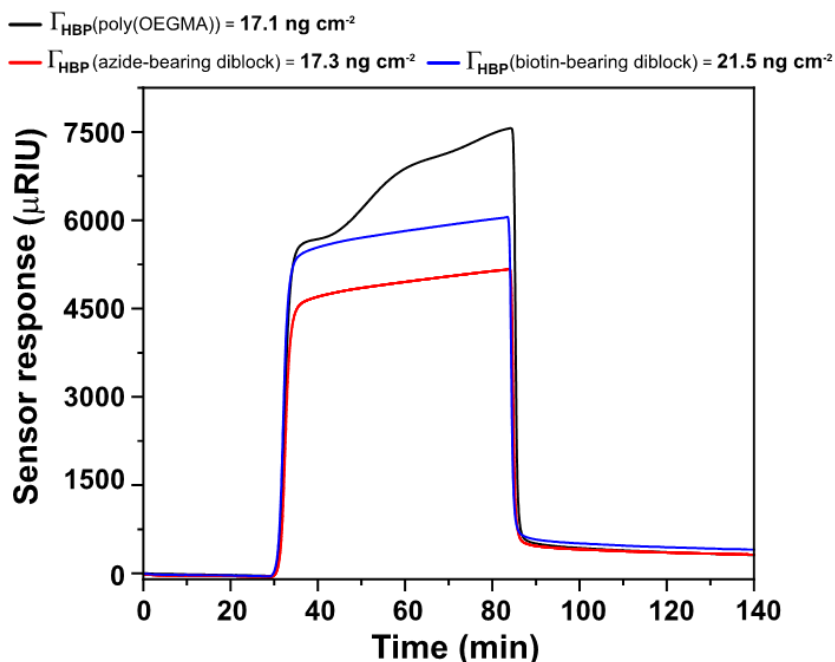


Figure 2.5. a) XPS characterization at C 1s region of different surfaces, 1) ATRP initiator, 2) poly(OEGMA), 3) poly(OEGMA-*b*-GMA), 4) poly(OEGMA-*b*-GMA)-N<sub>3</sub>. b) XPS characterization at N 1s region of poly(OEGMA-*b*-GMA) before 3) and after 4) azide functionalization. The components resulting from corresponding chemical species are highlighted in red.<sup>[143]</sup>

### 2.2.2. Antifouling property characterization

The use of antifouling polymer brushes in array-based sensing techniques overcomes the blocking steps by blockers, which simplifies the experiment procedures and makes it easier for signal readout. In order to show that the AAPBs possess excellent antifouling performance, the surface plasmon resonance (SPR) was conducted with undiluted human blood plasma (HBP), and the results are shown in Figure 2.6 including measurements on poly(OEGMA), poly(OEGMA-*b*-GMA)-N<sub>3</sub>, and biotin-modified poly(OEGMA-*b*-GMA) brushes. Prior to implementing SPR,  $\omega$ -mercaptoundecyl bromoisobutyrate SAMs were prepared on gold SPR chips, from which polymer brushes were grafted as described in the experimental method section below. The biotin-modified poly(OEGMA-*b*-GMA) chips were prepared by functionalization with biotin in situ in the SPR setup. Subsequently, all tested polymer brushes were challenged for 1 h with undiluted HBP, one of the most challenging biological media, to determine their resistance to unspecific protein pollution. The results show that the poly(OEGMA) surface is hardly polluted by the media, as the detected fouling was only 17.1 ng cm<sup>-2</sup>. Further grafting of azide-functionalized diblock and its functionalization with biotin did not significantly impair the antifouling properties of poly(OEGMA) brushes resulting in 17.3 and 21.5 ng cm<sup>-2</sup>, respectively. These data are well in line with previously published reports for bare poly(OEGMA) brushes.<sup>[146, 147]</sup>



**Figure 2.6.** SPR measurements acquired at  $\lambda = 670$  nm showing unspecific protein adsorption from undiluted human blood plasma on poly(OEGMA) (black), poly(OEGMA-*b*-GMA)-N<sub>3</sub> (red), and biotin-bearing poly(OEGMA-*b*-GMA) brushes (blue).<sup>[143]</sup>

### 2.2.3. Fluorescent inks patterning for printing and reaction parameters test

After establishing the successful synthesis of the desired polymer brush, two types of representative cyclooctynes, aryl-containing cyclooctyne (DBCO) and saturated system (BCN), were employed to explore the difference of the immobilization density and efficiency on azide-bearing brushes between the two cyclooctynes. In order to establish the optimum lithography regime for the target inks in  $\mu$ CS, microarrays including 100 dots were patterned into  $10 \times 10$  matrixes with a pitch of  $50 \mu\text{m}$  at different printing parameters (e.g., dwell time and relative humidity). The fully functionalized polymer brushes could sustain fluorescent arrays even after washing away of excess ink, while (as negative control) arrays printed on substrates of bare glass and diblock polymer brushes without azide moieties, poly(OEGMA-*b*-GMA), vanish after washing (Figure 2.7). In these conditions, we conclude that the glass slide and the unfunctionalized polymer brush barely affect the fluorescent signal.

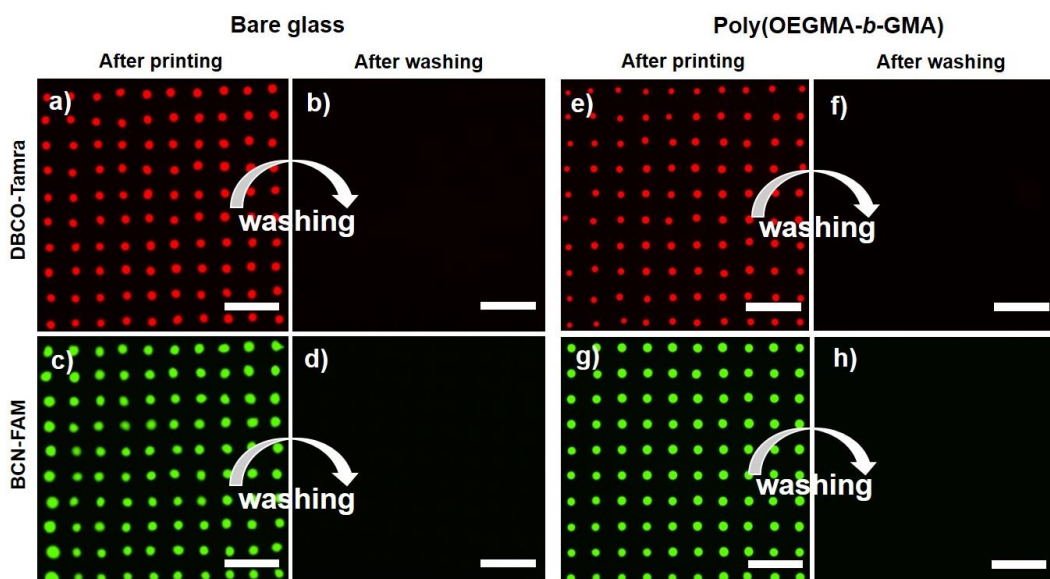


**Figure 2.7.** Spotting of DBCO-Tamra and BCN-FAM on bare glass and on polymer brushes without azido functionalization. Exposure times are 5 ms for patterns after printing and 1 s for samples after washing, and scale bars are  $100 \mu\text{m}$ .<sup>[143]</sup>

Humidity as a major factor in printing was studied initially, since it highly controls the speed of the ink transfer and can alter the concentration of the spotted ink by drying or hygroscopic action. Figure 2.8 pictures the feature size and relative fluorescence intensity on polymer brushes of DBCO-Tamra ink written at a humidity range from 20% to 70%. As illustrated in Figure 2.8a and b, the feature size (as here denoted by feature area) has a positive correlation with increasing humidity, but negative for fluorescence intensity. A possible explanation here is that the ink solution collects extra water vapour from the humidity in the atmosphere, which lowers ink viscosity and concentration, hence leading to faster ink flow and giving a bigger size yet weaker fluorescence intensity of spots. In addition, raised environmental humidity will also affect the polymer brush hydration and thus lowering the contact angle of the deposited droplet, further increasing the feature size and area over which the ink volume is spread. Typical images captured on specimens printed at 20% and 70% relative humidity are shown in Figure 2.8c and the corresponding feature size distribution on a 20% sample is given in Figure 2.8d.

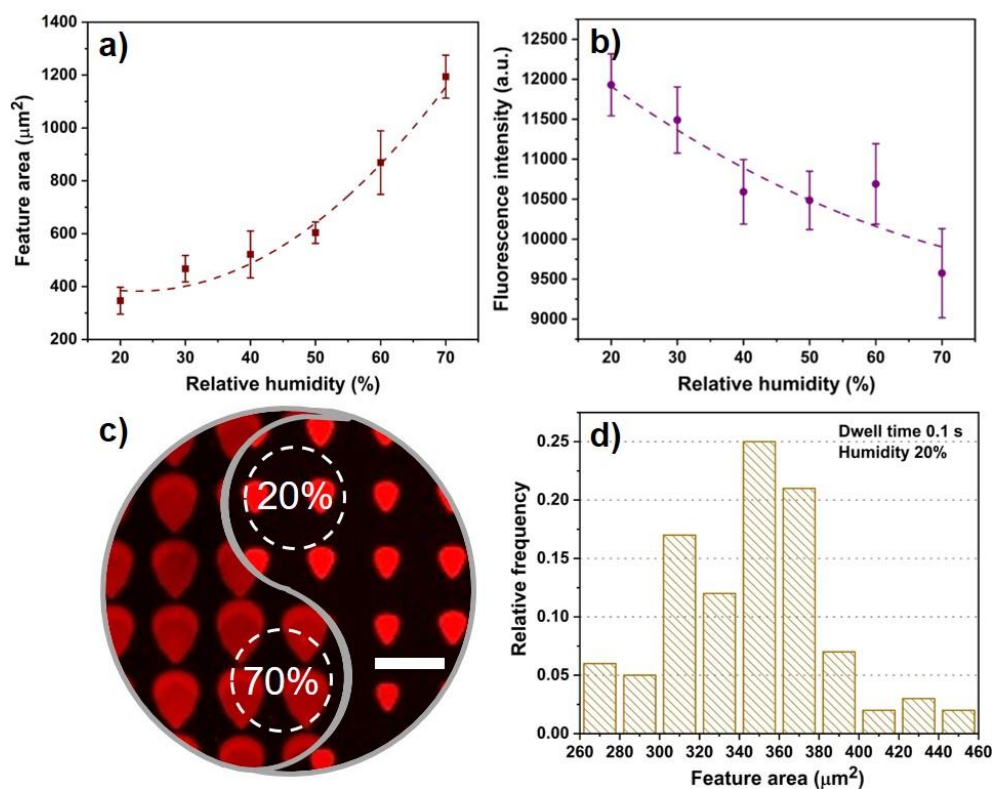


**Figure 2.8.** Dependence of a) feature size and b) relative fluorescence intensity on humidity of DBCO-Tamra on AAPBs; and c) fluorescent micrographs captured with

exposure times of 5 ms on two diverse patterns printed at dwell time of 0.1 s but at two different relative humidity situations, 20% and 70%, respectively; d) the corresponding feature area distribution of the microarray in c) written at relative humidity of 20%. Scale bar is 50  $\mu\text{m}$ .<sup>[143]</sup>

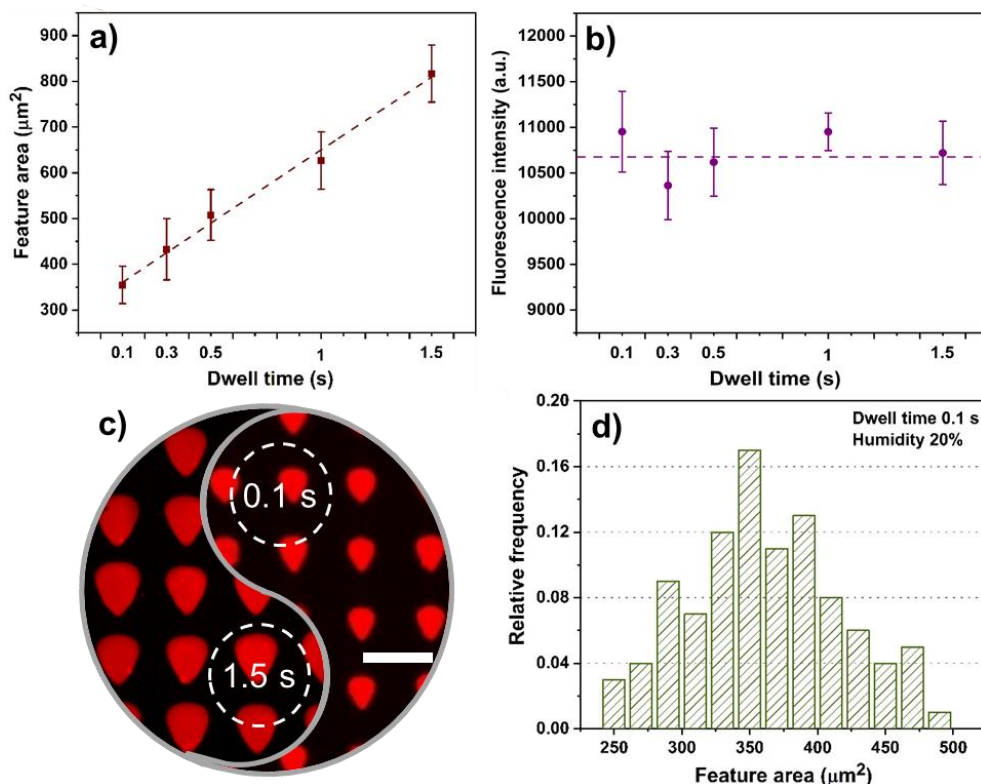


**Figure 2.9.** Dependence of a) feature dimension and b) relative fluorescence intensity on dwell time of DBCO-Tamra on AAPBs. c) Fluorescent images taken on two microarrays printed at relative humidity of 20% but dwell time of 0.1 and 1.5 s, with exposure time 5 ms. d) The corresponding feature dimension distribution of micropattern in c) written at dwell time 0.1 s. Scale bar is 50  $\mu\text{m}$ .<sup>[143]</sup>

Dwell time (tip/sample contact time during feature spotting) is another crucial parameter to govern the feature dimension and its size distribution. Figure 2.9 shows the results of DBCO-Tamra by tuning the dwell time. Evidently, the dwell time only affects the feature dimension, but not fluorescence intensity, as the amount of deposited ink contains much more molecules for immobilization than binding sites are available at the footprint of the droplet feature, thus overall deposited volume does not affect the amount of bound

compound per area. Results of the same set of experiments with BCN-FAM ink following similar trends are given in Figure 2.10 and 2.11. Based on these results and to obtain a narrow feature size distribution and highest fluorescence intensity, we fixed printing parameters for DBCO and BCN derivatives for the remaining experiments to a humidity of 20% (both) and dwell time of 0.1 s and 0.5 s, respectively.

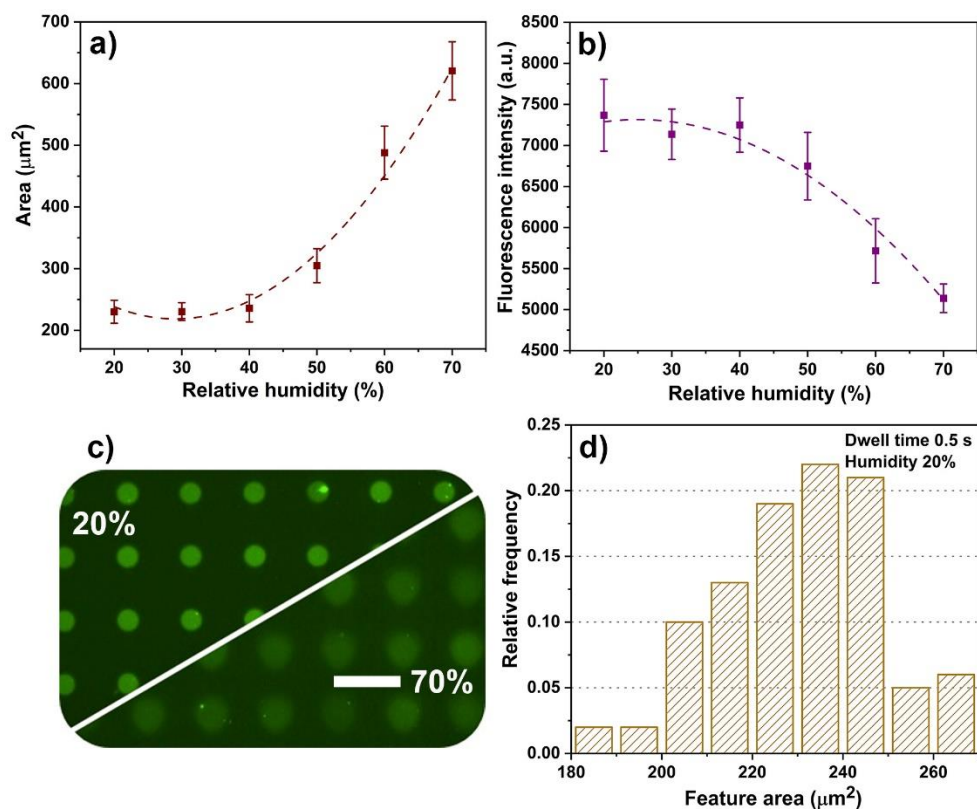


**Figure 2.10.** Dependence of a) feature size and b) relative fluorescence intensity on humidity of BCN-FAM on AAPBs; and c) fluorescent micrographs captured with exposure time 5 ms on two diverse patterns printed at dwell time of 0.5 s and at two different relative humidity situations, 20% and 70%, respectively; d) the corresponding feature area distribution of the microarray in c) written at relative humidity of 20%. Scale bar is 50  $\mu\text{m}$ .<sup>[143]</sup>

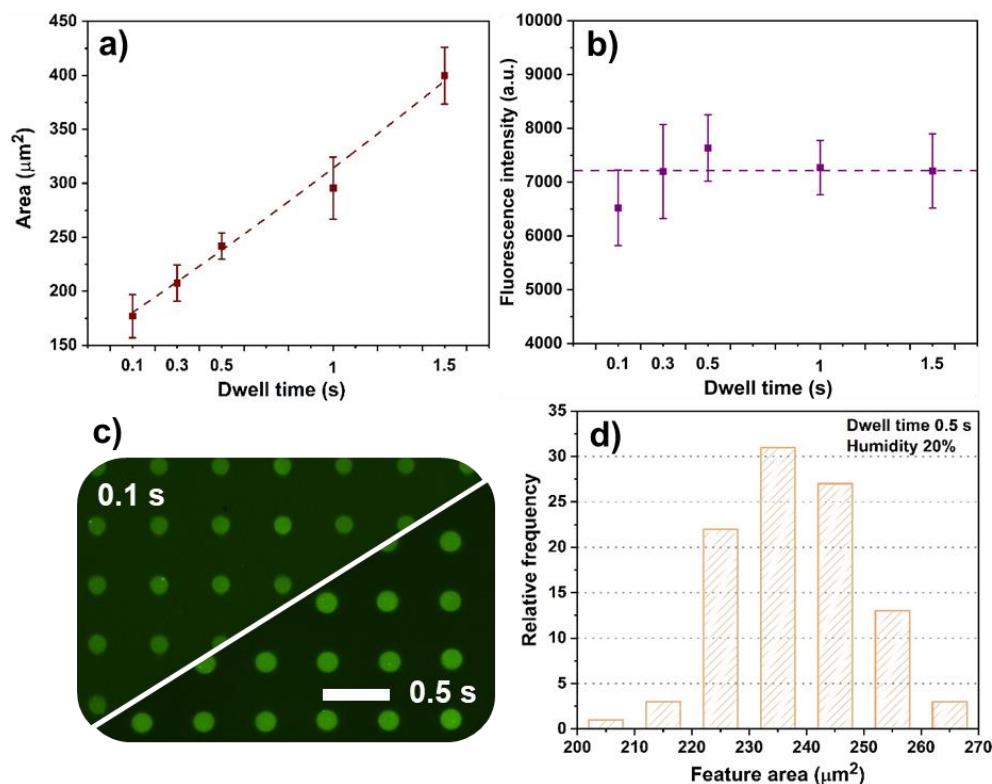


**Figure 2.11.** Dependence of a) feature dimension and b) relative fluorescence intensity on dwell time of BCN-FAM on AAPBs. c) Fluorescent images taken on two microarrays printed at relative humidity of 20% and dwell time of 0.1 and 0.5 s, with exposure time 5 ms. d) The corresponding feature dimension distribution of micropattern in c) written at dwell time 0.5 s. Scale bar is 50  $\mu\text{m}$ .<sup>[143]</sup>

Reaction time and temperature are the two vital factors in click reactions. Therefore, to evaluate the efficiency of SPAAC reactions between azide and cyclooctynes in  $\mu\text{CS}$ , the printed samples were allowed to rest for various reaction durations at room temperature (25°C) and at slightly elevated “physiological” temperature (37°C) for comparison. The results for fluorophore-DBCO conjugate ink immobilized on the AAPBs (arrays of 10 × 10 matrixes with a pitch of 50  $\mu\text{m}$ , optimal DBCO conditions for humidity and dwell time of 20% r.H., 0.1s) are shown in Figure 2.12. Here, the observed fluorescence intensity can be seen as a measure of the amount of coupled molecules. The fluorescence intensity increases with reaction time for 15 min thereafter reaching a saturation for both at 25°C and 37°C. Moreover, an elevated temperature (37°C) speeds up the reaction, thus the fluorescence intensity reaches the plateau already after 15 min incubation at 37°C, but only

after 20 min at 25°C. Beyond these time points, the obtained intensity shows only slight fluctuation which means that there is no more coupling going on and the binding attains saturation. Figure 2.12c and d exhibit the series of fluorescent images corresponding to the intensity graph in Figure 2.12a and b. All in all, we conclude that the optimal reaction condition for azide/DBCO in the probed parameter space is 15 min at 37°C, attaining the highest fluorescence intensity but consuming the lowest time.

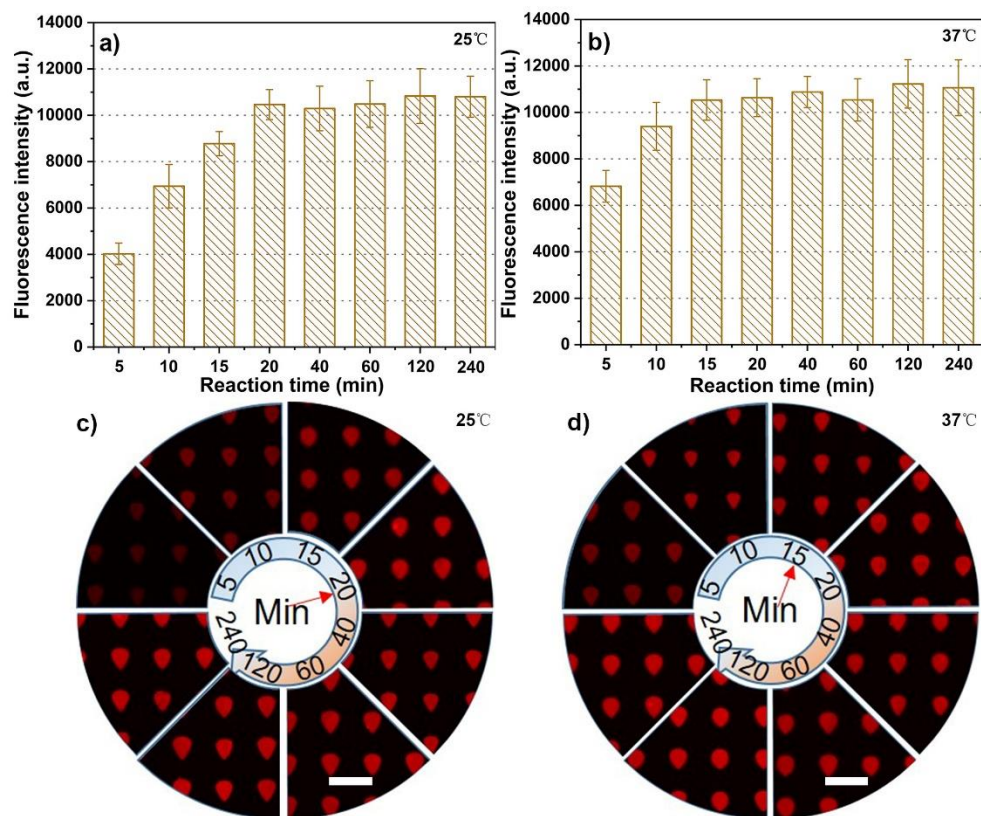


**Figure 2.12.** Relationship of the relative fluorescence intensity with the reaction times and temperatures of the DBCO-Tamra microarrays on AAPBs, a) at 25°C, b) at 37°C; c) and d) are the corresponding fluorescent images to a) and b), respectively. Exposure time for images are 5 ms, and scale bars are 50  $\mu\text{m}$ .<sup>[143]</sup>

The same approach (arrays of  $10 \times 10$  matrixes with a pitch of 50  $\mu\text{m}$ , optimal conditions for BCN of 20% r.H., 0.5 s dwell time) was then repeated to assess the reaction situation of azide/BCN. After finishing of spotting, the samples were incubated for a series of reaction times at 25°C and 37°C, respectively. The corresponding results are illustrated in Figure 2.13. The optimum reaction time for azide/BCN at both 25°C and 37°C was

prolonged to 40 min and 20 min, respectively. This is in accordance with the respective behavior in bulk labelling where such a delay possibly can be ascribed to the benzofusion in DBCO enhancing the reaction rate compared to BCN. The corresponding fluorescence microscopy images can be found in Figure 2.13c. Accordingly, the reaction time of 20 min at 37°C was deemed as optimal within the probed printing parameters for azide/BCN and was selected for further experiments in this chapter.

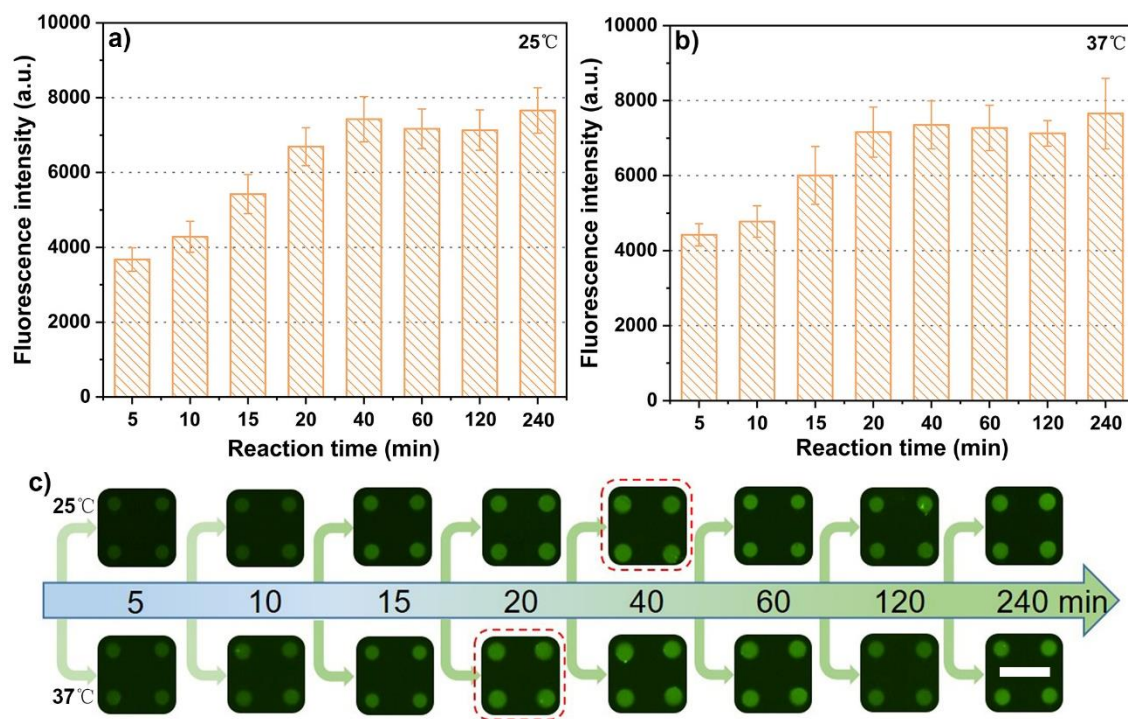


**Figure 2.13.** Relationship of the relative fluorescence intensity with the reaction times and temperatures of the BCN-FAM micropatterns on AAPBs a) 25°C, b) at 37°C; c) is the corresponding fluorescent images to a) and b). Exposure times for images are 100 ms, and scale bar is 50  $\mu\text{m}$ .<sup>[143]</sup>

#### 2.2.4. Protein binding on DBCO- and BCN-Biotin arrays

As the emission of fluorescent compounds will usually differ with modifications of the molecule, it is not straightforward to compare DBCO and BCN derivatives directly (and in our case, we chose different fluorophores (Tamra and FAM) with different spectra altogether). To enable a direct comparison of binding efficiency in regard to immobilization density we probed non-fluorescent derivatives that enable binding of the

exact same fluorophore labelled protein (streptavidin-Cy3) over biotin-streptavidin binding. Avidin and especially streptavidin has been widely used in immunoassays and other biological researches and analysis due to binding biotin with high affinity and specificity.<sup>[148]</sup>

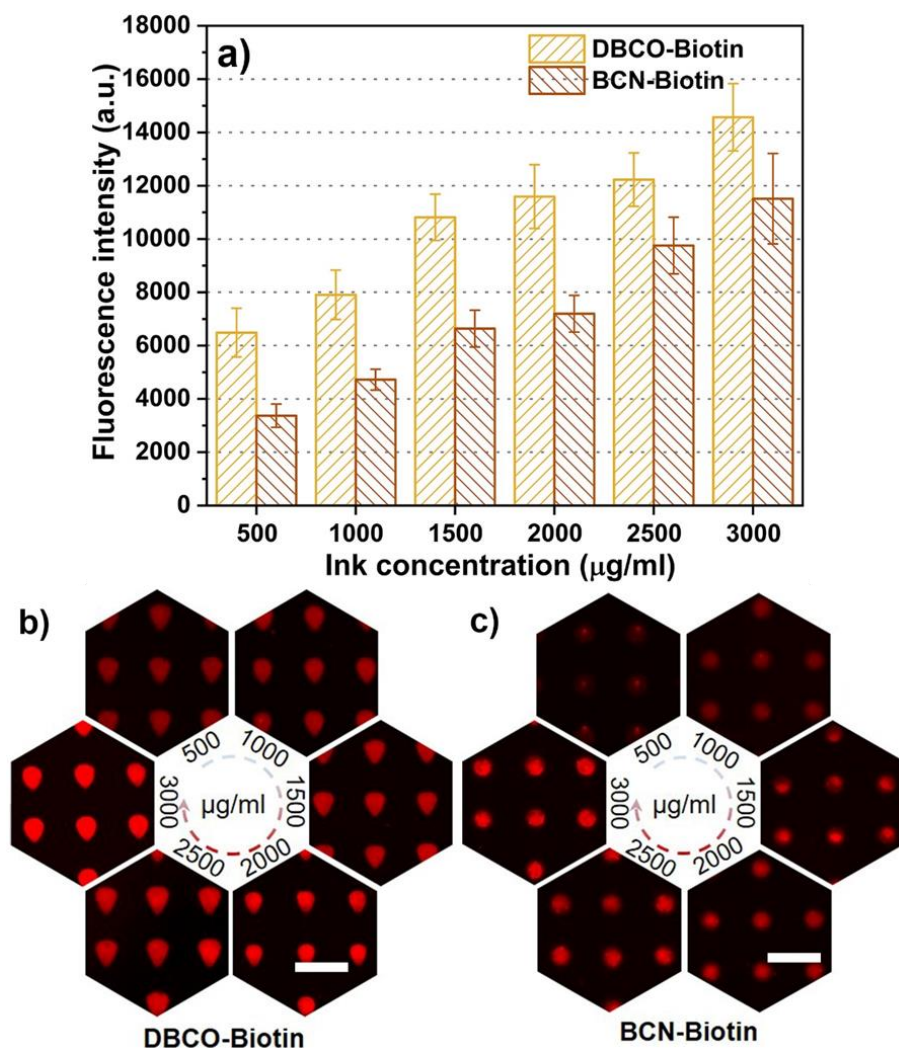


**Figure 2.14.** Influence of ink concentration on relative fluorescence intensity of a) biotins (linked with DBCO or BCN) immobilized on AAPBs after incubating with streptavidin(SA)-Cy3 at 37°C, 15 min for DBCO-Biotin, and 37°C, 20 min for BCN-Biotin. Printing settings for DBCO-Biotin of humidity was 20% and dwell time was 0.1 s, for BCN-Biotin was 20% and 0.5 s, respectively. b) and c) are the corresponding fluorescent images after incubation of SA-Cy3 for DBCO-Biotin and BCN-Biotin, respectively, and exposure times are 50 ms, and scale bars are 50 µm.<sup>[143]</sup>

To accomplish the comparison aforementioned, two types of biotin inks, DBCO-PEG<sub>4</sub>-Biotin and BCN-PEG<sub>3</sub>-Biotin, were spotted on the AAPBs with a series of concentrations from 500 to 3000  $\mu\text{g ml}^{-1}$  in  $10 \times 10$  matrixes with a pitch of 50  $\mu\text{m}$ . Straight after, before implementing the incubation step with SA-Cy3, the samples were allowed to rest at 37°C for 15 and 20 min, respectively, for the coupling of DBCO-Biotin and BCN-Biotin. The histograms in Figure 2.14a give the statistical comparison collected from the immobilized microarrays after binding with Cy3 conjugated streptavidin, and corresponding fluorescent images are shown in Figure 2.14b and c, respectively. Evidently, the fluorescence intensity gathered on DBCO-Biotin patterns is stronger than the one gathered on BCN-Biotin patterns in each ink concentration column. In details, the fluorescence intensity varies from  $(6487.24 \pm 912.93)$  to  $(14567.92 \pm 1263.81)$  for DBCO-Biotin and from  $(3368.22 \pm 438.24)$  to  $(11510.79 \pm 1698.74)$  for BCN-Biotin following the increase of ink concentration. The fluorescence intensity on the DBCO modified sample is 1.3 ~ 1.9 fold higher than on the BCN modified samples for the same concentration inks, even the molecular weight of DBCO-PEG<sub>4</sub>-Biotin ( $749.92 \text{ g mol}^{-1}$ ) is bigger than BCN-PEG<sub>3</sub>-Biotin ( $594.31 \text{ g mol}^{-1}$ ), meaning in inks of same weight concentration there are about 26% more molecules available in BCN-Biotin ink than in DBCO-Biotin ink. On the whole, considering all the observations together, molecular weight, concentration and fluorescence intensity of streptavidin linked fluorophore, we can conclude that in  $\mu\text{CS}$  the binding of azide/DBCO is more efficient than the binding of azide/BCN.

### 2.3. Summary

The work in this chapter described a systematic investigation of the coupling efficiency of small molecules delivered via  $\mu$ CS to azide functionalized diblock polymer brushes. Two representative cyclooctynes (DBCO and BCN) in fluorescent modifications and biotin derivatives were utilized in creating micropatterns by immobilization at azide groups through SPAAC reaction at different temperatures, reaction times and concentrations. The results show that higher temperature promoted the process of the click reactions and gave optimized reaction conditions for azide/DBCO and azide/BCN at 15 min (37°C) and 20 min (37°C), respectively. Importantly, by direct comparison of the SA-Cy3 fluorescence coupled to the polymer brush via biotin-DBCO and biotin-BCN, we found that the binding efficiency of the azide/DBCO coupling was significantly higher (1.3 ~ 1.9 fold) than for azide/BCN at the two reaction regimes. Therefore, our conclusions suggest using DBCO derivatives to bind with azides to attain a higher surface density of the immobilized target molecules. Our results can act as a reference for the choice of biorthogonal reagents in surface immobilization and offer important information for the fabrication of click-chemistry based microarrays.

## Chapter 3 – A fluorescent immunosensor for $\alpha$ -fetoprotein (AFP) detection

### 3.1. Introduction

Nowadays, cancer still is a leading health risk for human beings, and many people die from various cancers and related diseases every year. Among these tumor diseases, hepatocellular carcinoma (HCC), a primary liver cancer, has become the 6<sup>th</sup> most frequent occurring tumor and the 4<sup>th</sup> cancer-related deaths globally due to its unpredictability, highly malignancy, and poor prognosis.<sup>[149-152]</sup> Practically, the vast majority of the cases of HCC are diagnosed at the advanced stage and miss the optimal therapeutic period thereby.<sup>[153-155]</sup> In this instance, early diagnosis has become a crucial manner for the therapy of HCC and has drawn much attention of researchers for seeking the reliable biomarkers and establishing efficient biosensors for screening and diagnosing HCC.<sup>[10, 156]</sup>

Commonly, the ideal biomarker needs to have the ability to assist clinicians in accurately and specifically diagnosing asymptomatic patients and also can be broadly applied in screening processes.<sup>[157, 158]</sup> In the past decades, with the intensive study of the etiological mechanisms of HCC, many prognostic biomarkers have been successively identified suiting for early detection of HCC, e.g.,  $\alpha$ -fetoprotein (AFP),<sup>[153, 159]</sup>  $\alpha$ -fetoprotein-L3 (AFP-L3),<sup>[160]</sup> midkine (MDK),<sup>[161]</sup> microRNA (miRNA),<sup>[162, 163]</sup> and others.<sup>[156, 164]</sup> Among these series of biomarkers, AFP has been certified as an excellent and desirable biomarker for diagnosing HCC at the early stage, and it is also the only one that has been evaluated in a randomized controlled trial.<sup>[156]</sup> Practically, AFP is a glycoprotein with a molecular weight of about 70 kDa, and it is usually generated during fetal and neonatal development by the liver, yolk sac, and in the gastrointestinal tract.<sup>[165]</sup> Importantly, compared with other malignant tumors, the cases of HCC usually show an elevated serum level of AFP.<sup>[10, 166]</sup> Therefore, specific and sensitive detection of AFP is an effective and reliable approach for achieving early HCC treatment.

Plenty of scientific and technological manners have been developed for the diagnosis and early treatment of HCC based on AFP detection, including radioimmunoassay

(RIA),<sup>[167]</sup> electrochemical immunoassay (ECIA),<sup>[168]</sup> surface plasma resonance (SPR),<sup>[169-171]</sup> and enzyme-linked immunosorbent assay (ELISA),<sup>[172, 173]</sup> among others.<sup>[174-176]</sup> Apart from these methods, fluorescent immunosensors have also been extensively recognized for advantages concerning low cost, facile, and high sensitivity.<sup>[10, 166]</sup> Thus, they have been popularized in many research fields, e.g., cell screening, protein detection, DNA detection, and clinical diagnostics.<sup>[6, 177, 178]</sup>

As aforementioned, the fluorescent immunosensor plays an important role in detecting biomarkers for disease diagnosis. Specifically, an important consideration of biosensor fabrication is to select a suitable substrate for sensor platform construction. In addition, another main issue of biosensors during the detection process is the unspecific biofouling, which usually interrupts the collection of target signals by enhancing the ratio of signal-to-noise. Normally, functional inert proteins (e.g., bovine serum albumin (BSA), fetal bovine serum (FBS), goat serum, or casein) are kinds of popular biomacromolecules used for biosensors as interface passivators to prevent unspecific protein fouling.<sup>[63]</sup> In principle, the antifouling property of the interface is only endowed after the surface or the unreactive area is saturated with these proteins.<sup>[48]</sup> However, in some cases, the efficiency of the specific receptors or the reactive sites, which are needed for post-treatment, bound to the surface would be impaired by these proteins, and they can even cause undesired responses on their own.<sup>[179]</sup> Therefore, platforms made up of antifouling polymer brushes are prospective candidates for meeting the need for protein repellency and avoiding the drawbacks caused by inert proteins.<sup>[142, 180]</sup> Especially the hierarchical polymer brushes containing an antifouling block together with a reactive block show great promise in presenting antifouling performance and reactive sites for post-processing.<sup>[142, 181]</sup>

In this chapter, we developed a facile and reliable fluorescent biosensor for AFP detection through the combination of directly immobilized antibody microarray spotted by  $\mu$ CS (forming amide bonds, NHS/amino) on antifouling polymer brushes and the high specificity of antigen/antibody interaction. To realize this approach, AAPBs were employed as a platform to support capture arrays (DBCO-NHS ester), which were spotted by  $\mu$ CS, for the direct antibody binding strategy (NHS/antibody). In addition, DBCO-Biotin was also printed on AAPBs to construct sandwich structures

(biotin/streptavidin/biotin-antibody) for a comparison with an indirect antibody binding strategy. As shown in Figure 3.1, the AAPBs consist of two functional segments, the poly(OEGMA) block is synthesized at the bottom displaying superior antifouling performance; the top block (poly(GMA)/azide) is rich in reactive azido groups, which can immobilize the DBCO-compound arrays per SPAAC reaction efficiently and mildly.<sup>[182]</sup> The binding conditions of NHS/amino and antibody/antigen in probed spaces were investigated at different temperatures (25°C and 37°C) and reaction durations. Additionally, the sensitivity of the sensor based on the direct binding strategy (NHS/antibody/AFP) was evaluated at the optimal detection conditions by fluorescence imaging, and a visualized comparison with the indirect binding strategy (biotin/streptavidin/biotin-antibody/AFP) was also implemented.

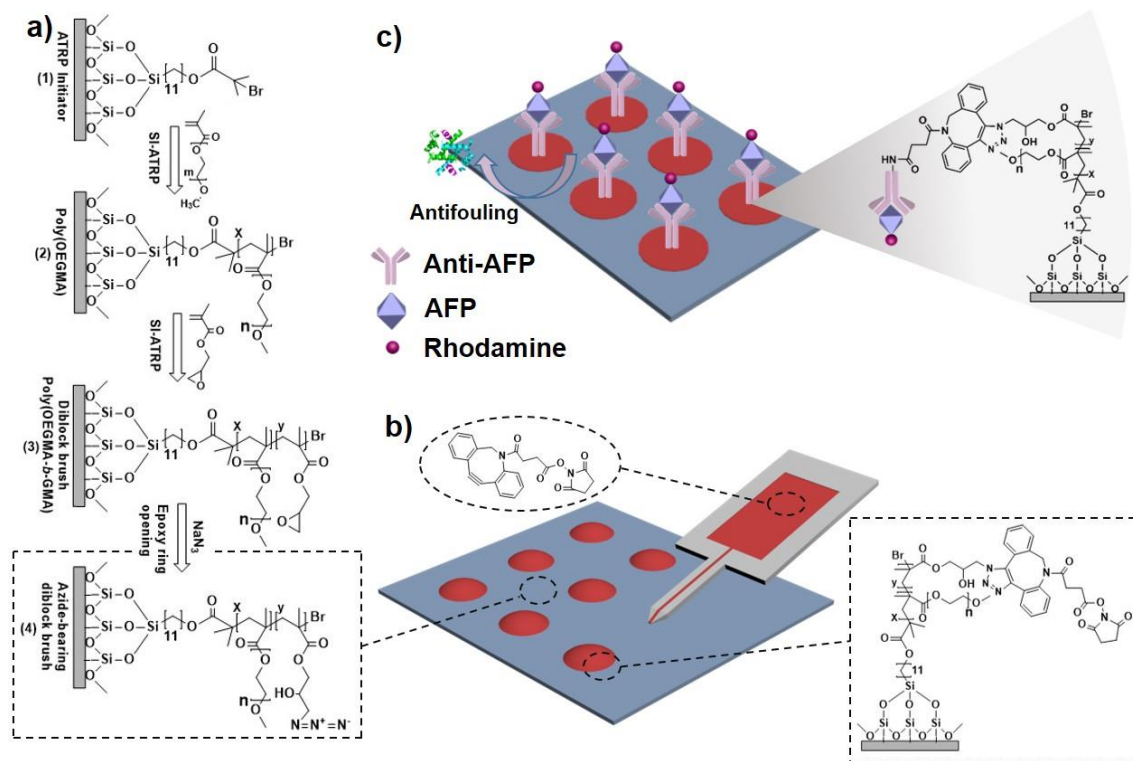


**Figure 3.1.** Schematic representation of a) the AAPBs synthesis progress, b) immobilization of DBCO-NHS ester capture arrays on AAPBs via  $\mu$ CS, c) AFP detection through direct binding strategy.

## 3.2. Results and discussions

### 3.2.1. Immobilization of DBCO-derivative capture arrays on AAPBs

In this chapter, DBCO-NHS ester or DBCO-Biotin patterns ( $10 \times 10$  matrixes with a pitch of  $50 \mu\text{m}$ ), which act as antibody capture arrays, were printed to AAPBs via  $\mu\text{CS}$  at a dwell time of 0.1 s and relative humidity of 20%. After printing, the arrays were allowed to click to the surface per SPAAC reaction at  $37^\circ\text{C}$  for 15 min, based on the results obtained in chapter 2. The physical and chemical characterization of the AAPBs can be found in 2.2.1 and 2.2.2.

### 3.2.2. Construction of antibody arrays

It is well known that the NHS ester species have a strong affinity to  $-\text{NH}_2$  groups, which are in the side chain of the lysine residues of proteins, and the steady amide bond between them can be easily formed in weakly alkaline conditions (pH 7 ~ 9).<sup>[10]</sup> Herein, the amide formation reaction was implemented in an alkaline PBS solution (pH 8.4), yet the NHS ester groups will hydrolyze initially and compete to the primary amino groups in the protein or antibody scaffold to generate amide bonds. In case of the adverse effects of the residual NHS ester groups after incubation of protein, an  $\text{NH}_2\text{-PEG}_4\text{-NH}_2$  solution (1:100 in PBS, pH 8.4, v/v) was incubated on the samples to quench the possibly surviving NHS ester moieties at the patterns. As can be seen, the NHS ester groups in the capture arrays are the key contribution to the direct anchoring of the specific antibody, which is used for AFP sensing. Consequently, we tried to test the optimal reaction conditions (temperature and time) between the NHS ester and the  $-\text{NH}_2$  groups in  $\mu\text{CS}$  spotted area for anchoring antibody adequately. For doing so, we employed Alexa Fluor647 labeled streptavidin (SA-AF647), which is also a protein and rich in amino groups and easy to access, to implement the test trials involving amide bond formation. As illustrated in Figure 3.2, the samples bearing capture arrays were bound to SA-AF647 at  $25^\circ\text{C}$  (room temperature) and  $37^\circ\text{C}$  (physiological temperature) for various reaction durations, respectively. Figure 3.2a shows the fluorescence intensity collected at different reaction conditions, and the corresponding fluorescent images are shown in Figure 3.2b. As here, the detected fluorescence intensity at different reaction conditions can be considered as a direct measure of the amount of the

bound molecules. It was noticed that with the lengthened reaction time, the fluorescence intensity raises at both incubation temperatures, while a plateau at the incubation regime of 37°C appears already after 20 min, but 40 min for the route of 25°C. Hereafter, we only observed minor fluctuation of the intensity, which means that the amount of the coupled protein on capture arrays has reached its saturation state and cannot be raised anymore even with extended reaction time. Therefore, we deduced that the optimum reaction condition for binding primary amine to HNS ester, that is, forming the amide bonds, in this work is at 37°C for 20 min, which exhibits the highest bound amount and avoids time consumption simultaneously. The spot size distribution calculated by the sample, which was treated at the optimal reaction conditions, is shown in Figure 3.2c. According to the discussion, the binding parameter 37°C/20 min was employed for the direct binding strategy (NHS/antibody) for anti-AFP fixing and for further experiments. In addition, concerning the indirect binding strategy (biotin/streptavidin/biotin-antibody), streptavidin was used for constructing sandwich structures for linking biotin-(anti-AFP) to DBCO-Biotin arrays by 37°C/30 min, in line to the parameters used in chapter 2.

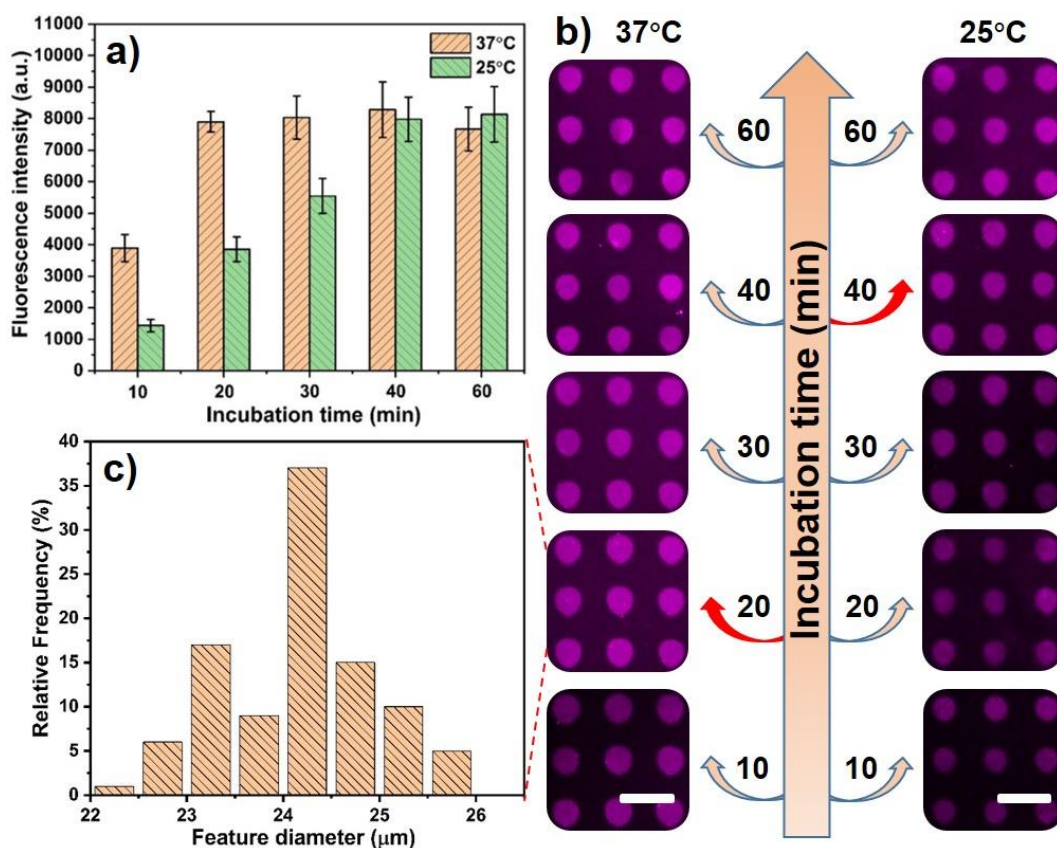


**Figure 3.2.** a) Relationship of the relative fluorescence intensity at different reaction times and temperatures of Alexa Fluor647 labeled streptavidin (SA-AF647) incubated on DBCO-NHS ester capture arrays on AAPBs, b) the corresponding fluorescent images at 37°C (right) and 25°C (left) with different reaction intervals, c) the feature size distribution (here denoted by spot diameter) on the sample treated at the optimum condition, 37°C/20 min. Exposure times for images are 1 s. Scale bars are 50  $\mu$ m.

### 3.2.3. Detection of fluorescently labeled AFP

By means of the optimal reaction conditions (37°C/20 min) between primary amine and NHS ester moieties, a specific antibody (anti-AFP, polyclonal) for AFP detection was coupled to the capture patterns through forming of amide bonds, i.e., the direct antibody anchoring strategy. Sequentially, to deactivate the possibly survived NHS ester moieties after antibody anchoring, a solution of NH<sub>2</sub>-PEG<sub>4</sub>-NH<sub>2</sub> (1:100 in PBS, pH 8.4, v/v) was used on the samples. After that, detection of AFP antigen by antibody microarrays was explored by use of rhodamine-labeled AFP at 25°C and 37°C with different intervals to establish the optimal parameters for efficient and rapid AFP detection. The related results are illustrated in Figure 3.3. As we can see from Figure 3.3a, the fluorescence intensity (deemed as a measure of the amount of the coupled AFP-rhodamine) at two detection temperature conditions are both going up following the prolonged incubation durations before a plateau appears after 20 min incubation at 37°C and after 40 min at 25°C. Thus, the elevated temperature accelerates the protein binding process. Hereafter, the fluorescence intensity maintains around a steady level, hence the upper limit of the coupled AFP attains at these parameters. The corresponding fluorescent images are shown in Figure 3.3b. Consequently, in this chapter, the parameters for protein detection were fixed at 37°C/20 min for both the direct and the indirect binding strategies to accomplish a fast and reliable biomarker detection.

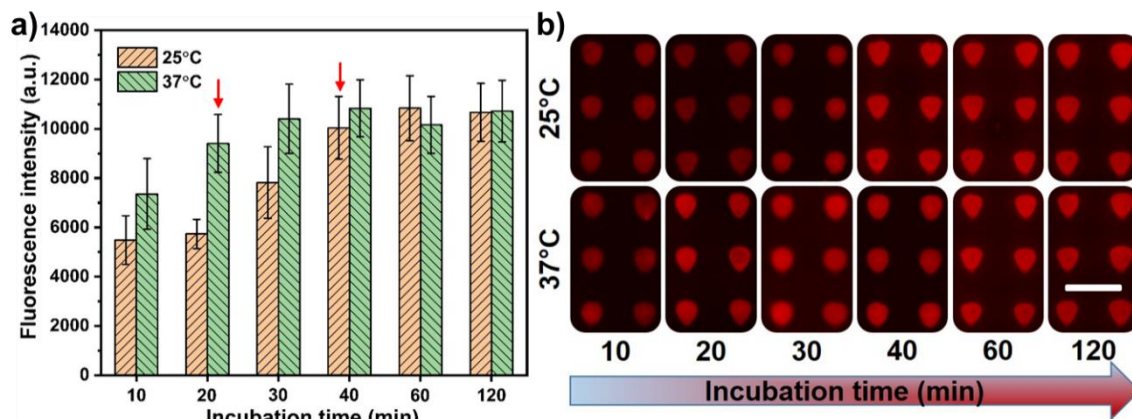


**Figure 3.3.** Detection of AFP antigen. a) Relationship of the relative fluorescence intensity with different incubation times and temperatures of rhodamine-conjugated AFP on directly immobilized anti-AFP arrays on AAPBs, b) the corresponding fluorescent images with different reaction times at temperatures of 25°C (top) and 37°C (bottom). Exposure times for images are 100 ms. The scale bar is 50  $\mu$ m.

To confirm that the AFP only binds to the specific antibodies immobilized at the capture arrays, isotype controls were carried out on nonspecific IgG antibody (anti-IgG) modified patterns after passivating by  $\text{NH}_2\text{-PEG}_4\text{-NH}_2$ , and the results are shown in Figure 3.4. Figure 3.4a confirms that the isotype control-IgG was immobilized to the capture arrays (DBCO-NHS ester) as the FITC conjugated secondary antibody is visible in the green channel. While, when incubating AFP-rhodamine on a sample prepared in parallel with the sample shown in Figure 3.4a, and not incubated with the second antibody, but passivated by  $\text{NH}_2\text{-PEG}_4\text{-NH}_2$  (Figure 3.4b and c), no signal could be observed either in the green or in the red fluorescence channel. This means that no AFP was captured by anti-IgG patterns, as expected. In addition, to certify that the polymer brush substrate only insignificantly affects the detection process, DBCO-NHS ester spots were written on it and then passivated by  $\text{NH}_2\text{-PEG}_4\text{-NH}_2$ , following incubation of AFP-rhodamine. As shown in Figure 3.5c, no fluorescent signal is visible. Therefore, the polymer brush substrate does not negatively influence the detection process in this work.

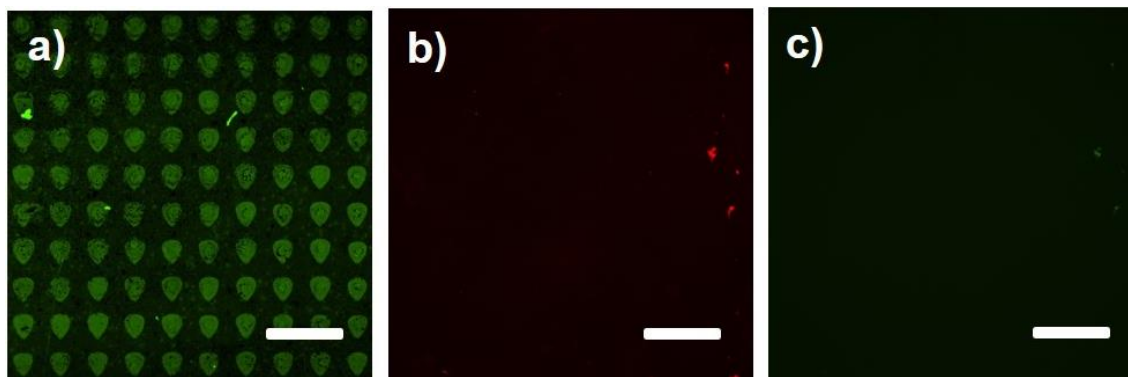


**Figure 3.4.** Isotype control experiments on IgG antibody functionalized arrays (direct binding regime). a) Coupled with FITC linked 2<sup>nd</sup> antibody. Images captured at b) red and c) green channel after incubation of AFP-rhodamine on IgG antibody functionalized arrays. Exposure times of the samples are 1 s. Scale bars are 100  $\mu\text{m}$ .

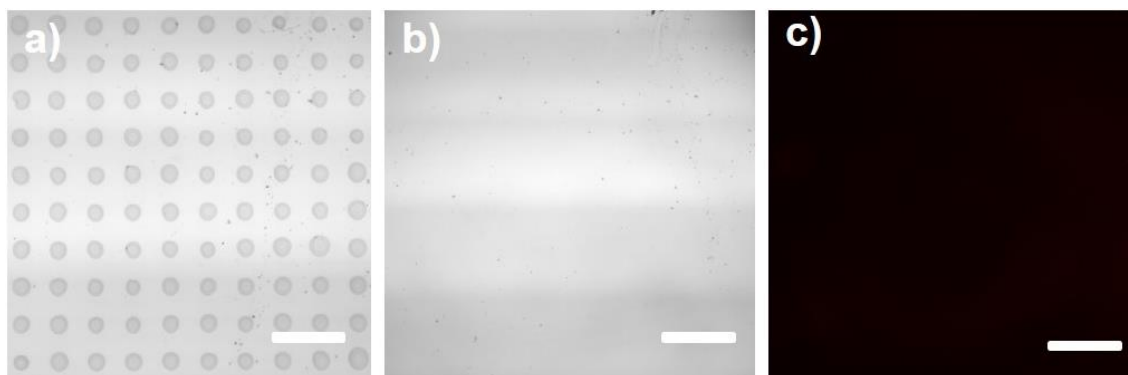


**Figure 3.5.** Negative control experiments on AAPB surfaces. Bright field images of the DBCO-NHS ester arrays on AAPB substrate, a) after printing by  $\mu\text{CS}$ , and b) after washing with PBS. c) Image captured at red channel after incubation of  $\text{NH}_2\text{-PEG}_4\text{-NH}_2$  and AFP-rhodamine sequentially on the sample shown in (a) and (b). The exposure times are 1 ms for a) and b), 100 ms for c). Scale bars are 100  $\mu\text{m}$ .

### 3.2.4. Sensitivity evaluation

According to reaction and detection parameters exploited in the previous two sections, in this section, a comparison between the direct antibody anchoring strategy (NHS/anti-AFP), which is facile, compact, and omits the construction of tediously traditional sandwich structures (biotin/streptavidin/biotin), and the indirect antibody anchoring strategy (biotin/streptavidin/biotin-antibody) in AFP detection is presented. The sandwich structure based approach is named here as the indirect antibody binding strategy. To assess these two strategies visually, fluorophore linked AFP with different concentrations was incubated at the optimal reaction and detection conditions on anti-AFP arrays, which were immobilized either by direct binding regime or indirect binding regime on AAPBs. Figure 3.6 shows the summary of the results of the sensitivity evaluation by the two detection regimes, and the corresponding fluorescent images are shown above the curves. Evidently, at the high-concentration part (i.e., higher than 100  $\mu\text{g/mL}$ , Figure 3.6a and b), the fluorescence intensity at both regimes shows no significant difference. While, when extrapolating the low-concentration section (Figure 3.6c and d, both considered four data points) with linear fitting ( $y = 419.60 + 99.62x$  for the direct binding strategy,  $y = 499.56 + 43.09x$  for the indirect binding strategy) of the curves, and taking into consideration the fluorescence background ( $766.37 \pm 106.36$  a.u.) of the substrate in the experiments, the sensitivity limits of AFP detection by our chips at the given conditions are obtained at 3.47  $\mu\text{g/mL}$  and 6.19  $\mu\text{g/mL}$  for the direct and indirect regimes, respectively. Consequently, the sensitivity of the direct-regime sensor, binding anti-AFP directly to DBCO-NHS ester capture arrays via the formation of amide bonds, is 44% higher than the indirect regime, which binds anti-AFP through biotin/streptavidin/biotin sandwich structures. The results proved that the proposed direct binding strategy for AFP detection by  $\mu\text{CS}$  written capture arrays on azide-bearing antifouling polymer brushes is quantitative and even outperforms the more complicated indirect approach. Moreover, our design provides a new route for biosensor construction and shows a great perspective on biomarker detection in general.

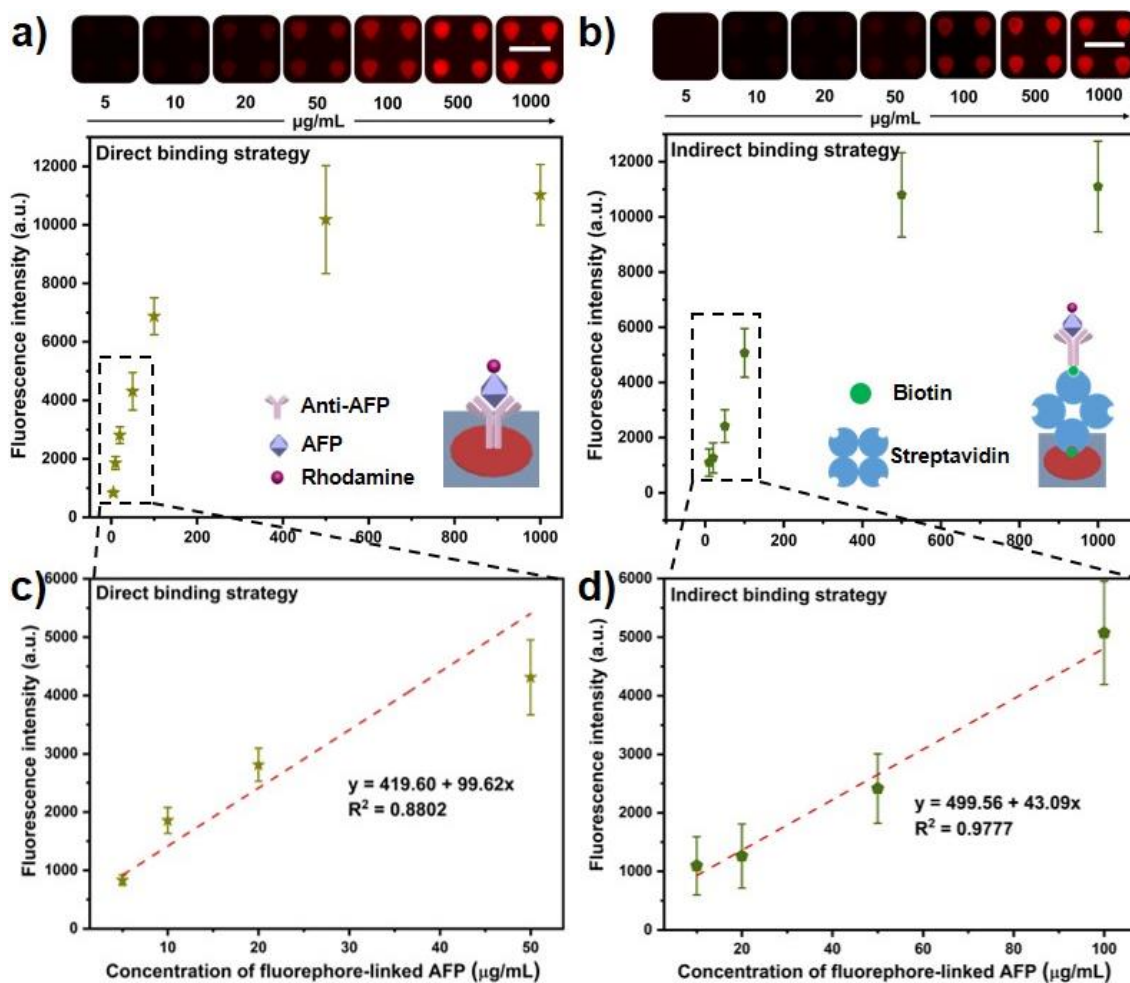


**Figure 3.6.** Sensitivity evaluation of AFP detection by antibody microarrays on AAPB substrates. The fluorescence intensity was collected on samples incubated with different concentrations of rhodamine labeled AFP, a) was based on the direct binding strategy (NHS/antibody/AFP), b) was based on the indirect binding strategy (biotin/streptavidin/biotin-antibody/AFP). All the reactions were implemented in the optimal situations. The above images are the corresponding fluorescent images concerning different AFP concentrations, and the cartons in the low right corner are the illustrations of the two regimes. c) and d) are the linear fitting curves of the detected fluorescence intensity at low concentrations ( $\leq 100 \mu\text{g/mL}$ ) corresponding to (a) and (b), respectively. The exposure times are 100 ms, the scale bars are  $50 \mu\text{m}$ .

### 3.3. Summary

The work in this chapter presented a facile and reliable immunosensor for AFP detection by fluorescence imaging on site-specifically functionalized cyclooctyne derivative patterns on AAPBs. The spotted DBCO-NHS ester micropatterns, which were immobilized to AAPBs via SPAAC reaction, were employed as capture arrays for anchoring of anti-AFP through forming of amide bonds. The conditions of amide bond formation (NHS/ amino) and the AFP detection process were tested at different reaction durations and temperatures on capture arrays. The results show that the optimal performance of NHS/amino and antibody/AFP coupling was yielded at elevated temperatures. Importantly, a sensitivity comparison of AFP detection was implemented between the direct binding strategy (NHS/antibody/AFP) and the indirect binding strategy (biotin/streptavidin/biotin-antibody/AFP). We found that the estimated sensitivity of the direct binding strategy was 3.47  $\mu\text{g/mL}$ , which is around 44% higher compared with the indirect binding strategy. All in all, our study proposes a novel and facile fluorescent immunosensor for AFP detection, combining click chemistry and amide reaction as well as antifouling polymer brushes. Compared to the costly and tediously traditional sandwich-type sensing approaches, our design may bring forward a new perspective for biomarker detection.

## **Chapter 4 – Signal-to-noise ratio improvement on diamond surfaces in fluorescence imaging by methacrylate-based polymer brush coating**

### **4.1. Introduction**

Over the past decades, diamonds, especially fluorescent nanodiamonds, have drawn great attention in biological and medical applications, e.g., fluorescence imaging,<sup>[183-185]</sup> drug delivery,<sup>[186, 187]</sup> quantum sensing,<sup>[188]</sup> and tissue engineering,<sup>[189, 190]</sup> due to their auto-fluorescence, non-toxicity, biocompatibility, and easy functionalization.<sup>[191, 192]</sup> The spontaneous fluorescence is a crucial characteristic of diamond materials derived from nitrogen-vacancy centers (NV).<sup>[193]</sup> A NV is a crystal lattice defect,<sup>[194]</sup> i.e. a center consists of a substitutional nitrogen atom located adjacent to a carbon vacancy,<sup>[195]</sup> thus exhibiting stable photoluminescence, resisting photobleaching and photoblinking. Consequently, nanodiamonds are extensively used as sensitive and specific fluorescent probes for bio-imaging<sup>[190, 196]</sup> and fluorescent-read sensors.<sup>[197, 198]</sup>

Fluorescence imaging is a popular and cost-effective characterization technique in biomedical studies, and it holds advantages over other imaging methods, e.g., high sensitivity, excellent resolution, low background and high signal-to-noise ratio.<sup>[195]</sup> Moreover, as a non-invasive tracing approach, fluorescence imaging provides a gentle manner to trace or visualize target biological processes in living organisms.<sup>[190, 199]</sup> By means of the remarkable advantages, diamond materials or nanodiamonds crucially contribute to the development and progress of fluorescence imaging in biological research. However, in certain cases, diamond emits only a weak fluorescence signal and generates a higher background, which makes target observation hard, thus limiting their applications in bio-imaging to some extent.<sup>[200, 201]</sup> In addition, diamonds without any interface modification usually can precipitate in biological media or adhere to not targeted proteins or biomolecules, thus bringing obstacles and interferences to the observations.<sup>[202, 203]</sup> To overcome these limitations and improve the final signal-to-noise ratio of diamond-based biosensors or bioprobes, different types of surface modification methods have been

developed, e.g., initial surface termination,<sup>[204, 205]</sup> noncovalent and covalent modification.<sup>[206-208]</sup> Coating diamond by covalent modification, for example, grafting polymer brushes as a functional film, is a promising way because the polymer-based coatings are biocompatible, hydrophilic and nontoxic.<sup>[209, 210]</sup> Moreover, polymeric structure and functionality can be modulated according to the specific need. Polymer brush coatings equipped with protein-repellent segments, e.g., poly(N-(2-hydroxypropyl)-methacrylamide) (HPMA),<sup>[211]</sup> poly(ethylene glycol) (PEG)<sup>[212]</sup> and carboxybetaine methacrylamide,<sup>[213]</sup> usually exhibit excellent antifouling properties without impeding the inherent features of the diamond. Further functionalizations by polymer-based coatings have also been demonstrated, e.g., introducing epoxide, azide or alkyne species to polymer brush scaffold to combine protein repellency and click chemistry.<sup>[184]</sup> In general, PEGylated coatings are employed to modify substrates to obtain desirable properties and functions. However, in living tissue conditions, the hydroxyl groups in the PEG side chain are prone to be oxidized to aldehydes by enzymes. In this condition, the proteins tend to attach to these aldehydes and generate side effects, thus loss of functions of polymers.<sup>[39, 84, 214]</sup> These weaknesses of PEGylated modifications are commonly called the “PEG dilemma”.<sup>[82, 206]</sup> Coincidentally, methacrylate-based polymers, e.g., poly(HPMA), are not troubled by such immune reactions. Poly(HPMA) is a non-immunogenic and eco-friendly polymer. Moreover, poly(HPMA) has a linear skeleton structure, and its side chain is easy to be functionalized, thus popularization in many fields.<sup>[215, 216]</sup>

In this chapter, to reduce the undesirable protein fouling and thus decrease the optical background of the oxidized diamond surface, a methyl methacrylate (MMA)-based alkyne-bearing antifouling polymer brush, poly(HPMA-*b*-AlkMA), was employed in combination with  $\mu$ CS (Figure 4.1). The polymer brush was immobilized through the “grafting from” method, which offers a dense and thickness controllable film coating.<sup>[65, 143]</sup> The copolymer chain was created by conventional radical polymerization with azobis(isobutyronitrile) (AIBN) as initiator, which avoids using toxic metal catalysts.<sup>[209]</sup> Detailedly, two different types of segments exist in the scaffold of the copolymer, poly(N-(2-hydroxypropyl)-methacrylamide) (HPMA) and poly(propargylacrylamide) (AlkMA). Poly(HPMA) is a broadly used hydrophilic and biocompatible polymer, which provides antifouling properties and constitutes the main structure of the copolymer. The poly(AlkMA) segment

was used to introduce alkyne groups to the copolymer structure. These alkyne groups are great candidates for copper-catalyzed alkyne-azide cycloaddition (CuAAC) reaction and are capable to attach different molecules or compounds to the coating surface. Therefore, the poly(HPMA-*b*-AlkMA) maintains protein-repellent without any additional background saturation and enables highly specific chemical functionalization by click chemistry, which is fast, mild, and highly efficient.

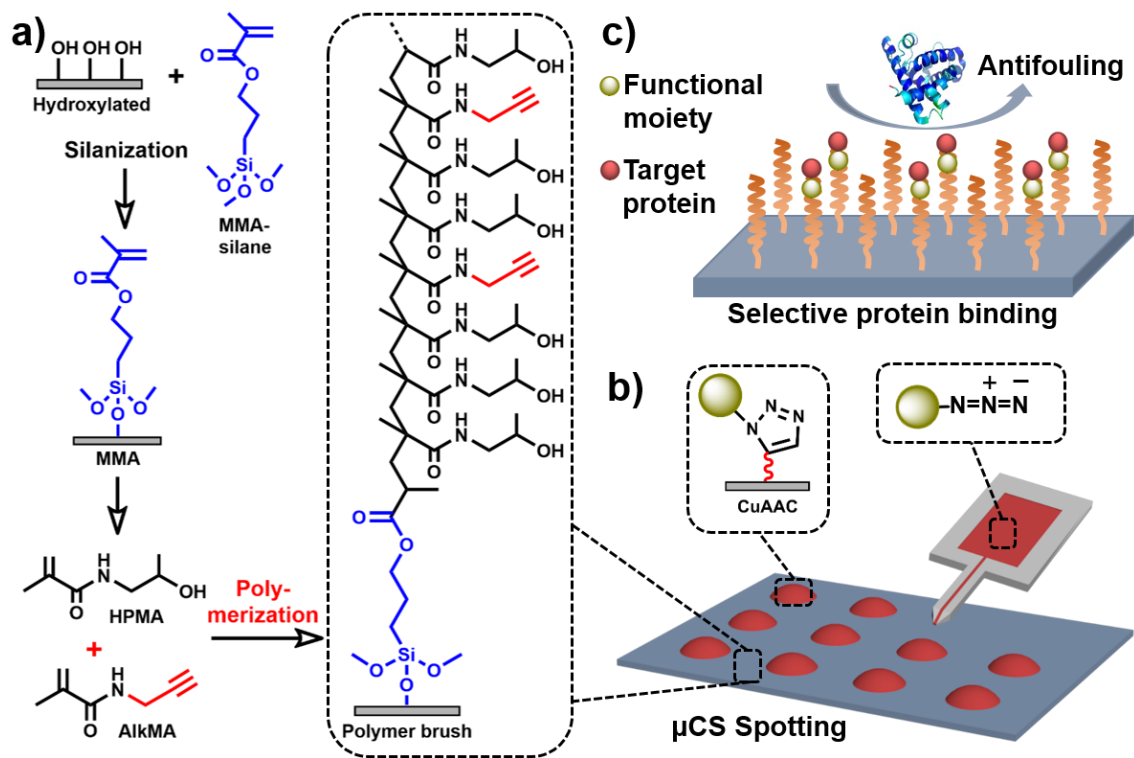


**Figure 4.1.** Schematic illustration of the chemical structure and  $\mu$ CS functionalization strategy of the poly(HPMA-*b*-AlkMA) polymer brushes. a) The fabrication route of the methacrylate-based alkyne-bearing antifouling polymer brushes. b) Creation of micropatterns by  $\mu$ CS on the reactive polymer brushes surface. c) Selective binding of a target protein to the site-specifically functionalized polymer brushes surface.

## 4.2. Results and discussions

### 4.2.1. Optimization of the polymerization procedure and properties of polymers

Both methacrylate-terminated glass and diamond substrates were modified with mixture of HPMA and AlkMA *via* conventional random radical polymerization to grow a dense layer of poly(HPMA-*b*-AlkMA). The resulting surfaces should exhibit excellent

antifouling properties by the HPMA segments and contain alkyne groups that can bind azide derivatives by CuAAC reactions. For a basic check on the functionalization, each step was monitored by static water contact angle (WCA), atomic force microscopy (AFM) and ellipsometry. The results are summarized in Table 4.1 and Figures 4.2 and 4.3.

**Table 4.1.** Summary of physical characterization (WCA, roughness and thickness) of the film coatings. Every mean value with standard deviation was counted from 3 random measurements.

Items	WCA [°]	Roughness [nm]	Thickness [nm]*
Bare glass slide	45.2 ± 3.6	0.148 ± 0.026	--
Bare diamond surface	57.6 ± 2.3	0.187 ± 0.072	--
MMA-silanized on glass	66.3 ± 2.2	0.251 ± 0.031	1.56 ± 0.06
on diamond	65.6 ± 1.8	0.232 ± 0.066	--
Poly(HPMA- <i>b</i> -AlkMA) on glass	62.1 ± 3.9	1.682 ± 0.183	3.97 ± 0.11
on diamond	62.3 ± 3.1	1.033 ± 0.221	--

\*Films thickness was measured on silicon samples prepared in parallel with glass samples. The polymerization was implemented for one day for all samples.

WCA and surface roughness (root-mean-square roughness average, Ra) characterizations are the two common and facile approaches to monitor the process of surface modification, because the surface tension and topography change when new substances are added to the material surface. As shown in Table 4.1 and Figure 4.2, the WCA and roughness values of the bare glass surface are 45.2° and 0.148 nm, respectively. After silanization by methyl methacrylate on the glass surface, these values increase to 66.3° and 0.251 nm, respectively. In addition, the ellipsometric thickness of the MMA-silanized sample is 1.56 nm, which is also consistent with the self-assembled monolayer. After implementing polymerization, the roughness and thickness increase to 1.682 nm and 3.97 nm, respectively, while a slight decrease in WCA (62.1°) was observed. A same tendency of WCA and roughness change was found on diamond-based samples (Figure 4.3).

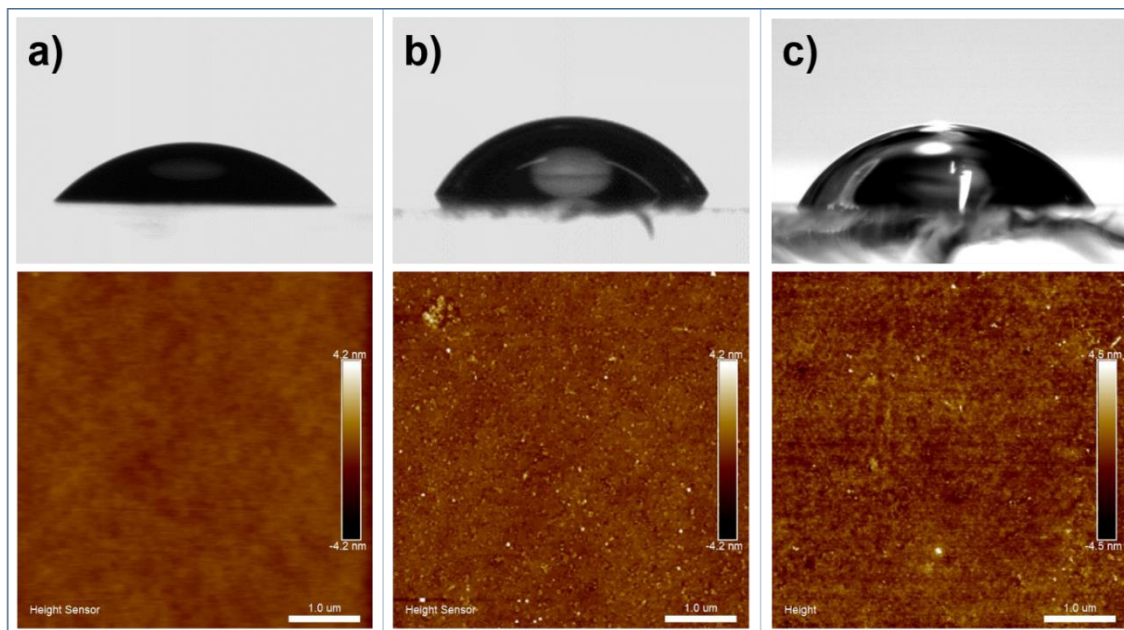


**Figure 4.2.** Corresponding static WCA (top) and AFM images (bottom) of glass-based samples. a) Bare glass, b) MMA-silanzed, c) poly(HPMA-*b*-AlkMA) modified.

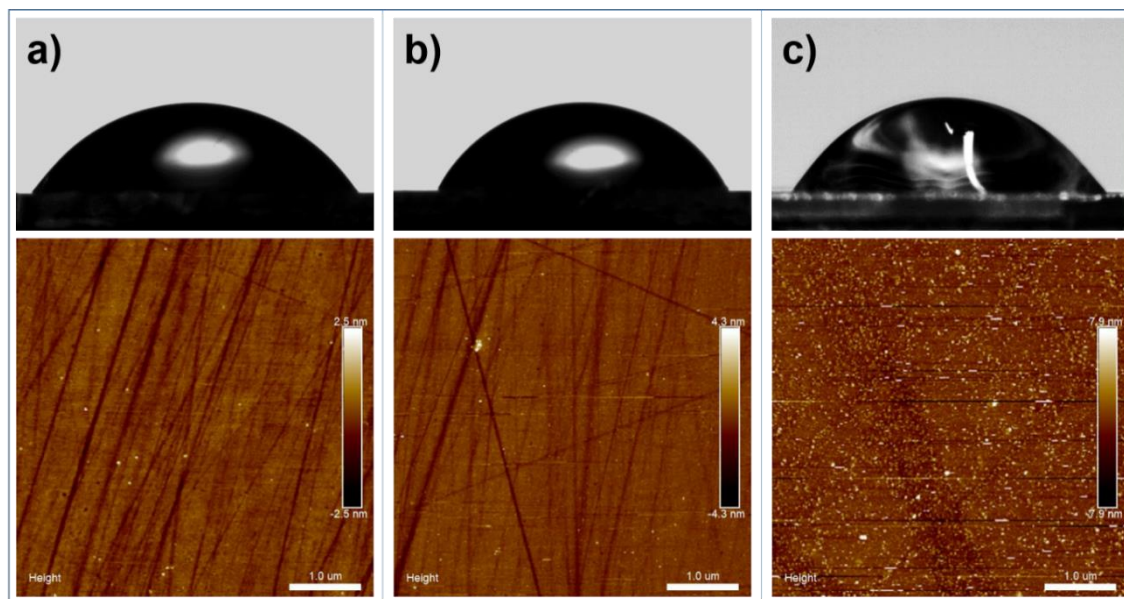


**Figure 4.3.** Corresponding static WCA (top) and AFM images (bottom) of diamond-based samples. a) Bare diamond, b) MMA-silanzed, c) poly(HPMA-*b*-AlkMA) modified.

To further confirm the chemical functionalization steps, x-ray photoelectron spectroscopy (XPS) was performed on the samples. After MMA-silanization the sample surface shows three peaks at 285.0 eV, 286.4 eV, and 288.9 eV, which are derived from (C–C, C–H), (C–O), and (O–C=O), respectively (Figure 4.4). Comparing the XPS spectra in the C 1s region of the bare glass slide and MMA-silanized surface, the (C–O):(C–C, C–H) ratio increases from 0.21 to 0.45, which indicates a successful silanization process. XPS analysis of the C 1s region of poly(HPMA-*b*-AlkMA) shows signals assigned to (C–N) and (N–C=O) at 286.3 eV and 288.4 eV, respectively, derived from the amide component in the polymer skeleton.<sup>[217]</sup> As shown in Figure 4.4b, three main element signals are considered in the wide-scan spectrum of poly(HPMA-*b*-AlkMA), i.e. O 1s (530.7 eV), C 1s (288.7 eV), and N 1s (403.4 eV) in a 4:9:1 ratio. Considering the possibility of atmospheric contamination, this result is consistent with the elemental composition of the poly(HMPA) structure (2:7:1).<sup>[211]</sup> In addition, a single peak at 400.3 eV in the N 1s spectrum also confirms the amide nitrogen in the polymer chain (Figure 4.5).<sup>[217]</sup>

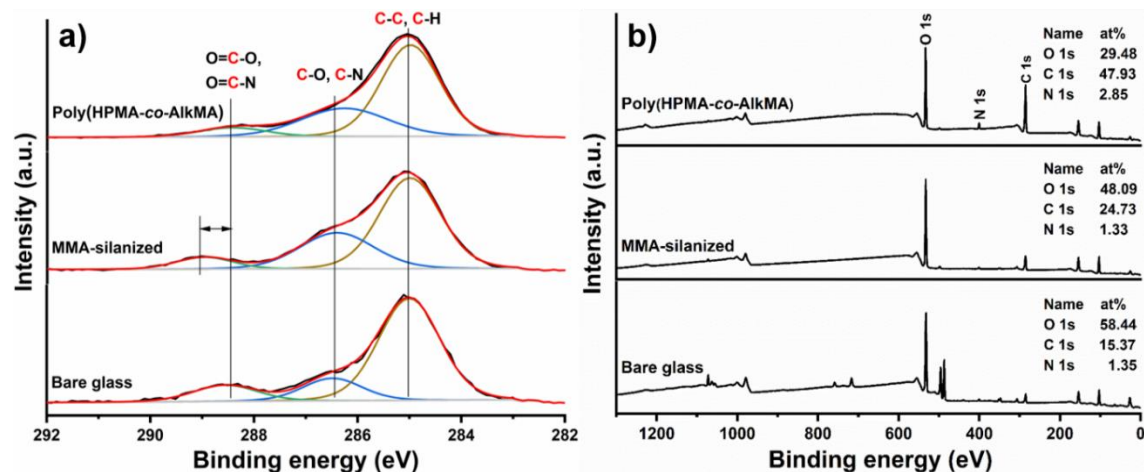


**Figure 4.4.** XPS characterization of different surfaces on glass substrates, a) at C 1s region, b) wide-scan spectra. The components resulting from corresponding chemical species are highlighted in red.

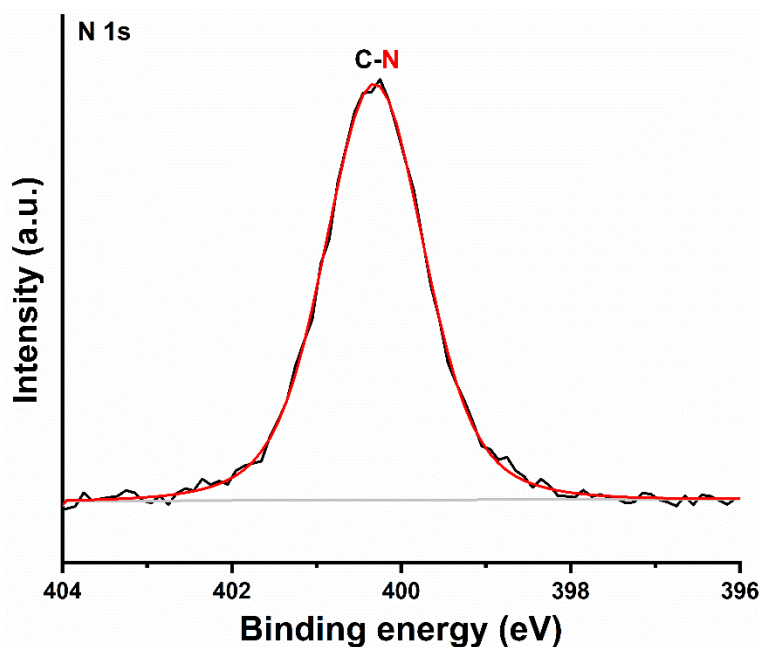


**Figure 4.5.** XPS characterization at N 1s region of poly(HPMA-*b*-AlkMA) surface on glass substrates.

#### 4.2.2. Evaluation of antifouling properties and reactivity of the polymer brushes

The general scheme of the poly(HPMA-*b*-AlkMA) polymer-brush-coated substrate preparation and patterning of azide ink arrays by  $\mu$ CS is given in Figure 4.1. In order to first verify the antifouling properties and the reactivity toward CuAAC reaction, polymer brushes were prepared on a glass surface. Afterwards, the polymer brushes were grown on a diamond surface at the optimal preparation conditions to assess the background and signal-to-noise ratio on it by fluorescence imaging. During printing, the tip was allowed to touch the substrate, allowing ink to flow from the ink reservoir to the substrate to generate micropatterns in a controlled environment. Each of the spots acts as a microreactor allowing the CuAAC reaction to take place between azide moieties and alkyne terminals on the polymer brush substrate. The azide-containing inks were mixed with catalysts of copper sulfate ( $\text{CuSO}_4$ ) and sodium ascorbate (Na-As) to facilitate the CuAAC reaction. The samples were left overnight at room temperature in the dark to ensure the completion of the click reaction. After that, the samples were washed with PBS to remove the excess ink residue prior to evaluation by fluorescence imaging or further use.

To validate the CuAAC reaction on poly(HPMA-*b*-AlkMA) polymer-brush-coated glass substrate and also to characterize the resulting arrays, a fluorescent ink, Tamra-azide, was

printed, followed by evaluation on a fluorescence microscope. Figure 4.6 shows the images of Tamra-azide functionalized micropatterns before (Figure 4.6a and b) and after (Figure 4.6c and d) washing with PBS solution and their fluorescence intensity comparison (Figure 4.6e). After washing, the pattern is still visible in the fluorescence channel, proving that the azide molecules were bound to the polymer brush surface firmly. Herein, the fluorescence intensity can be deemed as a measure of the amount of bound azide compounds. Washing removes the excess ink and unbound azides, leaving behind only potential a monolayer of bound azide compound on the sample surface. This is also reflected by a higher exposure time needed for the fluorescence imaging to reach the same intensity after washing (i.e. 55 ms before and 500 ms after washing), but the intensity remains almost the same for both. Still, the azide ink binds properly to the alkyne terminated polymer brush in  $\mu$ CS spotted spaces, and the micropattern is easy readout and assessed through a fluorescence microscope.

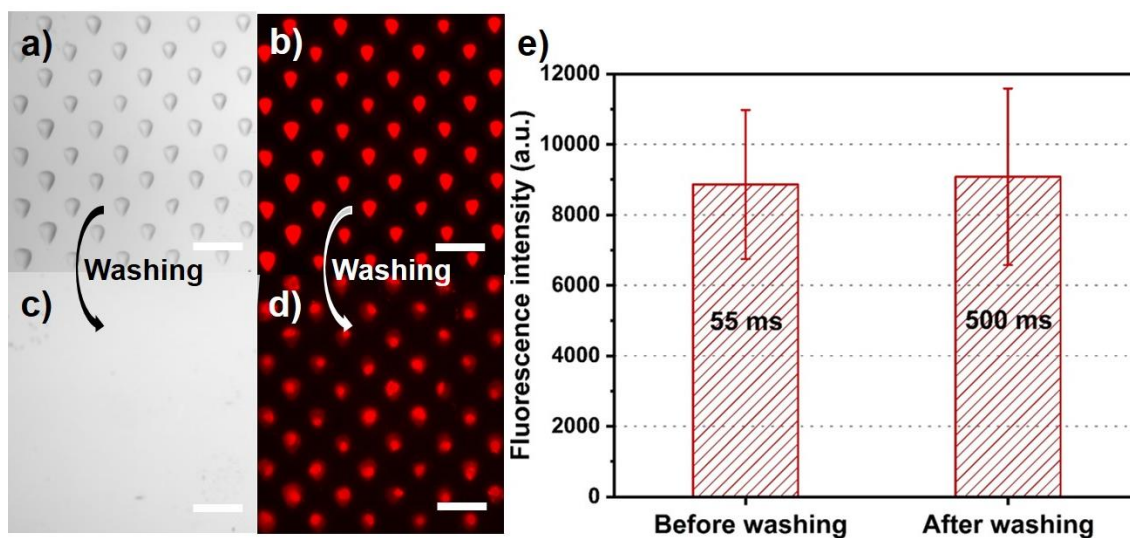


**Figure 4.6.**  $\mu$ CS printed Tamra-azide dots on polymer brush modified glass substrates. Pictures were captured in a) bright field and b) fluorescence (in Cy3 channel, exposure times 55 ms) before the washing step, and c) bright field and d) fluorescence (in Cy3 channel, exposure times 500 ms) after washing. e) Comparison of the fluorescence intensity before and after washing (data was collected on the image (b) and (d)). Taken into account the prolonged exposure time, around one tenth of fluorescent molecules available in the ink immobilized on the polymer brush. Scale bars are 50  $\mu$ m.

As described above, the azide compound binds properly to the alkyne-bearing polymer brushes. Judging from the needed exposure times to reach the same fluorescence intensity, about 10% of the molecules in an ink droplet get immobilized. Next, protein binding trials together with and without bovine serum albumin (BSA) blocking were implemented to assess the antifouling properties and targeting activity of the polymer brushes. To do so, biotin-azide ink was used to create micropatterns to polymer-brush-coated glass samples as described earlier. The high affinity of streptavidin toward biotin makes it a simple way to check the selective targeting and antifouling properties of the samples through selective protein binding. Therefore, streptavidin-Cy3 (SA-Cy3) was employed in combination either with or without FITC conjugated bovine serum albumin (BSA-FITC) blocking process in the trials. To keep procedures as similar as possible, the samples which were not blocked by BSA were incubated with phosphate buffered saline (PBS) as a control. The typical outcomes are shown in Figure 4.7. Firstly, as shown in Figure 4.7a and b, the polymer brush surface was blocked by BSA-FITC before implementing protein binding by SA-Cy3. In parallel, as shown in Figure 4.7c and d, another sample was directly incubated with SA-Cy3, without BSA blocking step. The SA-Cy3 was used for quantification of the bound protein and better visualization of antifouling properties, as the fluorescence intensity can be assumed as linear to the amount of the bound molecules. As shown in Figure 4.7e, the fluorescence intensity (in Cy3 channel) on SA-Cy3 coupled arrays, either with or without BSA blocking, is almost the same and also shows a considerably low intensity of background (in Cy3 channel), which means that the target protein even without prior blocking only binds to the biotinylated region and almost no protein fouling takes place at the unfunctionalized area. In addition, to visualize BSA adhesion, the background signals (in FITC channel) reflecting adhered BSA and unspecific fluorescence of polymer itself on the samples either blocked or unblocked by BSA-FITC were quantified as shown in Figure 4.8. As can be seen, the FITC background signals are both fairly low. With only slightly increased intensity on the blocked sample (this raise reflecting the small amount of BSA that can attach to the polymer brush). Interestingly, the sites with biotin-azide functionalization bind even less BSA, letting them appear darker than the unfunctionalized surrounding polymer brush. This suppression of intensity is not seen on the non-blocked sample, indicating that it is not caused by an overall reduction in background fluorescence

from the polymer brush itself due to CuAAC. Together, these results further suggest the excellent antifouling properties and low background character of the polymer brush coatings.

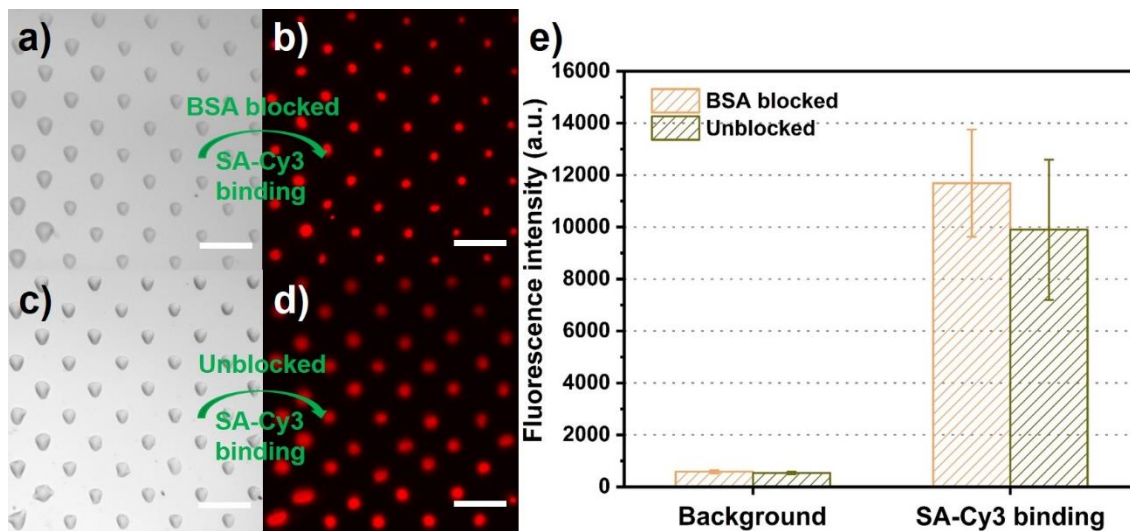


**Figure 4.7.** a) Biotin-azide printed dots and b) later incubated with SA-Cy3 after blocking with BSA-FITC. c) Biotin-azide printed dots and d) later incubated with SA-Cy3, but without any blocking step. e) Fluorescence intensity (in Cy3 channel) comparison between the samples blocked and unblocked with BSA-FITC. Exposure times for the fluorescent images are 100 ms. Scale bars are 50  $\mu\text{m}$ .

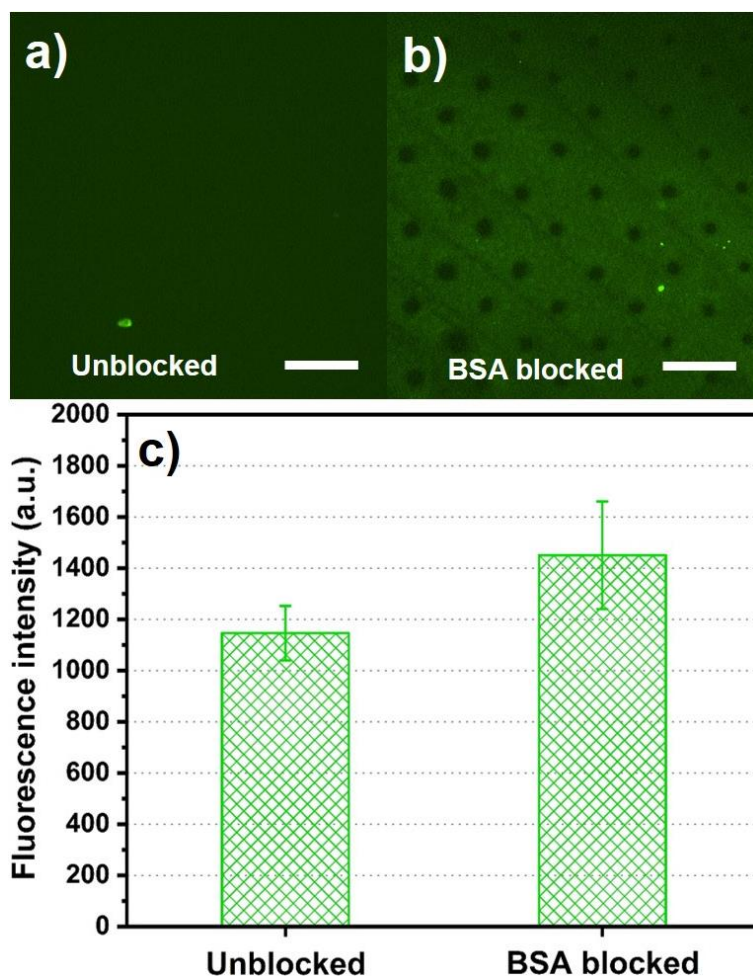


**Figure 4.8.** Samples (the same ones shown in Figure 4.7) were a) unblocked or b) blocked with BSA-FITC before incubation with SA-Cy3. c) Fluorescence intensity (in FITC channel) comparison between the unblocked and the blocked samples. Exposure times are 1 s for both pictures. Scale bars are 50  $\mu\text{m}$ .

Furthermore, to demonstrate the multiplexing compatibility and adaptability of the polymer brush coatings, azide inks either linked to a Cy5 fluorophore (Cy5-azide) or a biotin moiety (biotin-azide) were printed into alternating columns by  $\mu\text{CS}$ . Figure 4.9a shows the optical micrograph of the multiplexed pattern after printing ( $5 \times 5$  matrices of biotin-azide and Cy5-azide are shown on the top, and the pattern at the bottom part consists of the alternating columns of biotin- and Cy5-azide). After completion of the CuAAC reaction between azide and alkyne moieties, with the excess ink solution washed off, only the Cy5-azide functionalized columns are visible in fluorescence (Figure 4.9b). Thereafter, SA-Cy3 was incubated on the sample to visualize the biotin functionalized columns (Figure

4.9c). All in all, in this way, we demonstrated that it is feasible to do multiplexing functionalization without any negative interactions by  $\mu$ CS on poly(HPMA-*b*-AlkMA) polymer brush modified surface. Figure 4.5d shows the merged fluorescent image of Cy5-azide and SA-Cy3 bound biotin-azide arrays.

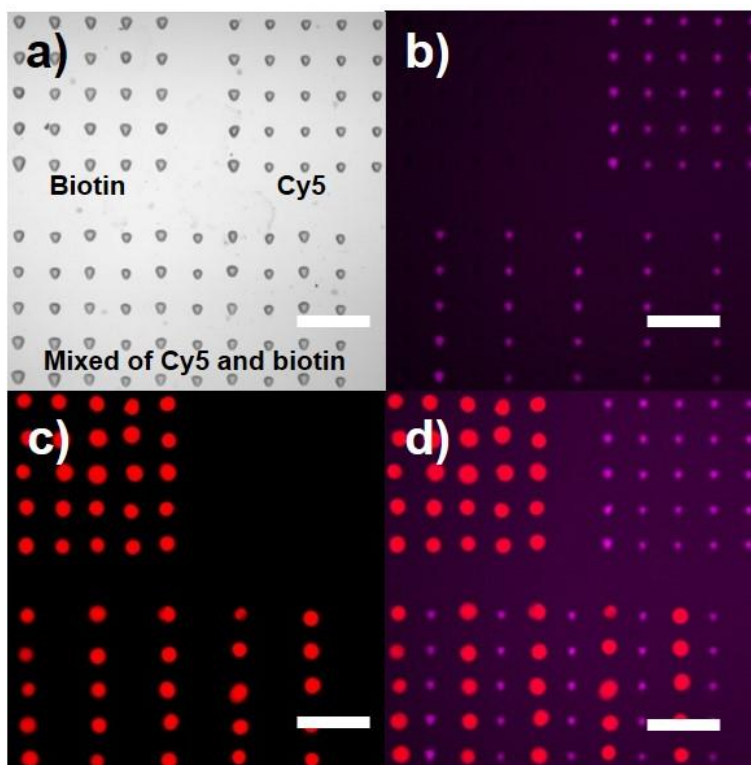


**Figure 4.9.** a) Optical image of  $5 \times 5$  matrices of biotin-azide (on the top left) and Cy5-azide (on the top right), and the pattern ( $10 \times 5$ ) at the bottom part consists of the alternating columns of biotin- and Cy5-azide. b) Cy5-azide arrays shown in Cy5 channel and with exposure time of 400 ms. c) Biotin-azide columns after binding with SA-Cy3 shown in Cy3 channel and with exposure time of 20 ms. d) Merged image by image (b) and (c). Scale bars are  $100 \mu\text{m}$ .

Based on our knowledge, the preparation conditions and the composition of the polymer brush have considerable influence on its antifouling properties and chemical reactivity.<sup>[137]</sup> In principle, the polymerization duration has a significant impact on coating thickness, and prolonged duration usually induces a thicker film coating. Therefore, to elucidate the coating thickness of polymer brush on its antifouling properties and reactivity, polymer brush coated glass samples with two different thicknesses were prepared, polymerized for

one day (“thinner”), and polymerized for four days (“thicker”). After sample preparation, these samples were investigated with protein binding assays as described earlier and then evaluated on a fluorescence microscope. The corresponding fluorescence intensity (in Cy3 channel) collected on different samples is shown in Figure 4.10a. The fluorescence intensity reveals that both types of samples give a similar low background value and thus a high signal-to-noise ratio, thus demonstrating excellent antifouling properties and chemical reactivity with azides. Moreover, the BSA blocking step again has no significant effects on antifouling properties as the same background and target signal values are shown. While error bars still overlap, the intensity of SA-Cy3 on the thicker sample is slightly lower than on the thinner sample. As the incubation protocols more kept same, this could mean that the thinner sample possesses a higher chemical efficient, since the intensity can be deemed as the number of reactive alkyne sites on the polymer brush that more translated into protein binding sites.

Furthermore, as the silanized methacrylate monolayer is crucial in the polymer brush grafting procedure, we studied the effects of ageing of the silane layer on the antifouling properties and reactivity of the polymer brush. For this purpose, polymer brushes were “grafted from” silanized monolayers at two different ageing states, aged for four months (“aged”) and freshly prepared (“fresh”). After that, a similar protein binding assay as described above was conducted on the brushes prepared on aged and fresh samples to evaluate the sample characters by fluorescence imaging. The related results are shown in Figure 4.10b. Both of the samples after protein binding show almost the same intensity of background and bound protein. Consequently, the ageing state of the underlying silane layer has an insignificant influence on the antifouling properties and reactivity of the polymer brush.

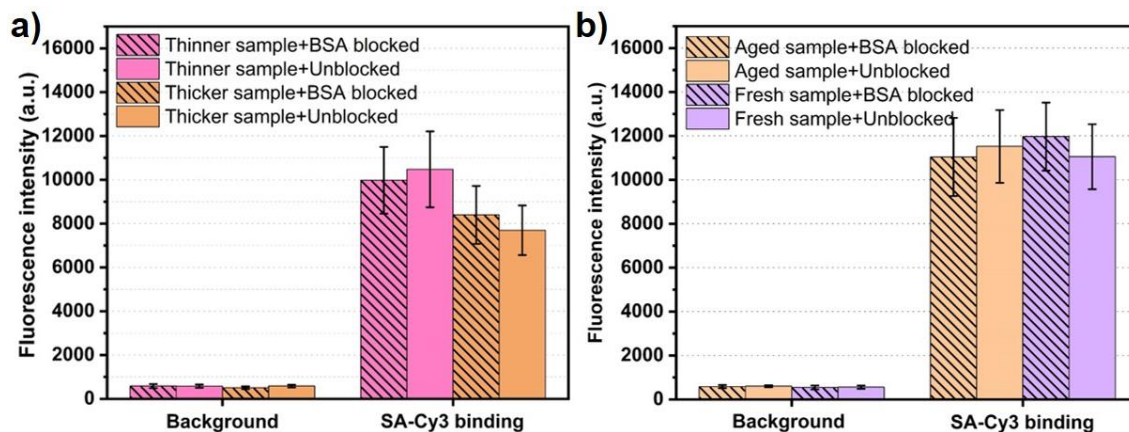


**Figure 4.10.** Fluorescence intensity (in Cy3 channel) of the samples incubated with SA-Cy3 with or without BSA blocking. Samples with a) different thicknesses and b) prepared at different ageing states of the underlying silane layer. The standard deviation was computed from 50 random spaces on unfunctionalized area for background, and 50 SA-Cy3 bound spots for target protein binding.

#### 4.2.3. Applying the polymer brush coatings to diamond surface

As demonstrated above, the poly(HPMA-*b*-AlkMA) polymer brush coating shows excellent antifouling properties and efficient reactivity in click chemistry, allowing omit to the additional passivation treatments and performing great in post-processes. These advantages facilitate the readout in array-based sensing techniques, simplifying the experimental procedures and saving analysis time. As a final step, the polymer brush coating prepared at the optimal fabrication parameters was implemented to the diamond surface to endow it with protein repellency and clickable reactive sites with the aim of suppressing unspecific background and raising the signal-to-noise ratio in array-based fluorescence imaging trials. Initially, a fluorescently labelled azide ink (Alexa488-azide) was patterned to the polymer-brush-coated diamond surface. As we can see from Figure 4.11a, b and c, the azide species bind stable to the surface, with the expected decrease in fluorescence intensity after washing off the excess ink. Overall, the polymer brush coating was successfully transferred to the diamond surface. Following, protein binding trials were conducted on biotin-azide functionalized microarrays, similar to the experiments done on glass samples. Importantly, the diamond-based samples were subjected either to BSA blocking or not before conducting protein binding, the results are

shown in Figure 4.11d, e and f. The comparison of the fluorescence intensity (Figure 4.11f) shows that highly selective protein binding was achieved on the micropatterned polymer-brush-coated diamond surface, with a high signal-to-noise ratio and low unspecific protein binding. This is in particular striking when comparing the fluorescence background on the polymer brush functionalized diamond with an unmodified control (Figure 4.12). Interestingly, on the diamond surfaces BSA blocking even slightly increases the background intensity (through error bars still overlap). All in all, the applied methacrylate-based alkyne-bearing antifouling polymer brush shows favorable effects on improving the signal-to-noise ratio for the diamond surface, thus highlighting and promoting the prospects of the diamond in biosensing related applications.

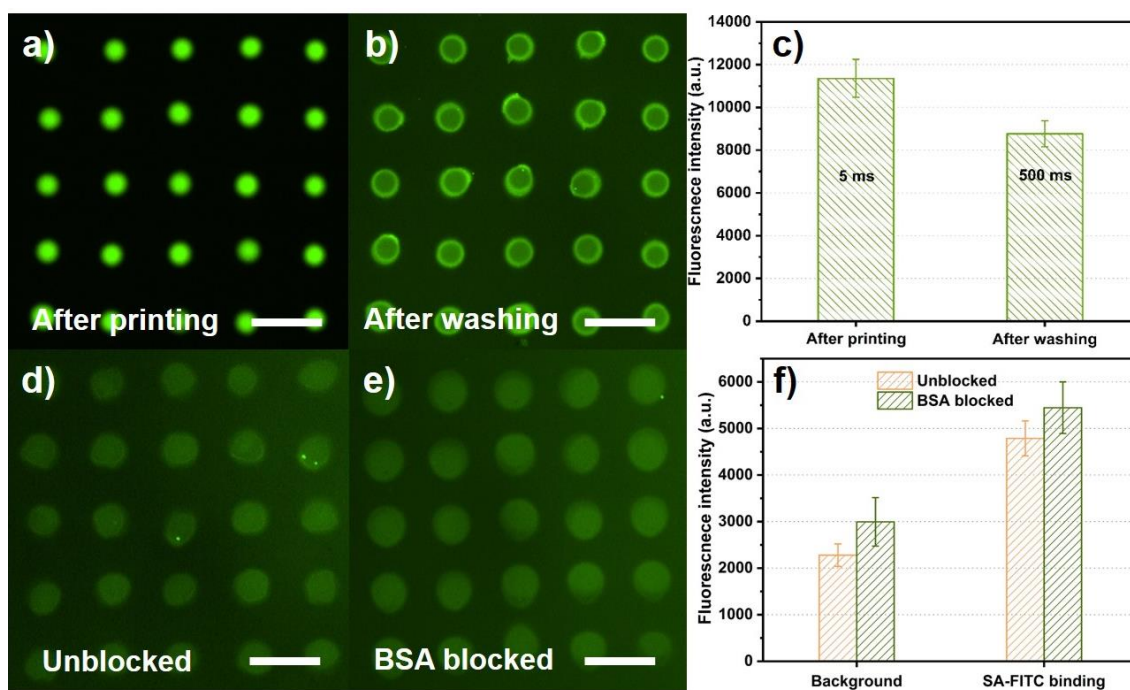


**Figure 4.11.** Fluorescent images of Alexa488-azide (green) micropatterns on a polymer-brush-coated diamond surface, a) after  $\mu$ CS printing (exposure time 5 ms), b) after washing (exposure time 500 ms), c) fluorescence intensity collected from image (a) and (b). Taking into account the prolonged exposure time after washing away the excess ink, around 1% of molecules available in the ink are immobilized to the diamond surface. Fluorescent images of SA (FITC conjugate, green) incubated biotin-azide micropatterns on polymer-brush-coated diamond surfaces, d) direct incubation of SA, and e) BSA (non-fluorescent) blocked prior to SA incubation (exposure time 1 s for both), f) fluorescence intensity of

background and spotted area collected from image (d) and (e). Interestingly, on the diamond surfaces BSA blocking even slightly increases the background intensity (through error bars still overlap). Scale bars are 50  $\mu\text{m}$  in all images.

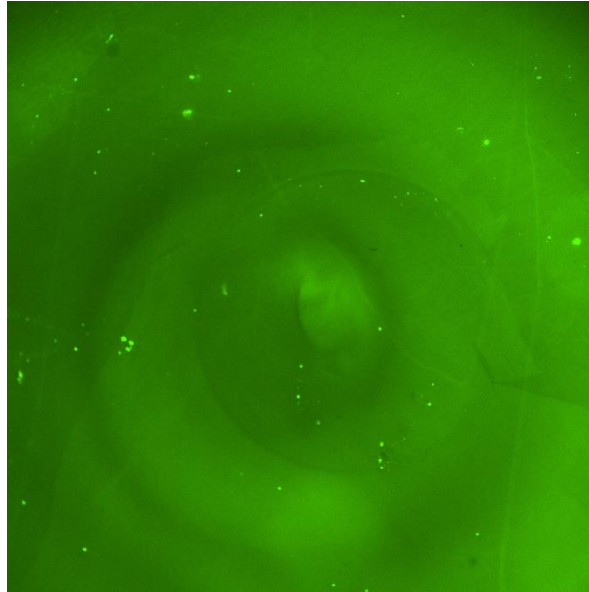


**Figure 4.12.** Fluorescent image (FITC channel of a naked diamond surface (no brush) after incubation with SA-FITC showing a high unspecific adsorption of protein. The fluorescence intensity is  $(6255.96 \pm 561.45)$  a.u. at an exposure time of 1s.

### 4.3. Summary

In summary, a biocompatible methacrylate-based alkyne-bearing antifouling polymer brush was designed and presented in this chapter, its remarkable protein-repellent ability and clickable reactivity were demonstrated via selective target protein binding in fluorescence imaging, and further successfully applied to diamond surfaces. The polymer brush coating is compatible with the site-specific functionalization via CuAAC click chemistry by  $\mu$ CS to enable covalently bound, arbitrarily designed or even multiplexed micropatterns. This facilitates the introduction of selective protein binding sites on an otherwise highly protein-repellent polymer brush surface on the diamond. Importantly, the applied polymer brush coating on the diamond surface retained its reactivity for click chemistry and showed an enhanced signal-to-noise ratio, promoting the applications of diamond in fluorescence imaging. At last, we expect this clickable antifouling coating could be beneficially implemented to diamond-related bioimaging probes or targeted systems and promote the development of fluorescence imaging in sensing.

## **Chapter 5 – Fabrication of different sensing platforms for DNA hybridization**

### **5.1. Introduction**

The development of DNA biosensors has gained substantial attention over the last decades because it has tremendous potential in the application of disease diagnosis and forensics,<sup>[218-221]</sup> in particular also for the diagnostic of viral diseases.<sup>[8, 222]</sup> In general, nucleic acid sensing strategies are based on the DNA hybridization between single-stranded DNA (ssDNA) probe and complementary target strand.<sup>[223, 224]</sup> First, ssDNA probes with a complementary sequence to the target are immobilized on the sensor interface or surface, then, the targeted complementary ssDNA can hybridize with the probe and bind the target for detection.<sup>[223]</sup> Different technologies have been developed for tethering DNA probes to substrates.<sup>[225-227]</sup> Among them, the patterning into microarrays has become one of the most popular and efficient fabrication approaches for sensing platforms since it evolved in the 1990s.<sup>[228]</sup> Normally, spot uniformity, density of immobilized DNA probes, and repeatability are known as primary factors for detecting probe microarray sensitivity and reliability, and these factors are strongly influenced by the physical and chemical properties of the sensor platform interface.<sup>[229-231]</sup> Furthermore, steric issues between the DNA probe and the interface, as well as steric hindrance between adjacent probes and electrostatic forces, all affect the hybridization efficiency and capacity in surface hybridization.<sup>[232]</sup> As a result, researchers have focused their attention on the morphology properties and structural architectures of the platforms in order to better understand the effects of interactions between the immobilized DNA probe assembly and the surface conformations on hybridization behaviors.

To achieve robust microarrays, a stable binding of the DNA probe to the substrate is key.<sup>[224]</sup> Here, in particular, thiolates have been used as a reactive bridge for the covalent binding of DNA oligomers to gold films because of their ease of use, chemical availability, and ability to produce thin and uniform films. A covalent Au-S bond forms by spontaneous reactions of thiolated oligonucleotides and gold surfaces, thus immobilizing the DNA

probe on the surface.<sup>[233, 234]</sup> Studies have shown that the gold-sulfur bond is less stable than bonds between sulfur and silver or copper, and this limits development and largescale manufacturing to some extent.<sup>[235]</sup> However, silver and copper are seldom used for *in-vivo* analysis due to their strong toxicity to living systems and their ability to easily oxidize, which readily attracts carbon-based contaminants from the ambient environment leading to difficulties in forming densely packed molecular layers.<sup>[224]</sup> Therefore, the gold-based system become a more desirable candidate for attaching thiol-conjugated derivatives as a result of its good biocompatibility and favorable qualities in optics and electronics.<sup>[224, 235]</sup>

Gold-based systems are in particular suited for measuring and monitoring DNA hybridization via surface plasma resonance.<sup>[236]</sup> Microarrays, on the other hand, are mostly read-out via fluorescence imaging.<sup>[237, 238]</sup> Here, gold-based platforms are unfavorable, as they can quench fluorescence when fluorophores get near to the surface.<sup>[239]</sup> However, there are also alternatives to gold-based interfaces, also able to accommodate thiolated DNA probes. Click reactions have become a popular procedure for conjugation of biomolecules, because of their high yields, mild reaction conditions, and compatibility with a wide range of reactive moieties. Different functional interfaces allowing specific click chemistry reactions, e.g. alkyne-based,<sup>[240, 241]</sup> alkene-based,<sup>[242, 243]</sup> epoxy-based surfaces are available.<sup>[244, 245]</sup> Additionally, the hybridization behavior of the surface-immobilized ssDNA probes highly depends on the probe packing density, probe conformation, and the interface structure and configuration.<sup>[246, 247]</sup> Several studies have proposed numerous schemes for immobilizing DNA probes in upright conformations on the interfaces, i.e. surfaces with functional monolayer,<sup>[248, 249]</sup> bilayer coatings,<sup>[250, 251]</sup> polymer-modified interfaces,<sup>[252, 253]</sup> and adsorption of DNA probes via a thiol incorporated at one end.<sup>[232]</sup> Brush-like interfaces or brush-like probes can also strengthen hybridization efficiency because of the lower steric hindrance as compared to the directly adsorbed probes on metal interfaces (Au, Ag or Cu).<sup>[232]</sup> To the best of our knowledge, no direct comparison of the differences in DNA hybridization behavior on various platforms with different surface topographies and compositions, such as self-assembled monolayers (SAMs), metal-based films, and polymer-based coatings, have been undertaken yet.

Therefore, in this work, three different platforms (DBCO- and PBAG-modified surfaces and plain gold surfaces) were compared to study the influence of surface chemistry, topography and conformation on DNA hybridization. The DBCO-modified surface is a SAM surface with cyclooctyne species that through thiol/yne reaction, can click to thiolated molecules. The PBAG-modified surface is a grafted bilayer polymer system with epoxide terminals (prepared via “grafting to” method) that can bind to SH-DNA via thiol/epoxide reaction. The gold-coated surface is prepared by physical vapor deposition and can react to thiolated-oligonucleotides via Au-S bonds. To evaluate the hybridization behavior and efficiency on these platforms, ssDNA probe (22 or 44mer) microarrays were patterned by microchannel cantilever spotting ( $\mu$ CS), followed by hybridization with a complementary oligonucleotide conjugated either with a fluorescent dye or a biotin moiety. Later, by utilizing DNA-directed immobilization (DDI), protein binding tests were performed to quantitatively determine the hybridization efficiency on different platforms by measuring fluorescence intensity (Figure 5.1).

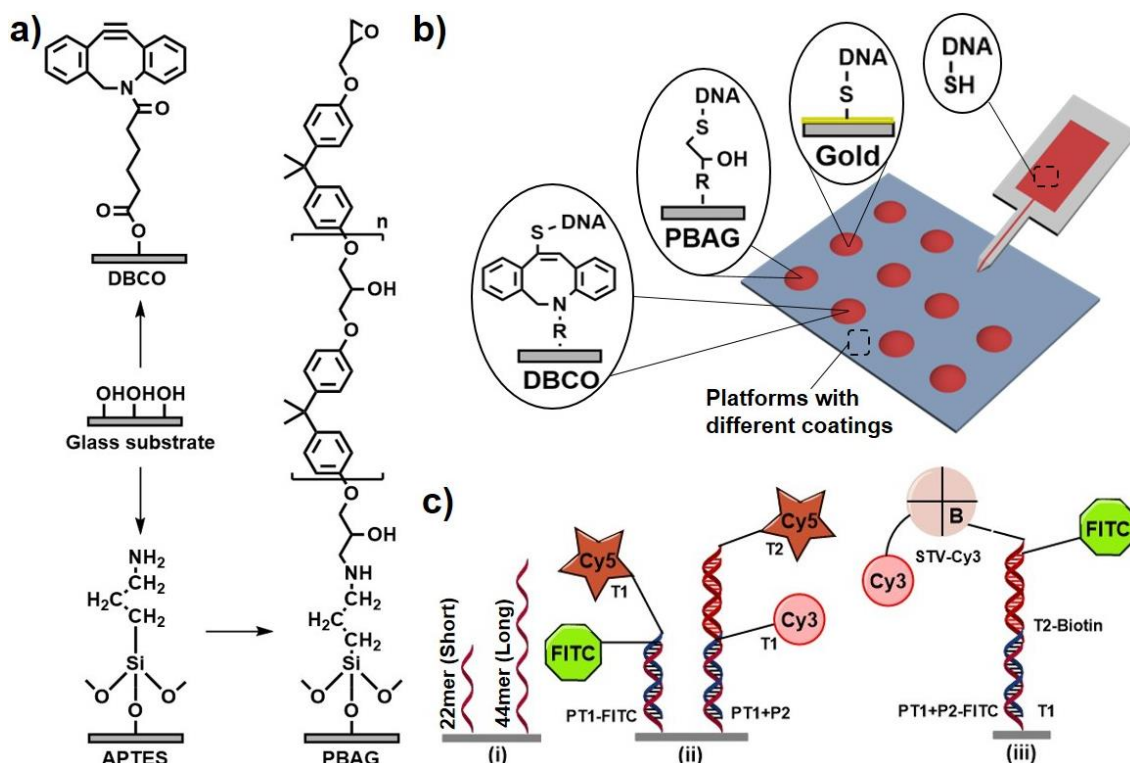


**Figure 5.1.** a) Schematic diagram of the modification processes of DBCO- and PBAG-modified platforms, b) thiolated DNA probe microarrays patterned by  $\mu$ CS on modified platforms, c) hybridization and protein binding on DNA arrays.

## 5.2. Results and discussions

### 5.2.1. Characterization of sensing platforms

Prior to spotting the DNA probe microarrays on the different platforms, the surface wettability, morphology, architecture, and composition were investigated by static water contact angle (WCA), atomic force microscopy (AFM), ellipsometry, and X-ray photoelectron spectroscopy (XPS) to characterize the basic surface parameters and morphology (Table 5.1).

**Table 5.1.** Static WCA, roughness, and ellipsometric thickness values of different platforms (mean  $\pm$  standard deviation).

Items	WCA [°]	Roughness [ $R_a$ , nm]	Thickness [nm]*
Bare glass	46.2 $\pm$ 1.5	0.135 $\pm$ 0.086	--
Amino-modified (-NH <sub>2</sub> )	44.1 $\pm$ 0.9	0.205 $\pm$ 0.109	1.4 $\pm$ 0.1
Gold-film	53.4 $\pm$ 1.4	0.519 $\pm$ 0.172	100**
DBCO-modified	63.0 $\pm$ 1.3	0.212 $\pm$ 0.107	1.5 $\pm$ 0.2
PBAG-modified	33.2 $\pm$ 1.3	0.386 $\pm$ 0.143	27.6 $\pm$ 2.7

\*Ellipsometric thickness was measured on silicon samples prepared in parallel with glass samples. \*\*Nominal thickness as of the evaporation process.

In general, WCA testing is a facile method to identify whether the expected molecules are modified on the substrate or not, because different molecules lead to different surface tension and show different WCA values.<sup>[254]</sup> Thus, static WCA measurements were performed on hydroxylated, DBCO-terminated, and PBAG-modified surfaces for up to three months post-modification. Due to the extremely stable and barely change in surface tension of the gold-modified silicon substrate, the WCA was not monitored for a longer time period.

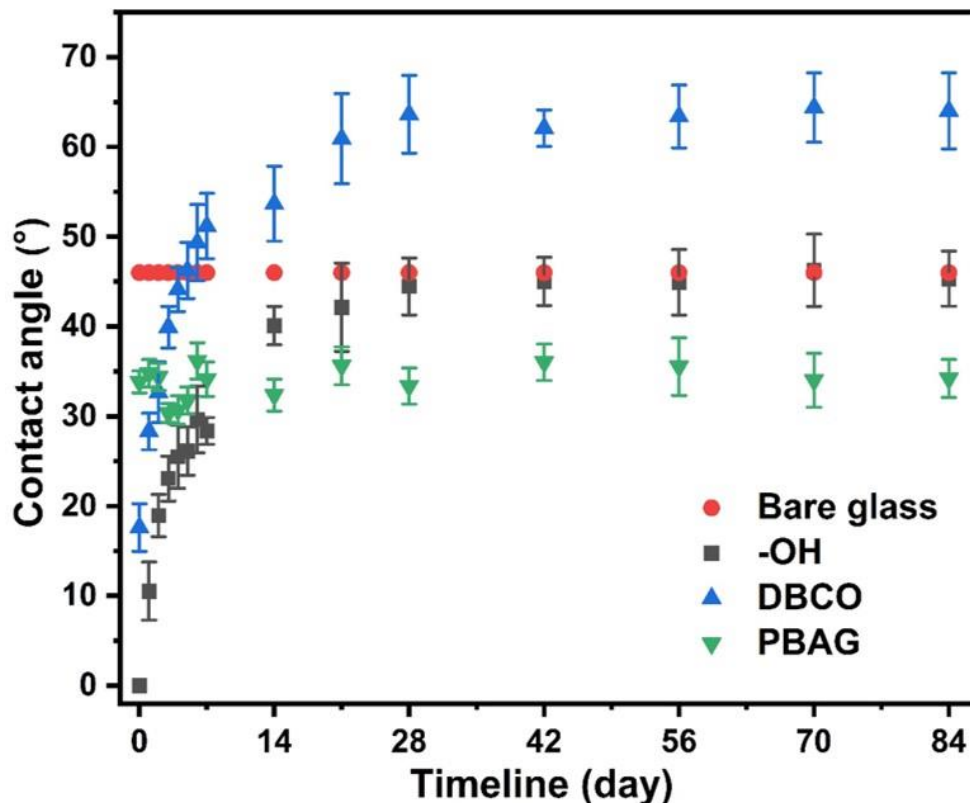


**Figure 5.2.** Recording of static WCA on bare glass, hydroxyl (-OH), DBCO and PBAG platforms for three months after the modification.

Initially, the plasma-activated, thus hydroxylated glass sample shows a near-zero WCA. However, after exposure to air conditions, the WCA of the hydroxylated sample increases and approaches the bare glass value (approx.  $46^\circ$ ) again after 28 days. The DBCO-terminated glasses exhibit less hydrophilicity, with an initial WCA at around  $18^\circ$ , stabilizing at approximately  $63^\circ$  after four weeks. The change of WCA on DBCO-modified and hydroxylated surfaces can likely be ascribed to the gradual decay of residual hydroxyl groups after the initial functionalization.<sup>[240]</sup> The WCA of freshly prepared amino-terminated surfaces (as the basis step for PBAG modification) shows a value at around  $31^\circ$ , raising to  $44^\circ$  after about four weeks (curve not shown). After “grafting to” the PBAG layer onto the  $\text{NH}_2$ -silanized surfaces, the WCA maintains at around  $33^\circ$  over the monitored period. This indicates a good stability of the film and the brush structures overlaying the whole surface (thus, residual groups on the surface are covered from the start).

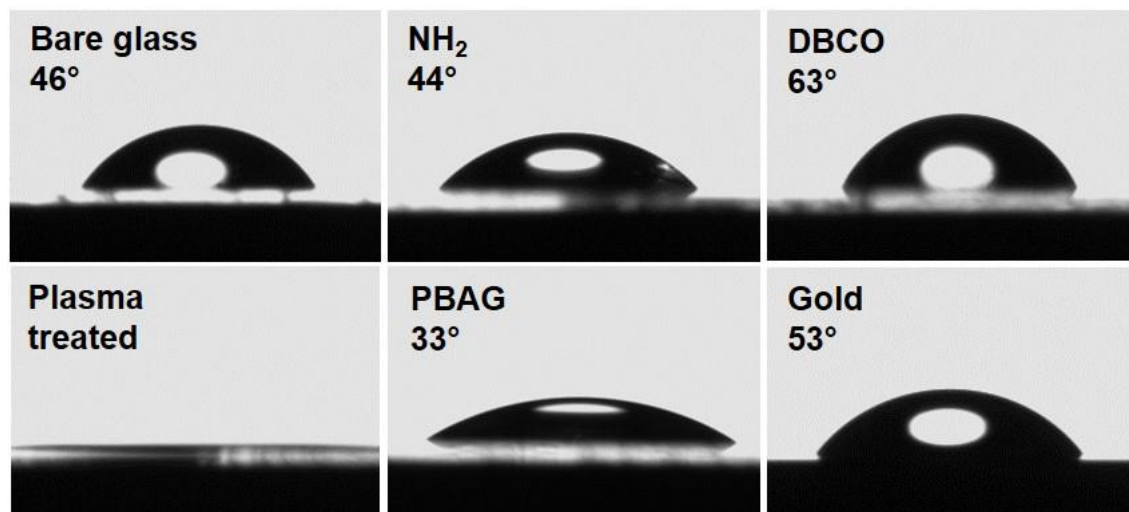


**Figure 5.3.** Digital photos of the static WCA on the bare glass,  $\text{NH}_2$ -, DBCO-, Plasma-treated glass (hydroxyl -OH), PBAG- and gold-modified substrates.

Surface modification induces not only a change in WCA but also a change in surface roughness, which is an important factor for the ink spreading during the  $\mu\text{CS}$  process. Furthermore, on the rough surfaces, the ink transfer from the SPT is not uniform, which can lead to non-uniform arrays during  $\mu\text{CS}$  process.<sup>[255]</sup> Therefore, surface roughness (root-mean-square roughness (Ra)) was evaluated via AFM and film thicknesses were measured via ellipsometry for the different modifications (Figure 5.4, Table 5.1). The bare glass possesses a very smooth interface with a roughness of  $(0.135 \pm 0.086)$  nm. After coating with different materials, roughness rises. As shown in Figure 5.4 and Table 5.1, the DBCO-terminated and  $\text{NH}_2$ -terminated surfaces exhibit roughnesses of  $(0.212 \pm 0.107)$  nm, and  $(0.205 \pm 0.099)$  nm, respectively. This is consistent with the roughness of SAMs, implying that the DBCO and amino group layers are successfully immobilized on the surface.<sup>[256]</sup> The ellipsometric thickness of DBCO-treated and  $\text{NH}_2$ -treated samples are  $(1.5 \pm 0.2)$  nm, and  $(1.4 \pm 0.1)$  nm, respectively, again consistent with a successful SAM formation. After “grafting to” the PBAG layer onto the  $\text{NH}_2$ -treated surfaces, the roughness increased further to  $(0.386 \pm 0.143)$  nm, and the ellipsometric thickness reached  $(27.6 \pm 2.7)$  nm. The gold-coated surface (prepared with 100 nm thickness of Au layer) displays a slightly higher value of roughness of  $(0.519 \pm 0.172)$  nm compared with the other surfaces.

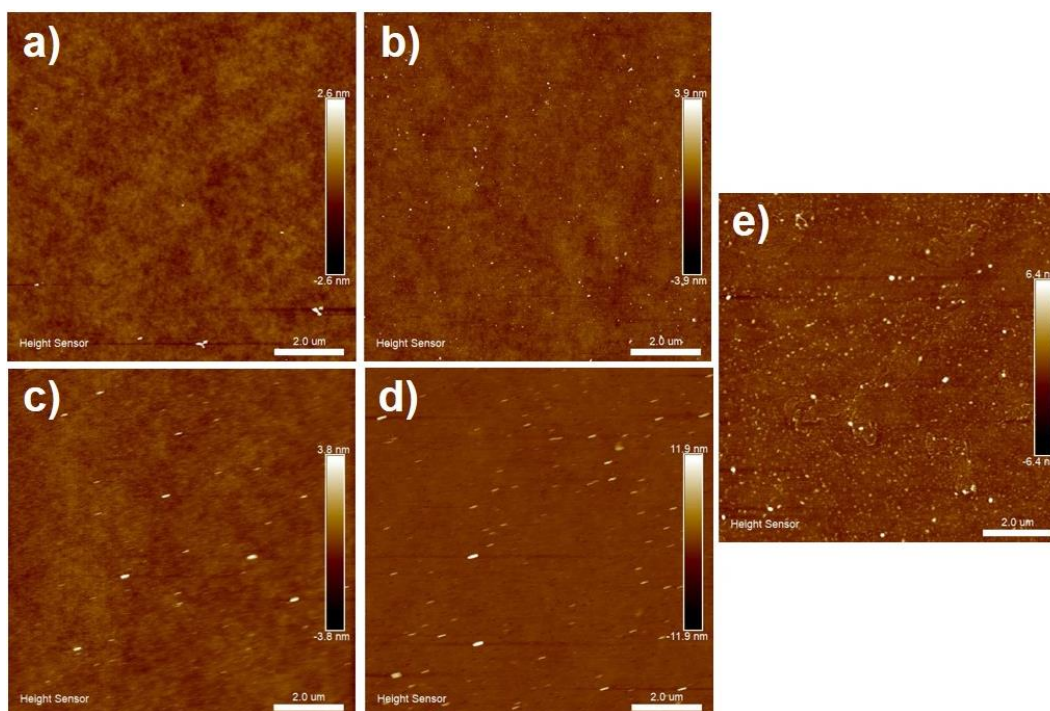


**Figure 5.4.** AFM images of modified surfaces for roughness measurement. a) Bare glass,  $0.135 \pm 0.086$  nm; b) DBCO-modified surface,  $0.212 \pm 0.107$  nm; c)  $\text{NH}_2$ -modified surface,  $0.205 \pm 0.109$  nm; d) PBAG-modified surface,  $0.386 \pm 0.143$  nm; e) gold-coated plain surface,  $0.519 \pm 0.172$  nm. All scale bars are equal to  $2 \mu\text{m}$ .

To confirm also the chemical modifications, XPS was performed on the samples, and the spectra are shown in Figure 5.5. As can be seen in Figure 5.5a and 5.5b, the nitrogen composition of the bare glass is about 0.67 at%, while after functionalization with  $-\text{NH}_2$  and DBCO species, the nitrogen compositions increase to 3.06 at% and 0.88 at%, respectively, confirming that the amino and DBCO compounds attached to the surface.<sup>[240]</sup> However, the nitrogen composition declined to 1.39 at%, when the second layer (PBAG) was grafted to the aminated surface. This can be understood as there are no nitrogen atoms existing in the scaffold of the grafted PBAG, thus changing the elemental composition of the surface. The high-resolution XP spectra in the N 1s region (Figure 5.5b) of  $-\text{NH}_2$ , PBAG- and DBCO-functionalized surfaces all show two distinct peaks. The first one, located at 400.0 eV, is attributed to the amino and the amide groups, the second (402.2 eV) can be attributed to the secondary amine groups.<sup>[257]</sup> Furthermore, the XP spectra of the C 1s region in Figure 5.5c shows that only the spectrum of the PBAG-modified sample shows

an additional peak at 287.0 eV, which probably stems from the epoxy groups on the PBAG backbone.<sup>[258]</sup> As a further indication of PBAG attachment, the ratio of (C-C, C-H):(C-O) is raised from 2.76 to 3.51 after grafting of the PBAG layer. For the gold surface, the core level spectra of the Au 4f region show two strong peaks observed at 84.0 eV and 87.7 eV, respectively, which can be attributed to the metallic Au<sup>0</sup>.<sup>[259]</sup> All in all, the XP spectra confirm that the expected compounds are presented on the surfaces, and surface modification was successfully implemented.

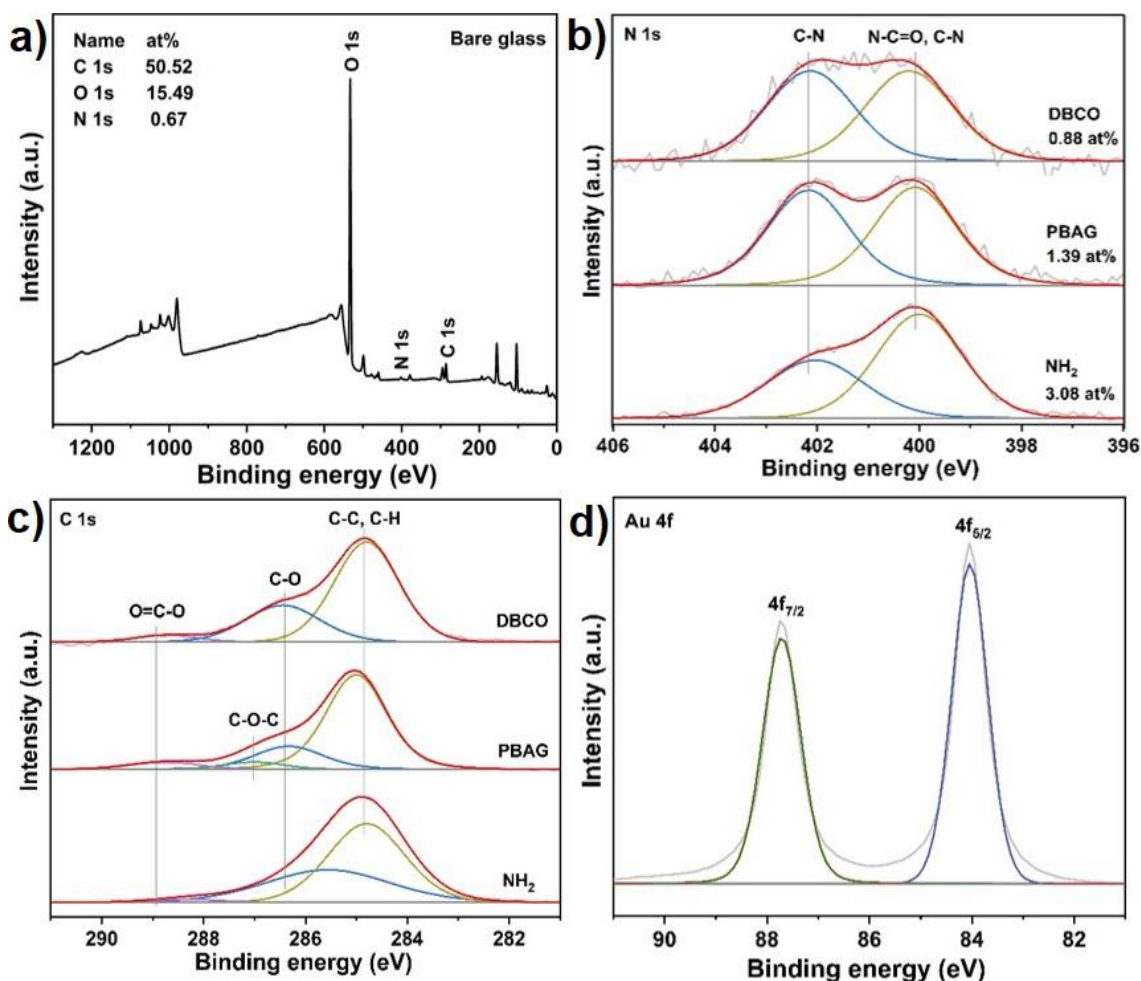


**Figure 5.5.** XP spectra of different modified surface. a) XP wide spectrum of bare glass surface, b) high-resolution XP spectra at N 1s region of aminated-(bottom), PBAG-modified (middle), and DBCO-modified (top) surfaces, c) high-resolution XP spectra at C 1s region of aminated-(bottom), PBAG-modified (middle), and DBCO-modified (top) chips, d) high-resolution XP spectra at Au 4f region of gold-coated surface.

### 5.2.2. DNA hybridization on different platforms

In order to generate microarrays for DNA hybridization, thiol-conjugated DNA probe sequences were spotted on the different platforms via  $\mu$ CS. To ensure complete reactions (thiol/epoxy, thiol/alkyne, and thiol/gold) and to obtain the saturated density of the immobilized probes, the spotted samples were allowed to rest at room temperature overnight before washing off the excess ink solution. Prior to hybridization, samples were blocked by bovine serum albumin (BSA) to prevent unspecific adhesion of DNA to the surfaces. Probes of two different lengths were employed, 22mer sequences (“short”), and 44mer sequences (“long”). The DDI protein binding tests were conducted on oligomer arrays containing long probe segments (44mer), which were hybridized with two short target sequences (both 22mer). After hybridization, samples were assessed by fluorescence microscopy.

As a first test of successful probe immobilization and hybridization on the different platforms, short probe segments (PT2, 22mer) were spotted into microarrays, followed by hybridized with fluorescently labelled ssDNA targets (T2-Cy3, 22mer), results are summarized in Figure 5.6. Obviously, hybridization occurred on all platforms, as evident by the microarray becoming visible in fluorescence. On the PBAG-coated sample (Figure 5.6a), the microarray spot features stand clearly out over the background after hybridization. On the DBCO-terminated surface (Figure 5.6b), the hybridized pattern is also visible, though the signal intensity is weaker. An interesting phenomenon was found on the gold-coated samples, as after hybridization, the arrays were barely seen in fluorescence when imaged in air (Figure 5.6c), only in solution patterns were clearly visible (Figure 5.6d). This can be understood considering that the fluorophores in the DNA targets are being quenched by the gold surface in the air conditions due to the DNA sequences lying down to the surface, bringing the fluorophore even nearer to the gold film. This increases the energy or electron transfer between the fluorophore and the surface, thus leading to non-radiative relaxation of the excited state.<sup>[239]</sup> Under liquid, the DNA sequences are in a more upright conformation, and the enlarged distance between the gold interface and the fluorophore weakens the quenching effect by the gold, making the patterns observable in fluorescence. On these ground, the fluorophore-surface interactions

on the gold-coated chips cause challenges for surface fluorescence analysis.<sup>[232]</sup> The feature size distribution (denoted by feature diameter) of different platforms is shown in Figure 4.6e. In addition, the effects of the pH value of the phosphate buffered saline (PBS) solution used as liquid on the fluorescent signal on the gold surface were also studied, but no significant impact was found (Figure 5.7). Consequently, the nearly neutral PBS buffer was used for all further experiments. Figure 4f shows the summary of the relative fluorescence intensity of the hybridized samples on PBAG-coated ( $12317.43 \pm 1079.56$  a.u.), DBCO-coated ( $6926.22 \pm 1406.44$  a.u.), and gold-coated ( $2900.93 \pm 243.69$  a.u.) surfaces. Clearly, the PBAG surface exhibits the highest fluorescence intensity of the three platforms, followed by DBCO and gold. Additionally, the PBAG sample shows less background compared to the DBCO sample, which is favorable to the fluorescent signal readout. The difference in the platforms' performance will be caused by a combination of several effects. (I) The efficiency of probe binding and resulting probe density in the microarray spots, (II) influence of the surface itself in hybridization with the target DNA, e.g. over surface charge effects, and (III) interference with the fluorescent readout by quenching of the fluorophore. Here, increasing the roughness of a surface can raise the number of possible binding sites resulting in a higher probe density. While the gold surface is the roughest of the tested platforms, it suffers from the fluorophore quenching, thus lowering overall performance. The surfaces' influence on the hybridization itself is harder to assess. In order to exclude a direct influence of the (underlying) glass surface itself on probe immobilization and hybridization, a control experiment with probe PT1-FITC (22mer, green fluorescent) was done on bare glass. (Figure 5.8). After washing, no fluorescence was observed, thus the glass itself does not significantly bind DNA on itself. As the fluorescent signal on the gold-coated sample is by far the weakest one among the three hybridization strategies, probably due to the quenching effect of gold, limiting the application prospect in fluorescence read-out microarrays. It was not further considered in the next experiments.

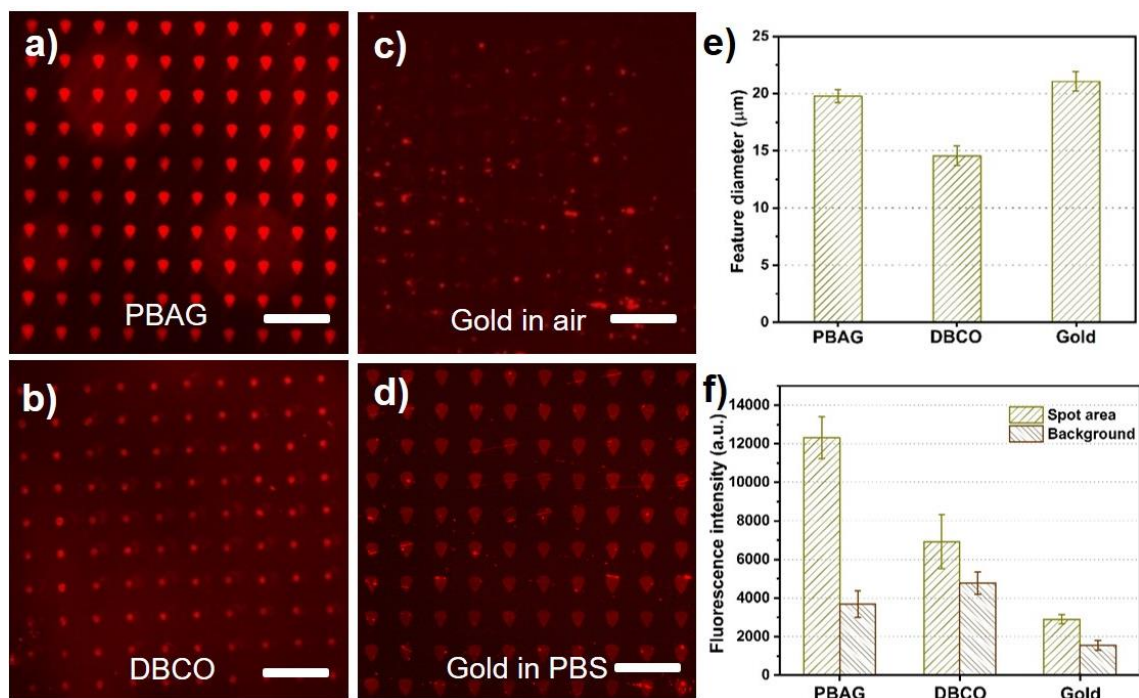


**Figure 5.6.** Hybridization of the target T2-Cy3 (red) with the probe PT2 dot arrays on different platforms, a) on PBAG surface, b) on DBCO surface, c) on gold surface (image captured in air), and d) on gold surface (image captured in PBS solution). e) Histogram of feature size (denoted by spot diameter) in DNA detection array on samples in image (a), (b) and (d). f) Summary of the relative fluorescence intensity (hybridized spots and background) collected on images (a), (b) and (d), respectively. The exposure times of the images are 1 s, and scale bars are equal to 100  $\mu\text{m}$ .

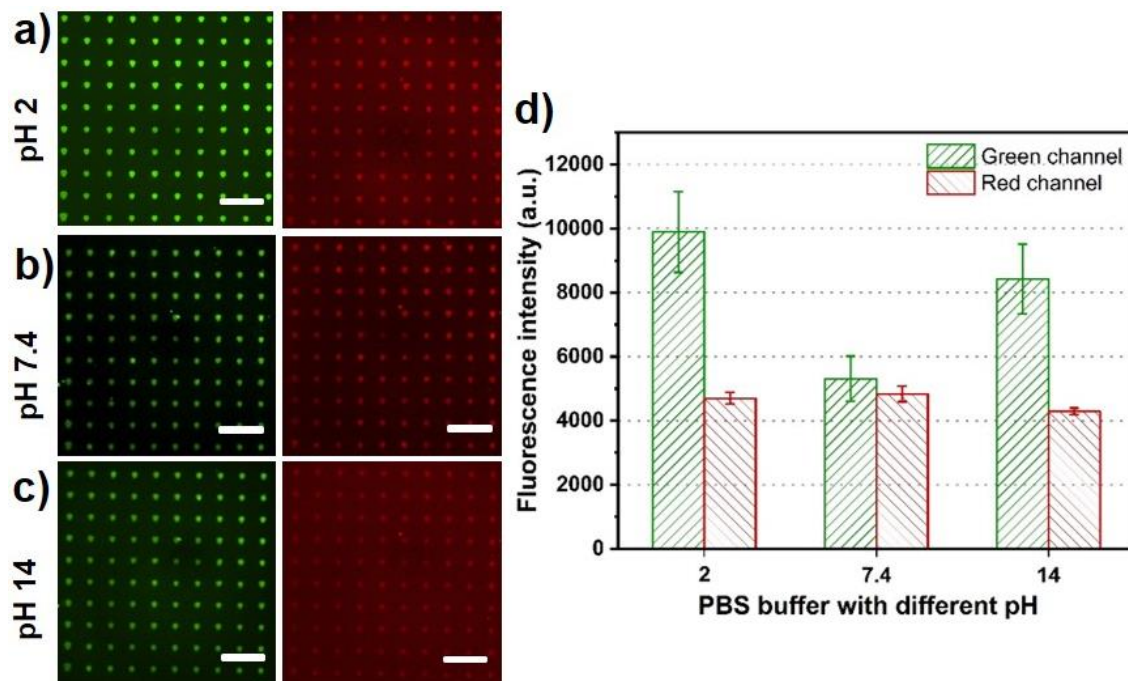


**Figure 5.7.** Fluorescent images of oligonucleotide arrays (PT2-FITC, green, left side) hybridized with fluorophore-tagged target oligomer T2-Cy3 (red, right side) on gold-coated chips covered with a drop of PBS solution at a) pH 2, b) pH 7.4, c) pH 14, respectively; d) fluorescence intensities collected at green and red channels on pictures (a), (b) and (c), respectively. The exposure times are 1 s, and scale bars are 100  $\mu\text{m}$ .

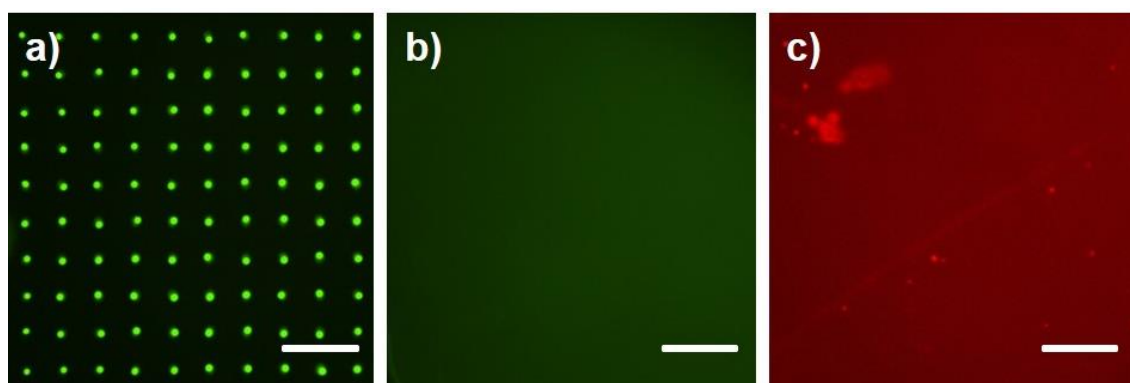


**Figure 5.8.** Control experiments on bare glass substrate. a) Freshly printed PT1-FITC (green) array, b) the same sample after washing with PBS, c) the sample after incubation with T1-Cy3. The exposure times of a) is 300 ms, and of b) and c) are 1 s. Scale bars are 100  $\mu\text{m}$ .

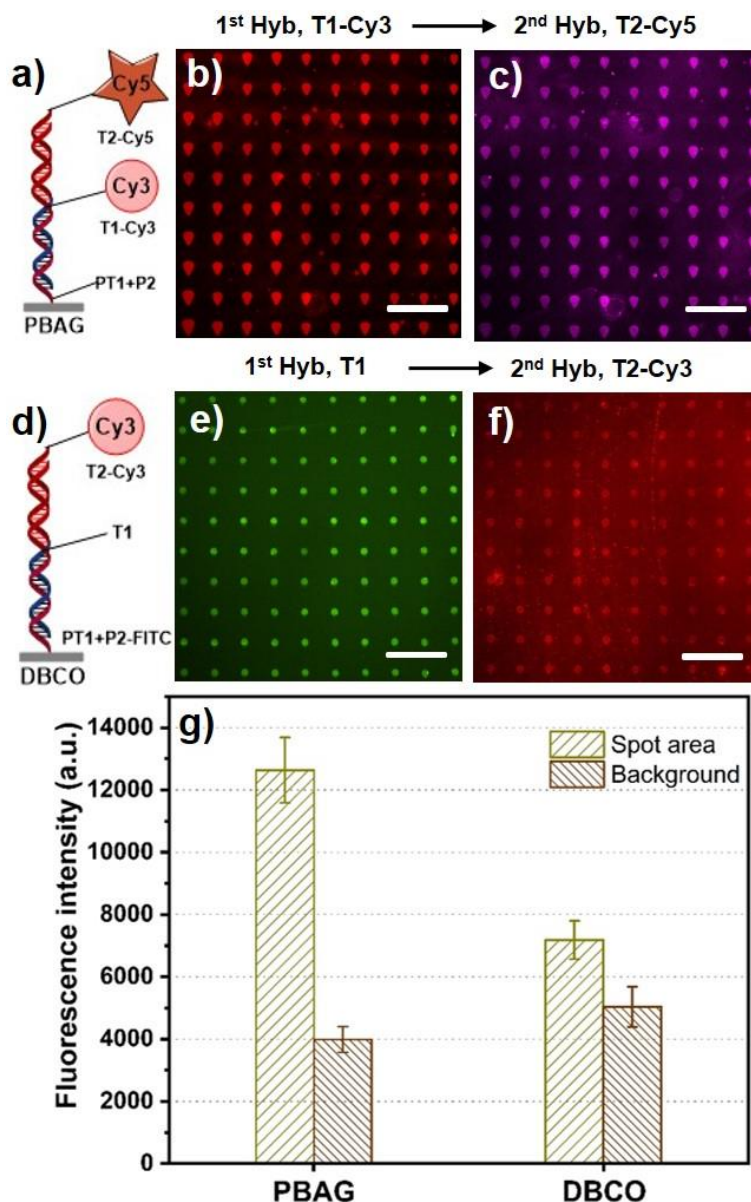


**Figure 5.9.** Hybridization (Hyb) of two ssDNA targets one after another probe arrays containing long DNA sequences. a) Schematic drawing of hybridization protocol for image (b) and (c). The ssDNA targets b) T1-Cy3 (red) and c) T2-Cy5 (magenta) were incubated on PBAG-modified substrate after immobilization of PT1+P2 on the surface. d) Schematic drawing of hybridization protocol for image (e) and (f). Hybridization of e) T1 and f) T2-Cy3 (red) with the PT1+P2-FITC (green) probe array on DBCO-modified surface. g) Summary of the relative fluorescence intensity (spot area and background) collected on images (b) and (f). The exposure times are 1 s, and scale bars are 100  $\mu$ m.

Next, two-step hybridizations were trialed. For this, two different short targets (both 22mer) were used to hybridize with a probe bearing a complementary long segment (44mer) on PBAG- and DBCO-modified surfaces one after another (Figure 5.9). For PBAG surfaces, microarrays of probes bearing long sequence (PT1+P2, 44mer) were spotted via  $\mu$ CS and then hybridized subsequently with the short targets T1-Cy3 (first, 22mer) and T2-Cy5 (second, 22mer). On first incubation, the microarray appears in Cy3-channel of the fluorescence (Figure 5.9b), and after second incubation, also in the Cy5-channel (Figure 5.9c). In a similar protocol but with differently labelled targets, a long sequence probe (PT1+P2-FITC, 44mer) was spotted into a microarray and then subsequently hybridized first with a non-fluorescent short target (T1, 22mer), and then with a fluorescently labelled second short target (T2-Cy3, 22mer). First, the microarray is stably visible in the FITC-channel fluorescence (Figure 4.9e), via the probe-conjugated fluorophore. On the second incubation, the microarray becomes visible also in the Cy3-channel (Figure 5.9f), proving the assembly of the second target. The quantized fluorescence intensity collected on PBAG- (figure 5.9b) and DBCO-modified (figure 5.9f) surfaces again confirms that the PBAG surface exhibits advantages in DNA hybridization and shows less background.

### 5.2.3. Protein binding assay on hybridized DNA patterns

In the last set of experiments, the PBAG and DBCO platforms were assessed for DDI-like protein immobilization. For this, both surfaces were prepared with microarrays spotted from the same fluorescently labelled probe with a long sequence (PT1+P2-FITC, 44mer), then hybridization with the short targets (T1 and T2-Biotin). In a final incubation step, the microarrays were incubated with a fluorescently labelled protein (streptavidin-Cy3, (SA-Cy3)) that can then self-assemble over the biotin-avidin interaction.<sup>[143, 148]</sup> Figure 5.10 shows the results of the protein binding assay on the DNA patterns. After patterning, on both platforms, the probe microarrays are clearly visible in FITC-channel (Figure 5.10a and b). After hybridization and protein incubation, the microarrays are also visible in the Cy3-channel, indicating successful immobilization of the protein (Figure 5.10c and d). The fluorescence intensity of the coupled streptavidin on the hybridized DNA arrays is  $(9673.33 \pm 879.38)$  a.u. on the PBAG surface, and  $(5621.22 \pm 606.44)$  a.u. on the DBCO

surface, respectively. On the whole, the DNA hybridization efficiency on PBAG-modified chips is around 40% higher than it on DBCO-modified chips according to the fluorescence intensity. A possible reason could be that the “grafting to” bilayer polymer, PBAG-treated surface, declines the activated sites for DNA probe immobilization and lowers the steric hindrance, hence leading to a higher hybridization efficiency.

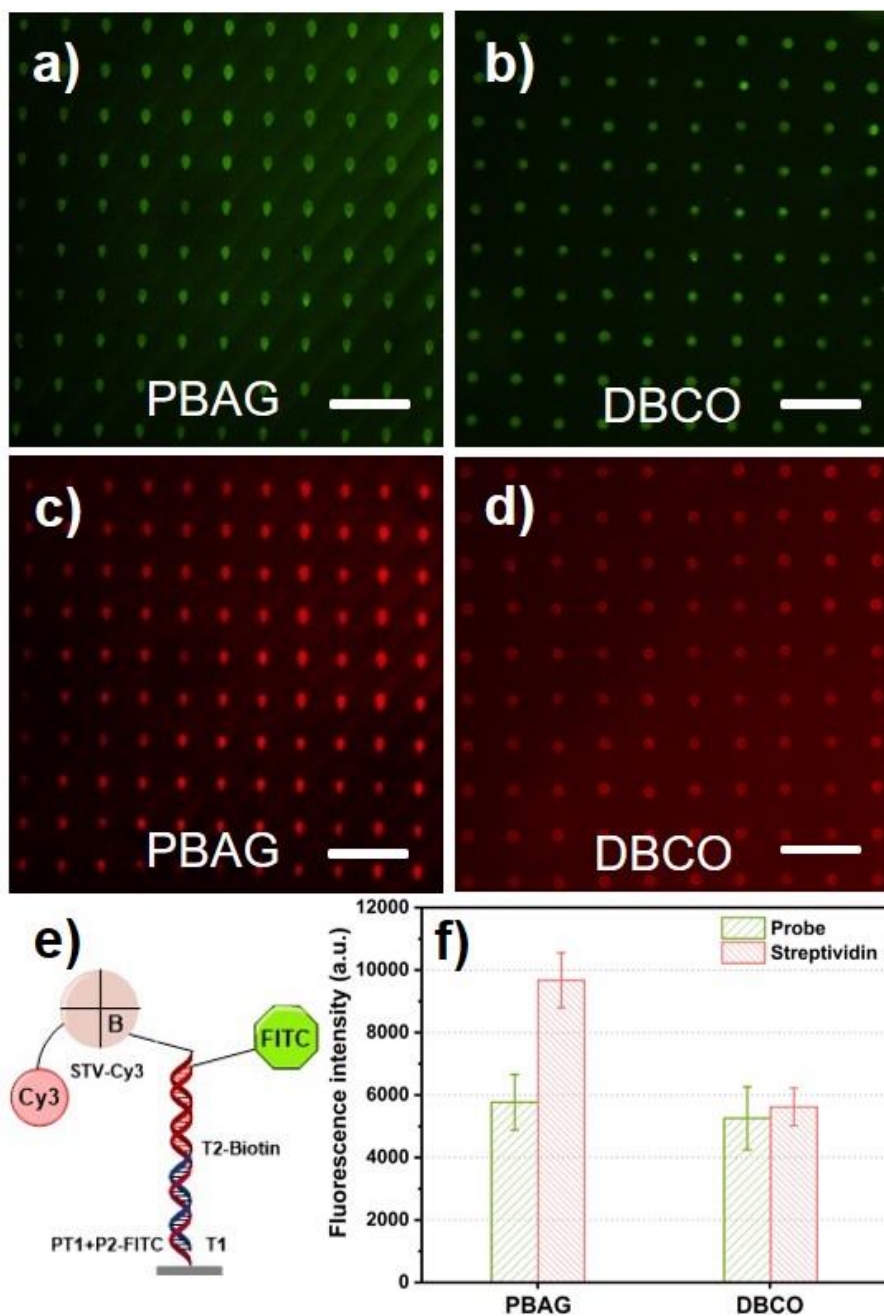


**Figure 5.10.** Fluorescence images captured on PT1+P2-FITC (green) immobilized arrays on a) PBAG-treated and b) DBCO-terminated chips after hybridization with T1 and T2-Biotin. Incubation of SA-Cy3 (red) on c) PBAG substrate, and on d) DBCO substrate after hybridization with T1 and T2-Biotin. e) Schematic drawing of DNA hybridization and protein binding protocols. f) The relative fluorescence intensity probe (green) and streptavidin (red) collected on picture (a), (b), (c) and (d), respectively. The exposure times are 1 s, and scale bars are 100  $\mu\text{m}$ .

### 5.3. Summary

In this chapter, we presented an investigation of the effects of the surface structure and conformation of three different kinds of platforms (gold on silicon, epoxide-functionalized polymer brush on glass, and alkyne-terminated SAM on glass) on DNA hybridization behaviors and efficiency via fluorescence imaging. We found that these three kinds of platforms were all even enough for immobilization of ssDNA probe arrays via  $\mu$ CS, while the gold-coated surface was the roughest one and the DBCO-SAM surface showed the minimum value of roughness. The hybridization experiments on gold-based samples showed that the strand orientation had a distinct influence on detection sensitivity, while it also exhibited drawbacks of quenching for fluorophores compared with the samples implemented on glass slides. Importantly, the PBAG-modified platforms, which had a bilayer polymer brush structure, demonstrated a higher efficiency of hybridization evaluated by fluorescence imaging, and were almost 40% higher than on DBCO-treated samples. Therefore, our results clue in the fabrication of DNA sensors for using a polymer-based interface, for example, the PBAG-modified surface, to gain a higher hybridization efficiency in fluorescence imaging detection strategies.

## Chapter 6 – Thesis summary and outlook

In summary, various platforms together with site-specific functionalization technology, microchannel cantilever spotting ( $\mu$ CS), were successfully employed in this dissertation to fabricate different biochips for bioscreening and biomedical applications. For the preparation of the platforms, different surface modification methods were used, e.g., “grafting from” and “grafting to” approaches for polymer brushes, self-assembled monolayers (SAMs), and metal film deposition. Moreover, inks either linked to a fluorophore or a non-fluorophore moiety were patterned and immobilized to the platforms via approaches of  $\mu$ CS and click reactions (alkyne-azide cycloaddition (AAC), thiol/yne, thiol/epoxy), respectively.

To address fouling issues and implement functional inks immobilization, an azide-bearing antifouling polymer brush (AAPB) was successfully synthesized by “grafting from” approach and patterned with cyclooctyne inks (DBCO/BCN) either linked to a fluorophore or a non-fluorophore moiety via  $\mu$ CS for high-efficient cyclooctyne screening or biomarker detection by fluorescent imaging. The AAPBs contain an antifouling block at the bottom that exhibits excellent unspecific protein repellency and circumvents any advancing blocking steps; and an azide-functionalized top block, that can mildly and efficiently react with cycloalkynes via SPAAC reactions. DBCO or BCN derivatives either linked to a fluorophore or a biotin species were printed on AAPBs via  $\mu$ CS for binding density and binding efficiency comparison between the DBCO/azide and the BCN/azide combinations. Streptavidin (Cy3 conjugated) binding experiments on biotin bearing spot patterns (DBCO/BCN-biotin) revealed that the DBCO derivatives show a higher surface density of molecular immobilization with azides than the BCN/azide system. Accordingly, another DBCO derivative (DBCO-NHS ester) was patterned to AAPBs to fabricate a newly and facilely fluorescent immunosensor for  $\alpha$ -fetoprotein (AFP) detection for diagnosis of hepatocellular carcinoma (HCC). The fluorescent immunosensor involves four technics together, i.e., SPAAC reaction for DBCO-containing capture array immobilization, amide bond formation (NHS ester/amine) for direct antibody anchoring regime or sandwich structures construction (biotin/streptavidin/biotin-antibody) for indirect antibody anchoring regime, the antigen-antibody interactions, and the fluorescent imaging technique.

Results revealed that the direct and indirect antibody anchoring strategies both work well for AFP detection, but the direct binding approach exhibits a compact fabrication process and is even more sensitive.

The methacrylate-based alkyne-bearing antifouling polymer brush (poly(HPMA-*b*-AlkMA)) was successfully synthesized via the “grafting from” method by conventional radical polymerization. The protein-repellent properties and the chemical reactivity toward CuAAC reaction of polymer brush were evaluated by selective protein binding assays by fluorescence imaging. The results reveal that the polymer brush shows excellent performances in repelling unspecific protein fouling and is highly reactive to bind azide derivatives (e.g., conjugated with fluorophores or moieties for protein coupling) via CuAAC reactions. While transforming the polymer brush coating to a diamond surface, we found that the unspecific background of the diamond was suppressed, and the signal-to-noise ratio was remarkably improved. Thus, the methacrylate-based alkyne-bearing antifouling polymer brush coating provides a novel solution to strengthen the target signal and lower the unspecific background on the diamond surface.

In DNA hybridization, the surface physicochemical properties of the sensor platforms usually play an important role in hybridization efficiency. Therefore, three different platforms (gold-deposited film, SAM-DBCO, “grafting to” PBAG polymer brush) carrying different physical topographies and chemical compositions were prepared to investigate the DNA hybridization behaviors with a fluorescent microscope. Consequently, the  $\mu$ CS and DNA directed-immobilization techniques were combined to pattern and immobilize SH-DNA probes to these platforms. The DNA probe immobilization procedures involved three reactions, i.e., Au-S bond formation, thiol/yne reaction, and thiol/epoxy reaction. The results showed that the hybridization processes all worked nicely on these platforms, while the polymer-based platform (PBAG-modified surface) demonstrated a higher hybridization efficiency according to the fluorescence intensity.

Last but not least, this thesis has demonstrated different bio-applications through the combination of different polymer-based biochips and a microarray technique. The author attempts to convince the readers that microarray functionalized polymer substrates are a class of promising biosensor candidates with a broad range of exciting application

opportunities. In future applications, polymer brushes could even facilitate biosensing of not only small and macromolecules, as proteins, but the concept being extended even to living cells. For example, macrophages, one of the most adherent cell types, play an important role in the immune response of the body, and two different phenotypes (M1 and M2) of them exist normally. The author and coworkers have already proved that the antifouling polymer brushes could repel the unwanted adhesion of macrophages and selectively capture them on the specific antibody functionalized micropatterns.<sup>[6]</sup> However, this achievement only can attach macrophages to some designated spaces, and the accurate phenotype sorting is still pending. In future work, the author aims to create multiplexing antibody arrays to sort macrophages in subtypes exactly. Additionally, as proofed in this thesis, the polymer-based platforms show great prospective in DNA hybridization. This platform together with DNA-directed immobilization technique for protein detection or cell screening, also merits further studies to bring them into a widespread application.

## Chapter 7 – Experimental section

### 7.1. Materials and chemicals

**Table 6.1.** List of materials and chemicals. All chemicals were used as received and without any further purification processes unless specified.

<b>Name</b>	<b>Supplier</b>
Ultrapure water	Produced in lab
Methanol	Merck (Germany)
Ethanol	Sigma-Aldrich (Germany)
Acetone	Sigma-Aldrich (Germany)
Chloroform	Sigma-Aldrich (Germany)
Acetic acid	Sigma-Aldrich (Germany)
Dimethyl sulfoxide	Sigma-Aldrich (Germany)
Glycerol	Sigma-Aldrich (Germany)
Toluene	Sigma-Aldrich (Germany)
Dichloromethane	Sigma-Aldrich (Germany)
Hydrogen peroxide	Sigma-Aldrich (Germany)
Ammonium hydroxide solution	Sigma-Aldrich (Germany)
(3-Aminopropyl)triethoxysilane	Sigma-Aldrich (Germany)
Poly(Bisphenol A-co-epichlorohydrin), glycidyl end-capped, Mn ~ 355 (PBAG)	Sigma-Aldrich (Germany)
Dibenzylcyclooctyne-PEG <sub>4</sub> -NHS ester	Jena Bioscience (Germany)
5-(and-6)-carboxytetramethylrhodamine	Thermo Scientific (USA)
Bovine serum albumin	Sigma-Aldrich (Germany)
Phosphate buffered saline	Sigma-Aldrich (Germany)
Dibasic potassium phosphate (K <sub>2</sub> HPO <sub>4</sub> )	Sigma-Aldrich (Germany)

Potassium phosphate monobasic (KH <sub>2</sub> PO <sub>4</sub> )	Sigma-Aldrich (Germany)
Trehalose dihydrate	Sigma-Aldrich (Germany)
Tween 20	Euroimmun (Germany)
[11-(2-Bromo-2-Methyl)Propionyloxy] Undecyltrichlorosilane (ATRP initiator)	Sigma-Aldrich (Germany)
CuBr	Sigma-Aldrich (Germany)
CuBr <sub>2</sub>	Sigma-Aldrich (Germany)
NaN <sub>3</sub>	Sigma-Aldrich (Germany)
2,2'-Bipyridyl, oligo (ethylene glycol) methyl ether methacrylate, Mn = 300 (OEGMA)	Sigma-Aldrich (Germany)
Glycidyl methacrylate (GMA)	Sigma-Aldrich (Germany)
Dibenzylcyclooctyne-PEG <sub>4</sub> -5/6-tetramethylrhodamine	Jena Bioscience (Germany)
Dibenzylcyclooctyne-PEG <sub>4</sub> -biotin conjugate	Jena Bioscience (Germany)
5-Carboxyfluorescein-PEG <sub>3</sub> -BCN	Conju-Probe (USA)
Biotin-PEG <sub>3</sub> -BCN	Conju-Probe (USA)
N,N-dimethylformamide	Sigma-Aldrich (Germany)
Streptavidin	Sigma-Aldrich (Germany)
Streptavidin-Cy3	Sigma-Aldrich (Germany)
Aluminium oxide 90 basic	Carl Roth (Germany)
NH <sub>2</sub> -PEG <sub>4</sub> -NH <sub>2</sub>	Sigma-Aldrich (Germany)
FITC-goat anti-mouse Ig (Polyclonal)	BD Biosciences (Germany)
AFP antibody (C3) [Biotin]	Novus Biologicals (Germany)
AFP polyclonal antibody	Thermo Fisher Scientific (Germany)
Streptavidin, Alexa fluor <sup>TM</sup> 647 conjugate	Thermo Fisher Scientific (Germany)
α-fetoprotein (source: human cord serum)	Lee BioSolutions, Inc. (USA)
Mouse IgG1 kappa Isotype control	Thermo Fisher Scientific (Germany)

Tamra-azide	Thermo Fisher Scientific (Germany)
Alexa fluor <sup>TM</sup> 488-azide	Thermo Fisher Scientific (Germany)
Cyanine 5-azide	Thermo Fisher Scientific (Germany)
Biotin-PEG <sub>4</sub> -azide	Jena Bioscience (Germany)
3-Methacryloxypropyltrimethoxysilane (MEMO)	Sigma-Aldrich (Germany)
Copper sulfate (CuSO <sub>4</sub> )	Sigma-Aldrich (Germany)
Sodium ascorbate (Na-As)	Sigma-Aldrich (Germany)
Bovine serum albumin FITC conjugate (BSA-FITC)	Sigma-Aldrich (Germany)
Azobis(isobutyronitrile) (AIBN)	Sigma-Aldrich (Germany)

All single-stranded oligonucleotides containing thiol-conjugated probes (PT1, PT1-FITC, PT1+P2, PT1+P2-FITC), and target oligomers (T1, T1-Cy3, T1-Cy5, T2-Cy5, T2-Biotin) purchased from Sigma-Aldrich (Germany), and the sequences are shown in table 6.2. Notably, the 22mer sequences are named “short” ones, and the 44mer sequences are named “long” ones.

**Table 7.2.** Sequence of oligonucleotides.

Oligonucleotide	Sequence [5'-3']
PT1 (22mer)	GGA CGA ATA CAA AGG CTA CAC G-[ThiC3]
PT1-FITC	[6FAM]-GGA CGA ATA CAA AGG CTA CAC G-[ThiC3]
PT2	GTG GAA AGT GGC AAT CGT GAA G-[ThiC3]
PT1+P2 (44mer)	GGA CGA ATA CAA AGG CTA CAC GGTG GAA AGT GGC AAT CGT GAA G-[ThiC3]
PT1+P2-FITC	[6FAM]-GGA CGA ATA CAA AGG CTA CAC GGTG GAA AGT GGC AAT CGT GAA G-[ThiC3]
T1	C GTG TAG CCT TTG TAT TCG TCC
T1-Cy3	[Cyanine3]-C GTG TAG CCT TTG TAT TCG TCC

T1-Cy5	[Cyanine5]-C GTG TAG CCT TTG TAT TCG TCC
T2-Cy5	[Cyanine5]-C ACC TTT CAC CGT TAG CAC TTC
T2-Biotin	[Biotin]-C ACC TTT CAC CGT TAG CAC TTC

## 7.2. Equipments for experiments

### 7.2.1. Patterning by microchannel cantilever spotting ( $\mu$ CS)

The spotting strategy for surface patterns was implemented with a NLP 2000 system (NanoInk, USA). Briefly described: prior to mounting the surface patterning tool (SPT) (SPT-S-C30S, Bioforce Nanosciences, USA) on a holder, SPT probes were hydrophilized by oxygen plasma activation (10 sccm O<sub>2</sub>, 0.2 mbar, 100 W, for 2 min, ATTO plasma system, Diener electronics, Germany). After activation, 0.2  $\mu$ L of ink solution was loaded on the reservoir of the probe immediately and then it was mounted to the holder on the NLP 2000 system to conduct pattern writing. Dot patterns were designed of (10  $\times$  10) or (5  $\times$  5) spot arrays with a pitch of 50  $\mu$ m in each direction. Typically, the spotting procedures were implemented at a series of relative humidity in the range of 20 ~ 70% and various dwell time from 0.1 s to 1.5 s.

### 7.2.2. Water contact angle (WCA)

The static WCA measurements were performed on an OCA-20 contact angle analyzer (DataPhysics Instruments GmbH, Germany) at room temperature. Every sample was measured 3 times. Briefly, a 3  $\mu$ L drop was dispensed on a substrate, and after 1 min of stabilization of the water drop the contact angle was measured. The whole process was conducted by the on-board software and recorded by the built-in camera.

### 7.2.3. Film thickness measurement

The thickness of films and coatings was measured with a spectroscopic ellipsometry (M 2000, Woollam Co., Inc., Lincoln NE, USA) on silicon substrates in dry conditions at an incident angle of 65° in the wavelength range of  $\lambda = 370 \sim 900$  nm. All measurements were evaluated with an optical box model on the software CompleteEase, and silicon substrates

were all fitted with standard values for Si and SiO<sub>2</sub> as defined in the software. The thickness and the optical properties of the polymer layers were fitted with a Cauchy relation model.

#### **7.2.4. Atomic force microscopy (AFM)**

To evaluate the surface topography of different substrates, an atomic force microscopy (AFM, Dimension Icon, Bruker, Germany) was employed. The measurements were conducted at room temperature in air in tapping mode (Cantilever type, 40 N m<sup>-1</sup>, 325 kHz, HQ:NSC15/Al BS, MicroMasch, Germany). For each sample, 3 random positions were scanned (each 5 × 5 μm<sup>2</sup> or 10 × 10 μm<sup>2</sup>) and the roughness R<sub>a</sub> was extracted by the onboard software of the instrument.

#### **7.2.5. X-ray photoelectron spectroscopy (XPS)**

The analysis of chemical compositions of the surfaces was identified by X-ray photoelectron spectroscopy (XPS) using a Thermo Scientific K-Alpha system (XPS, Thermo Fisher Scientific, East Grinstead, UK) with a base pressure of about 2 × 10<sup>-9</sup> mbar. Excitation was done using monochromatic Al-Kα-X-rays. The energy calibration of the system was done according to ISO 15472:2001 using copper, silver, and gold reference samples. The transmission function was determined using the build in thermo standard method on a silver reference sample. Quantification of the measurement results was done using modified scofield sensitivity factors. A 400 μm x-ray spot was used for the analysis. On the non-conducting samples, a flood gun was used for compensating charging.

#### **7.2.6. Fluorescent microscopy**

The fluorescent images were recorded on a Nikon Eclipse 80i upright fluorescence microscope (Nikon, Japan) integrated with an Intensilight illumination (Nikon, Japan), and a CoolSNAP HQ2 camera (Photometrics, USA), and Texas Red, Cy5, and FITC filters set (Nikon Y-2E/C).

## 7.3. Experimental methods

### 7.3.1. Screening of high-efficient cyclooctyne on azide-bearing antifouling polymer brushes (AAPBs)

#### 7.3.1.1. Grafting of azide-bearing antifouling polymer brushes (AAPBs)

The AAPBs employed herein possessing a hierarchical structure and was synthesized by “grafting from” strategy. The hierarchical structure contains an antifouling block at the bottom and an azide functionalized block at the top. The full synthesis protocol of AAPBs is described below. Before doing plasma cleaning, substrates (either silicon wafer ( $10 \times 10$  mm, used in ellipsometric characterizations) or round glass substrates (13 mm diameter)) were sonicated in chloroform, ethanol, and water for 5 min each, and then dried with a stream of nitrogen. After that, substrates were plasma treated (10 sccm  $O_2$ , 0.2 mbar, and 100 W) in an ATTO system, Diener electronics (Germany) for 20 min. Without delay, the hydroxylated substrates were soaked in a freshly prepared solution of initiator in anhydrous toluene ( $1 \text{ mg mL}^{-1}$ ) for 3 h. To obtain a homogeneously SAM initiator on the chip surfaces, the immobilization procedure was done in a dry environment. When finished, the substrates were rinsed with toluene, acetone, ethanol, and water, and then blown with nitrogen for drying before the next step.

Prior to grafting the antifouling block and azido block on the initiator layer, the inhibitors were removed by passing the monomers through an alumina column. Here we depict the protocol concisely: As the whole reaction process must be in oxygen-free conditions, all the containers and mixtures were deoxygenized with  $N_2$  for 1 h before implementing the next step. For synthesis of the bottom layer, methanol (5 mL), catalysts and monomer solution were placed in three round-bottom flasks and degassed with  $N_2$  for 1 h, separately. The catalyst mixture contained 2,2'-bipyridyl (155 mg, 991  $\mu\text{mol}$ ),  $CuBr_2$  (16.8 mg, 75  $\mu\text{mol}$ ), and  $CuBr$  (53.8 mg, 375  $\mu\text{mol}$ ). A solution of OEGMA (5.9 g, 19 mmol) in 5 mL ultrapure water constituted the monomer solution. After 1 h of degassing, methanol (5 mL) was transferred into the flask containing catalysts and then stirred under  $N_2$  protection to obtain the catalyst solution. Without delay, the monomer solution was transferred into the flask containing the catalyst solution to obtain the precursor solution. Subsequently, the

precursor solution was gently injected into a container containing the initiator SAM-modified substrates under  $N_2$  environment. The reaction was conducted at  $30^\circ\text{C}$  for 30 min, and then stopped by removing the substrates from the container. The substrates were rinsed with ethanol and water twice and dried with a stream of nitrogen. The ellipsometric thickness of obtained poly(OEGMA) layer was approximately 24.3 nm in dry conditions.

The next two procedures were growing the top layer of the polymer brushes and functionalizing the epoxy terminals with azido groups. Here, the poly(OEGMA) obtained in the last step acted as macroinitiators for the growing of the top block. Fresh GMA without inhibitor (6.7 mL, 49 mmol), dry N,N-Dimethylformamide (DMF, 10 mL), 2,2'-bipyridyl (191 mg, 1222  $\mu\text{mol}$ ), and  $\text{CuBr}_2$  (21.8 mg, 98  $\mu\text{mol}$ ) were added to a round-bottom flask and bubbled with  $N_2$  for 1 h, after which  $\text{CuBr}$  (70.1 mg, 489  $\mu\text{mol}$ ) was added, and then the mixture was stirred thoroughly until full dissolution. Straight after, the fully mixed solution was slowly injected into a previously deoxygenated reactor containing the poly(OEGMA) coated substrates obtained in the last step. The growth was allowed to proceed at  $60^\circ\text{C}$  for 6 h. Subsequently, the substrates were removed from the reactor and rinsed with DMF, dichloromethane, acetone, and water twice of each and dried under a stream of nitrogen. The entire dry thickness of the poly(OEGMA-*b*-GMA) was 32.7 nm, and the corresponding thickness of the top block, therefore, 8.4 nm. To finally obtain the azido functionalized diblock polymer brushes, a nucleophilic epoxide ring-opening with azide was carried out by immersing the substrates into a solution of  $\text{NaN}_3$  (3.4 mg  $\text{mL}^{-1}$ ) in anhydrous DMF at  $60^\circ\text{C}$  for 24 h. Afterwards, the substrates were rinsed with DMF, ethanol and water twice each and dried with nitrogen. For characterization of the antifouling property of AAPBs via SPR, SAM of  $\omega$ -mercaptoundecyl bromoisobutyrate was immobilized on gold-coated glass sensor chips as the initiator for polymer brush growing, and the grafting method was the same as aforementioned.

#### 7.3.1.2. Cyclooctyne ink solution preparation

In order to prevent premature evaporation of the inks during printing, all ink solutions were admixed with glycerol. For storage, inks were kept in dark at  $-20^\circ\text{C}$ . The concentration of the fluorescent dyes employed (DBCO-Tamra and BCN-FAM) in a mixture of DMSO/glycerol (7:3, v/v) was  $500 \mu\text{g mL}^{-1}$ . Analogously, DBCO-Biotin and

BCN-Biotin, were dissolved at a concentration range from 500 to 3000  $\mu\text{g mL}^{-1}$  in a mixture of DMSO/glycerol (7:3, v/v).

#### 7.3.1.3. Coupling of cyclooctynes to AAPBs via SPAAC reactions

After surface patterning, the target molecules, DBCO-Tamra and BCN-FAM, were allowed to couple to the AAPBs substrates for different durations in the range of 5 to 240 min either at 25 or 37°C, respectively. Subsequently, samples were rinsed with PBS 3 times to remove excess ink and then blew dry with nitrogen. A similar protocol was performed for the non-fluorescent targets with different concentrations at a fixed temperature of 37°C, but 15 min for DBCO-Biotin and 20 min for BCN-Biotin.

#### 7.3.1.4. Protein binding on biotinylated dot arrays

A fluorescently labeled protein, streptavidin-Cy3, was used to bind with the immobilized biotin derivatives. In this procedure, the merits of di-block polymer brushes were exhibited thoroughly. Usually, bovine serum albumin (BSA) or a similar agent is necessary as a blocking reagent for the protein binding process, but in this chapter, the antifouling di-block polymer brushes conveniently allowed to omit the blocking process completely. The arrayed biotin derivatives were incubated with 100  $\mu\text{L}$  of 1  $\text{mg mL}^{-1}$  streptavidin-Cy3 in PBS (1:100) at 37°C for 30 min in a dark environment. Subsequently, samples were rinsed with PBS 3 times and blown dry under a stream of nitrogen before conducting fluorescence microscopy.

### 7.3.2. A fluorescent immunosensor for $\alpha$ -fetoprotein (AFP) detection

#### 7.3.2.1. Fabrication of sensor platforms

The substrates employed in this chapter were also AAPBs, and the fabrication protocol can be found in 6.3.1.1.

#### 7.3.2.2. Ink solution preparation

The ink solution was prepared by dissolving DBCO-NHS ester or DBCO-Biotin in DMSO, notably, 30% (v/v) of glycerol was added into the solvent to prevent fast evaporation while printing, and the final concentration of the ink was 2  $\text{mg mL}^{-1}$ .

### 7.3.2.3. Fluorophore linked AFP solution preparation

Rhodamine-NHS ester was used to label AFP antigen, which is according to the efficient reaction between the succinimidyl-ester and the  $-NH_2$  groups in the protein skeleton in weakly alkaline conditions (e.g., pH 7 ~ 9). Prior to labeling step, the AFP solution was dialyzed in PBS to replace the tris(hydroxymethyl)aminomethane buffer solution with PBS. After that, rhodamine-NHS ester was added to the AFP solution at a 10 ~ 15-fold molar excess, after 6 hrs reaction, the mixture was dialyzed again to remove the extra rhodamine.

### 7.3.2.4. Phosphate buffered saline (PBS) preparation

Thoroughly dissolving 35.9 g  $K_2HPO_4$  into 500 mL DI water as solution A, and dissolving 2.76 g  $KH_2PO_4$  into 100 mL DI water as solution B. After that, Mixing 216 mL of solution A and 8 mL of solution B together to get the phosphate buffered saline, and the final pH value of the mixture was 8.4.

### 7.3.2.5. Immobilization of antibody capture arrays

After surface patterning (20% r.H., 0.1 s dwell time), the DBCO-NHS ester arrays were allowed to couple to the polymer brush substrates for 15 min at 37°C according to the results obtained in chapter 2. Subsequently, the samples were rinsed with PBS (pH 7.4) 3 times to remove the excess ink and then incubated with antibody solution immediately for the direct binding strategy. A similar protocol was used for the DBCO-Biotin arrays, but after washing off the excess ink, streptavidin was used on the samples to construct sandwich structures for antibody (biotin conjugate) anchoring (indirect binding strategy).

### 7.3.2.6. Antibody anchoring and detection of AFP

Initially, SA-AF647 was used to explore the optimum reaction conditions between NHS ester and amino. Detailedly, SA-AF647 solution ( $200 \mu\text{g mL}^{-1}$  in PBS, pH 8.4) was covered on the samples, which were spotted with NHS ester capture arrays, and then the binding procedures were implemented at 25 and 37°C for different intervals (10 ~ 60 min). Subsequently, the samples were washed with PBS (pH 8.4) 3 times and then blown dry under a stream of nitrogen before being observed with a fluorescent microscope to determine the optimal reaction conditions. Analogously, to find the optimal detection conditions of AFP, testing experiments were implemented by incubation of AFP-rhodamine ( $200 \mu\text{g mL}^{-1}$  in PBS) on antibody arrays with a series of incubation times at

25°C and 37°C, respectively. Thereafter, the optimal reaction conditions in each step were used for the sensitivity study of AFP detection. Additionally, in the direct binding strategy, a solution of NH<sub>2</sub>-PEG<sub>4</sub>-NH<sub>2</sub> (1:100 in PBS, pH 8.4, v/v) was used to treat the samples after the antibody anchoring step to exclude the potentially diverse effects on the detection process by the residual NHS ester moieties. A similar protocol was conducted for the indirect binding strategy after constructing the sandwich structures.

### **7.3.3. Improvement of signal-to-noise ratio of the diamond surface by methacrylate-based polymer brush coating**

#### 7.3.3.1. Diamond film preparation

Double-side polished (001) HPHT diamonds ( $3 \times 3 \times 0.3 \text{ mm}^3$ , Element Six, UK) were used as a substrate and overgrown with an approx. 20  $\mu\text{m}$  thick ultrapure diamond film to suppress background fluorescence by the diamond substrate. An ellipsoidal microwave plasma chemical vapor deposition (MPCVD) (915 MHz) reactor with purified gases (hydrogen and methane) was employed for diamond growth.<sup>[260]</sup> After growth the samples were polished to achieve a surface roughness of below 1 nm. All samples were cleaned in a 3:1 mixture of sulfuric and nitric acid at 250°C.

#### 7.3.3.2. Methacrylate-based polymer brush coated substrates preparation

Glass slides ( $10 \times 10 \text{ mm}$ ) and diamond chips ( $3 \times 3 \text{ mm}$ ) were cleaned by sonication in chloroform, ethanol, and water for 5 min each and then dried with nitrogen. Straight after, plasma treatment (10 sccm O<sub>2</sub>, 0.2 mbar and 100 W, ATTO plasma system, Diener electronics, Germany) was done 5 min for glass and 30 s for diamond, respectively. Subsequently, the hydroxylated substrates were immersed in a freshly prepared MEMO solution in toluene (1%, v/v) overnight at room temperature in dark, and then the substrates were washed with toluene, ethanol, and water, and dried under a nitrogen stream. The polymer brush was “grafting from” a methacrylate silanized surface by conventional radical polymerization. Briefly, HPMA (700 mg, 4.82 mmol), AlkMA (35 mg, 0.06 mmol), and AIBN (200 mg, 1.22 mmol) were dissolved in DMSO (2.1 mL). After completely dissolving, the mixture was added to a flask containing silanized substrates. The polymerization was conducted under nitrogen at 55°C for one day or for four days. While

finishing, the substrates were washed with ethanol and water twice each and blown dry by nitrogen.

#### 7.3.3.3. Ink solution preparation

Ink solutions for CuAAC were based on copper sulfate (10 mM), and sodium ascorbate (20 mM) solutions in ultrapure water, that were mixed with azide conjugated compounds. An amount of 20% (v/v) of glycerol was added to the ink solutions as an ink carrier and to avoid over quick evaporation of the ink solvent. The final concentration of the ink solution was 0.5 mg/mL.

#### 7.3.3.4. Aide ink immobilization and protein binding protocol

After printing (30% r.H., 0.1 s dwell time), the azide functionalized samples were allowed to rest overnight at room temperature in the dark environment to complete the CuAAC reaction. After washing with PBS 3 times, the protein binding assays were implemented on biotinylated samples, which were incubated with PBS or BSA in advance. Subsequently, samples were rinsed with PBS 3 times and blown dry under a stream of nitrogen before conducting fluorescence imaging.

### **7.3.4. Fabrication of different sensing platforms for DNA hybridization**

#### 7.3.4.1. Preparation of sensing platforms

The PBAG polymer-based substrates were fabricated by “grafting to” strategy. The PBAG components ( $M_n \sim 355$ ) were bought as pre-polymerized. Begin by, the glass coverslips or silicon slides were cleaned with an aqueous solution consisting of 14.3%  $\text{NH}_3$ , and 14.3%  $\text{H}_2\text{O}_2$  in ultrapure water at  $150^\circ\text{C}$  for 20 minutes. Immediately after, the slides were washed with ultrapure water, ethanol, and ultrapure water again, and dried under a nitrogen stream. Afterwards, the slides were immersed in a freshly prepared 1% APTES solution (95% methanol, 5%  $\text{H}_2\text{O}$ , 1 mM acetic acid) for 20 minutes to obtain amino silane-derived SAMs on the slides. The substrates were then washed with ethanol, ultrapure water, and acetone, and dried under a  $\text{N}_2$  stream. Finally, the aminated slides were soaked in an acetone solution containing 5% PBAG overnight at room temperature to complete the epoxide ring-opening with primary amine and graft PBAG molecules to the  $-\text{NH}_2$  layer. While finishing, the slides were washed with acetone, dried under a nitrogen stream and stored at  $-20^\circ\text{C}$ .

The DBCO-terminated surfaces were prepared as the description below. Briefly, substrates were cleaned with chloroform, ethanol, and water using an ultrasonic bath for 5 minutes each to remove the surface organic contaminants, and then dried with a stream of nitrogen. Followed by, the slides were hydroxylated by oxygen plasma (10 sccm O<sub>2</sub>, 0.2 mbar, 100 W) in an ATTO system, Diener electronics (Germany) for 2 min. Without delay, the glass slides were functionalized with DBCO by immersing in a DBCO-NHS ester solution (1 mg mL<sup>-1</sup>) in dichloromethane overnight at room temperature. Finally, the slides were rinsed thoroughly with dichloromethane, acetone, ethanol, and water, and then dried by blowing with nitrogen. The completed chips were stored in dark in a desiccator.

The gold-coated Si substrates were prepared by evaporating 100 nm Au on 7 nm Cr. Prior to use, the gold substrates were sonicated with chloroform, ethanol, and water for 5 minutes each, and then dried with a stream of nitrogen. After that further cleaning with an oxygen plasma cleaner for 2 minutes (10 sccm O<sub>2</sub>, 0.2 mbar, 100 W).

#### 7.3.4.2. DNA ink preparation

The ink solutions were prepared by dissolving oligonucleotides in a mixture of Trehalose buffer and glycerol (v/v, 8:2) at a concentration of 100 μM. The added glycerol was to avoid premature drying of the ink and also acted as an ink carrier. The Trehalose buffer containing 200 mM K<sub>2</sub>HPO<sub>4</sub>, 200 mM KH<sub>2</sub>PO<sub>4</sub>, 0.5% v/v Trehalose-Dihydrate, and 0.1% v/v Tween 20. The ink solutions were stored at 4°C in dark for further usage.

#### 7.3.4.3. Hybridization protocol

Arrays containing probe-oligonucleotides spotted by SPT-tips (30 ~ 40% r.H., 0.5 s dwell time) were allowed to rest overnight to complete the binding process between the thiol groups contained in oligonucleotides and the DBCO or PBAG or gold surfaces, and then washed three time by pipetting with PBS to remove the excess ink solution. Straight after, the sample was blocked with 50 μL BSA for 30 min to diminish potentially non-specific fouling of the target DNA or the protein. Subsequently, 50 μL of target ssDNA (1 μM) was covered on the sample surface at room temperature for 1.5 h to perform the hybridization process, and then washed with PBS 3 times, and dried with nitrogen. For the second hybridization step, a similar procedure aforementioned was used.

#### 7.3.4.4. Protein binding assay on hybridized DNA arrays

To implement protein binding on hybridized chips, a mixture containing streptavidin-Cy3 ( $1 \text{ mg mL}^{-1}$ ) and PBS (v/v, 1:100) was incubated on DNA arrays that were previously hybridized with compartments bearing biotin conjugates for 30 minutes. Afterwards, the chips were washed by pipetting on and off PBS three times and then dried by blowing with nitrogen for microscope observation.

---

**References**

- [1] E. Ruckenstein, Z. F. Li, *Adv. Colloid Interfac.* **2005**, *113*, 43-63.
- [2] P. H. Lin, B. R. Li, *Analyst* **2020**, *145*, 1110-1120.
- [3] S. Kumar, F. Ye, S. Dobretsov, J. Dutta, *Front. Nanotechnol.* **2021**, *3*, 771098.
- [4] T. Wei, Q. Yu, W. Zhan, H. Chen, *Adv. Healthcare Mater.* **2016**, *5*, 449-456.
- [5] T. Wei, Z. Tang, Q. Yu, H. Chen, *ACS Appl Mater Interfaces* **2017**, *9*, 37511-37523.
- [6] J. Striebel, M. Vorobii, R. Kumar, H.-Y. Liu, B. Yang, C. Weishaupt, C. Rodriguez-Emmenegger, H. Fuchs, M. Hirtz, K. Riehemann, *Adv. NanoBiomed Res.* **2020**, *1*, 2000029.
- [7] H. Cui, P. Zhang, W. Wang, G. Li, Y. Hao, L. Wang, S. Wang, *Nano Res.* **2017**, *10*, 1345-1355.
- [8] Q. Wang, J. Wang, Y. Huang, Y. Du, Y. Zhang, Y. Cui, D. M. Kong, *Biosens. Bioelectron.* **2021**, *197*, 113739.
- [9] R. Meyer, S. Giselbrecht, B. E. Rapp, M. Hirtz, C. M. Niemeyer, *Curr. Opin. Chem. Biol.* **2014**, *18*, 8-15.
- [10] S. M. M. Dadfar, S. Sekula-Neuner, V. Trouillet, H. Y. Liu, R. Kumar, A. K. Powell, M. Hirtz, *Beilstein J. Nanotechnol.* **2019**, *10*, 2505-2515.
- [11] S. K. Nemani, R. K. Annavarapu, B. Mohammadian, A. Raiyan, J. Heil, M. A. Haque, A. Abdelaal, H. Sojoudi, *Adv. Mater. Interfaces* **2018**, *5*, 1801247.
- [12] F. Yan, Y. Jiang, X. Sun, Z. Bai, Y. Zhang, X. Zhou, *Mikrochim. Acta* **2018**, *185*, 424.
- [13] S. Khan, G. Newaz, *J. Biomed. Mater. Res. A* **2010**, *93*, 1209-1224.
- [14] H. Amani, H. Arzaghi, M. Bayandori, A. S. Dezfuli, H. Pazoki - Toroudi, A. Shafiee, L. Moradi, *Adv. Mater. Interfaces* **2019**, *6*, 1900572.
- [15] T. Hanawa, *Dent. Mater. J.* **2017**, *36*, 533-538.
- [16] N. S. N. Hasnan, M. A. Mohamed, Z. A. Mohd Hir, *Adv. Mater. Technol.* **2021**, 2100993.
- [17] R. Wang, M.-S. Xu, X.-D. Pi, *Chin. Phys. B* **2015**, *24*, 086807.
- [18] A. Muck, A. Svatos, *Talanta* **2007**, *74*, 333-341.

- [19] D. J. Slade, V. Subramanian, J. Fuhrmann, P. R. Thompson, *Biopolymers* **2014**, *101*, 133-143.
- [20] W. Wang, C. Xue, X. Mao, *Int. J. Biol. Macromol.* **2020**, *164*, 4532-4546.
- [21] G. S. Kaliaraj, T. Siva, A. Ramadoss, *J. Mater. Chem. B* **2021**, *9*, 9433-9460.
- [22] A. Shakeri, S. Khan, T. F. Didar, *Lab Chip* **2021**, *21*, 3053-3075.
- [23] W. Long, H. Ouyang, X. Hu, M. Liu, X. Zhang, Y. Feng, Y. Wei, *Int. J. Biol. Macromol.* **2021**, *186*, 591-615.
- [24] Z. Guo, S. Chakraborty, F. A. Monikh, D. D. Varsou, A. J. Chetwynd, A. Afantitis, I. Lynch, P. Zhang, *Adv. Biology* **2021**, *5*, 2100637.
- [25] M. Bhatt, P. Shende, *J. Mater. Chem. B* **2022**, *10*, 1176-1195.
- [26] M. Singh, N. Kaur, E. Comini, *J. Mater. Chem. C* **2020**, *8*, 3938-3955.
- [27] L. Wang, U. S. Schubert, S. Hoepfener, *Chem. Soc. Rev.* **2021**, *50*, 6507-6540.
- [28] C. Nicosia, J. Huskens, *Mater. Horiz.* **2014**, *1*, 32-45.
- [29] J. Wang, F. Wu, M. Watkinson, J. Zhu, S. Krause, *Langmuir* **2015**, *31*, 9646-9654.
- [30] S. Ahoulou, E. Perret, J. M. Nedelec, *Nanomaterials* **2021**, *11*, 999.
- [31] V. Singh, P. C. Mondal, A. K. Singh, M. Zharnikov, *Coord. Chem. Rev.* **2017**, *330*, 144-163.
- [32] S. Casalini, C. A. Bortolotti, F. Leonardi, F. Biscarini, *Chem. Soc. Rev.* **2017**, *46*, 40-71.
- [33] S. Watson, M. Nie, L. Wang, K. Stokes, *RSC Adv.* **2015**, *5*, 89698-89730.
- [34] X. Zhang, D. Brodus, V. Hollimon, H. Hu, *Chem. Cent. J.* **2017**, *11*, 18.
- [35] L. A. E. J. Christopher Love, Jennah K. Kriebel, Ralph G. Nuzzo, George M. Whitesides, *Chem. Rev.* **2005**, *105*, 1103-1170.
- [36] X. Yan, J. Tang, D. Tanner, J. Ulstrup, X. Xiao, *Catalysts* **2020**, *10*, 1458.
- [37] S. P. Pujari, L. Scheres, A. T. Marcelis, H. Zuilhof, *Angew. Chem.* **2014**, *53*, 6322-6356.
- [38] L. Upadhyaya, X. Qian, S. Ranil Wickramasinghe, *Curr. Opin. Chem. Eng.* **2018**, *20*, 13-18.
- [39] H. Jin, L. Tian, W. Bing, J. Zhao, L. Ren, *Prog. Mater. Sci.* **2022**, *124*, 100889.

- [40] A. M. C. Maan, A. H. Hofman, W. M. Vos, M. Kamperman, *Adv. Funct. Mater.* **2020**, *30*, 2000936.
- [41] L. Deng, W. Guo, H. H. Ngo, H. Zhang, J. Wang, J. Li, S. Xia, Y. Wu, *Bioresour Technol.* **2016**, *221*, 656-665.
- [42] G. D. Bixler, B. Bhushan, *Phil. Trans. R. Soc. A* **2012**, *370*, 2381-2417.
- [43] B. Yameen, A. Farrukh, *Chem. Asian J.* **2013**, *8*, 1736-1753.
- [44] V. B. Damodaran, N. S. Murthy, *Biomater. Res.* **2016**, *20*, 18.
- [45] L. Delauney, C. Compère, M. Lehaitre, *Ocean Sci.* **2010**, *6*, 503-511.
- [46] J. S. S. Silke Megelski, D. Bruce Chase, John F. Rabolt, *Macromolecules* **2002**, *35*, 8456-8466.
- [47] R. G. C. Emanuele Ostuni, R. Erik Holmlin, Shuichi Takayama, George M. Whitesides, *Langmuir* **2001**, *17*, 5605-5620.
- [48] R. Wang, X. Zhou, X. Zhu, C. Yang, L. Liu, H. Shi, *ACS Sens.* **2017**, *2*, 257-262.
- [49] I. Francolini, C. Vuotto, A. Piozzi, G. Donelli, *APMIS* **2017**, *125*, 392-417.
- [50] Z. Wang, L. Scheres, H. Xia, H. Zuilhof, *Adv. Funct. Mater.* **2020**, *30*, 1908098.
- [51] H. Thérien-Aubin, L. Chen, C. K. Ober, *Polymer* **2011**, *52*, 5419-5425.
- [52] Y. N. Chou, A. Venault, C. H. Cho, M. C. Sin, L. C. Yeh, J. F. Jhong, A. Chinnathambi, Y. Chang, Y. Chang, *Langmuir* **2017**, *33*, 9822-9835.
- [53] C. K. O. Amanda K. Leonardi, *Annu. Rev. Chem. Biomol. Eng.* **2019**, *10*, 241-264.
- [54] J. A. F. Chakravarthy S. Gudipati, James A. Callow, Maureen E. Callow, and Karen L. Wooley, *Langmuir* **2005**, *21*, 3044-3053.
- [55] G. P. Sakala, M. Reches, *Adv. Mater. Interfaces* **2018**, *5*, 1800073.
- [56] E. Oblak, A. Piecuch, A. Krasowska, J. Luczynski, *Microbiol. Res.* **2013**, *168*, 630-638.
- [57] M. Fu, Y. Liang, X. Lv, C. Li, Y. Y. Yang, P. Yuan, X. Ding, *J. Mater. Sci. Technol.* **2021**, *85*, 169-183.
- [58] M. R. Gopikrishnan V., Raasaiyah Pazhanimurugan, Thangavel Shanmugasundaram, R. Balagurunathan, *J. Chem. Pharm. Res.* **2015**, *7*, 1144-1153.
- [59] Z. Huang, H. Ghasemi, *Adv. Colloid. Interfac.* **2020**, *284*, 102264.

- [60] W.-L. Chen, R. Cordero, H. Tran, C. K. Ober, *Macromolecules* **2017**, *50*, 4089-4113.
- [61] L. L. Raphael Barbey, Dusko Paripovic, Nicolas Schuwer, Caroline Sugnaux, Stefano Tugulu, Harm-Anton Klok, *Chem. Rev.* **2009**, *109*, 5437-5527.
- [62] Y. Cai, D. K. Schwartz, *ACS Appl. Mater. Interfaces* **2016**, *8*, 511-520.
- [63] U. Bog, A. de los Santos Pereira, S. L. Mueller, S. Havenridge, V. Parrillo, M. Bruns, A. E. Holmes, C. Rodriguez-Emmenegger, H. Fuchs, M. Hirtz, *ACS Appl. Mater. Interfaces* **2017**, *9*, 12109-12117.
- [64] S. Ma, X. Zhang, B. Yu, F. Zhou, *NPG Asia Mater.* **2019**, *11*, 24.
- [65] F. Wang, H. Zhang, B. Yu, S. Wang, Y. Shen, H. Cong, *Prog. Org. Coat.* **2020**, *147*, 105860.
- [66] S. Campuzano, M. Pedrero, P. Yanez-Sedeno, J. M. Pingarron, *Int. J. Mol. Sci.* **2019**, *20*, 423.
- [67] Y. Chang, *J. Polym. Res.* **2022**, *29*, 286.
- [68] H. W. Chien, C. C. Tsai, W. B. Tsai, M. J. Wang, W. H. Kuo, T. C. Wei, S. T. Huang, *Colloid. Surface B* **2013**, *107*, 152-159.
- [69] S. C. Lange, E. van Andel, M. M. J. Smulders, H. Zuilhof, *Langmuir* **2016**, *32*, 10199-10205.
- [70] M. Li, B. Zhuang, J. Yu, *Chem. Asian J.* **2020**, *15*, 2060-2075.
- [71] D. Li, Q. Wei, C. Wu, X. Zhang, Q. Xue, T. Zheng, M. Cao, *Adv. Colloid. Interfac.* **2020**, *278*, 102141.
- [72] Y. Xia, V. Adibnia, R. Huang, F. Murschel, J. Faivre, G. Xie, M. Olszewski, G. De Crescenzo, W. Qi, Z. He, R. Su, K. Matyjaszewski, X. Banquy, *Angew. Chem.* **2018**, *58*, 1308-1314.
- [73] S. Chen, L. Li, C. Zhao, J. Zheng, *Polymer* **2010**, *51*, 5283-5293.
- [74] E. Luong-Van, I. Rodriguez, H. Y. Low, N. Elmouelhi, B. Lowenhaupt, S. Natarajan, C. T. Lim, R. Prajapati, M. Vyakarnam, K. Cooper, *J. Mater. Res.* **2012**, *28*, 165-174.
- [75] T. M. D. Rana, *Chem. Rev.* **2010**, *110*, 2448-2471.
- [76] D. Murakami, H. Jinnai, A. Takahara, *Langmuir* **2014**, *30*, 2061-2067.
- [77] G. Cheng, G. Li, H. Xue, S. Chen, J. D. Bryers, S. Jiang, *Biomaterials* **2009**, *30*, 5234-5240.

- [78] A. J. Keefe, N. D. Brault, S. Jiang, *Biomacromolecules* **2012**, *13*, 1683-1687.
- [79] S. Hansson, V. Trouillet, T. Tischer, A. S. Goldmann, A. Carlmark, C. Barner-Kowollik, E. Malmstrom, *Biomacromolecules* **2013**, *14*, 64-74.
- [80] Y. Jiang, Y. Zhang, M. Cao, J. Li, M. Wu, H. Zhang, S. Zheng, H. Liu, M. Yang, *Nanotechnology* **2021**, *32*, 385601.
- [81] A. B. Sánchez-Alvarado, J. Iturbe-Ek, N. Mamidi, A. O. Sustaita, *ACS Appl. Polym. Mater.* **2021**, *3*, 5339-5354.
- [82] S. Wang, Z. Wang, J. Li, L. Li, W. Hu, *Mater. Chem. Front.* **2020**, *4*, 692-714.
- [83] J. O. Zoppe, N. C. Ataman, P. Mocny, J. Wang, J. Moraes, H. A. Klok, *Chem. Rev.* **2017**, *117*, 1105-1318.
- [84] R. Yang, X. Wang, S. Yan, A. Dong, S. Luan, J. Yin, *Prog. Polym. Sci.* **2021**, *118*, 101409.
- [85] J. Baggerman, M. M. J. Smulders, H. Zuilhof, *Langmuir* **2019**, *35*, 1072-1084.
- [86] M. G. F. Hartmuth C. Kolb, and K. Barry Sharpless, *Angew. Chem.* **2001**, *40*, 2004-2021.
- [87] H. Y. Yoon, D. Lee, D. K. Lim, H. Koo, K. Kim, *Adv. Mater.* **2021**, *34*, 2107192.
- [88] X. Zhang, S. Zhang, S. Zhao, X. Wang, B. Liu, H. Xu, *Front. Chem.* **2021**, *9*, 774977.
- [89] J. Kaur, M. Saxena, N. Rishi, *Bioconjugate Chem.* **2021**, *32*, 1455-1471.
- [90] Z. Geng, J. J. Shin, Y. Xi, C. J. Hawker, *J. Polym. Sci.* **2021**, *59*, 963-1042.
- [91] V. D. Bock, H. Hiemstra, J. H. van Maarseveen, *Eur. J. Org. Chem.* **2006**, *2006*, 51-68.
- [92] M. Meldal, *Macromol. Rapid Commun.* **2008**, *29*, 1016-1051.
- [93] J. E. Hein, V. V. Fokin, *Chem. Soc. Rev.* **2010**, *39*, 1302-1315.
- [94] W. Yang, J. Chen, J. Yan, S. Liu, Y. Yan, Q. Zhang, *J. Polym. Sci.* **2022**, *60*, 627-649.
- [95] S. S. v. B. Marjoke F. Debets, Jan Dommerholt, A. (Ton) J. Dirks, Floris P. J. T. Rutjes, and Floris L. van Delft, *Acc. Chem. Res.* **2011**, *44*, 805-815.
- [96] R. Manova, T. A. van Beek, H. Zuilhof, *Angew. Chem.* **2011**, *50*, 5428-5430.

- [97] D. Gahtory, R. Sen, A. R. Kuzmyn, J. Escorihuela, H. Zuilhof, *Angew. Chem.* **2018**, *57*, 10118-10122.
- [98] A. Battigelli, B. Almeida, A. Shukla, *Bioconjugate Chem.* **2022**, *33*, 263-271.
- [99] J. A. P. Nicholas J. Agard, and Carolyn R. Bertozzi, *J. Am. Chem. Soc.* **2004**, *126*, 15046-15047.
- [100] J. M. Baskin, J. A. Prescher, S. T. Laughlin, N. J. Agard, P. V. Chang, I. A. Miller, A. Lo, J. A. Codelli, C. R. Bertozzi, *Proc. Natl. Acad. Sci. USA* **2007**, *104*, 16793-16797.
- [101] X. Ning, J. Guo, M. A. Wolfert, G.-J. Boons, *Angew. Chem.* **2008**, *120*, 2285-2287.
- [102] J. Dommerholt, S. Schmidt, R. Temming, L. J. Hendriks, F. P. Rutjes, J. C. van Hest, D. J. Lefeber, P. Friedl, F. L. van Delft, *Angew. Chem.* **2010**, *49*, 9422-9425.
- [103] J. M. B. Julian A. Codelli, Nicholas J. Agard, Carolyn R. Bertozzi, *J. Am. Chem. Soc.* **2008**, *130*, 11486-11493.
- [104] M. F. Debets, S. S. van Berkel, S. Schoffelen, F. P. Rutjes, J. C. van Hest, F. L. van Delft, *Chem. Commun.* **2010**, *46*, 97-99.
- [105] G. Liu, S. H. Petrosko, Z. Zheng, C. A. Mirkin, *Chem. Rev.* **2020**, *120*, 6009-6047.
- [106] Z. Q. Li, P. Guo, Y. G. Zhou, *Adv. Mater. Technol.* **2021**, *6*, 2000897.
- [107] G. Liu, M. Hirtz, H. Fuchs, Z. Zheng, *Small* **2019**, *15*, 1900564.
- [108] K. A. Brown, D. J. Eichelsdoerfer, X. Liao, S. He, C. A. Mirkin, *Front. Phys.* **2013**, *9*, 385-397.
- [109] J. Z. Richard D. Piner, Feng Xu, Seunghun Hong, Chad A. Mirkin, *Science* **1999**, *283*, 661-663.
- [110] H. Li, Z. Wang, F. Huo, S. Wang, *Chem. Res. Chinese Universities* **2021**, *37*, 846-854.
- [111] M. L. Juntao Xu, Janice L. Huff, Curtis Mosher, Srikanth Vengasandra, Guifu Ding, Eric Henderson, *Biomed. Microdevices* **2004**, *6*, 117-123.
- [112] L. Liang, D. Astruc, *Coord. Chem. Rev.* **2011**, *255*, 2933-2945.
- [113] R. Kumar, A. Bonicelli, S. Sekula-Neuner, A. C. B. Cato, M. Hirtz, H. Fuchs, *Small* **2016**, *12*, 5330-5338.
- [114] S. M. M. Dadfar, S. Sekula - Neuner, V. Trouillet, M. Hirtz, *Adv. Mater. Interfaces* **2021**, *8*, 2002117.

- [115] O. Guselnikova, J. Váňa, L. T. Phuong, I. Panov, L. Rulišek, A. Trelin, P. Postnikov, V. Švorčík, E. Andris, O. Lyutakov, *Chem. Sci.* **2021**, *12*, 5591-5598.
- [116] M. P. S. Chang-Fang Wang, Ermei M. Mäkilä, Maija L. K. Hyvönen, Pirjo M. Laakkonen, Jarno J. Salonen, Jouni T. Hirvonen, Anu J. Airaksinen, Hélder A. Santos, *Biomaterials* **2015**, *48*, 108-118.
- [117] G. Xu, P. Liu, D. Pranantyo, K.-G. Neoh, E.-T. Kang, S. Lay-Ming Teo, *ACS Sustainable Chem. Eng.* **2019**, *7*, 1786-1795.
- [118] L. G. L. Emily Murrell, *ACS Comb. Sci.* **2020**, *22*, 109-113.
- [119] J. T. Ling Chu, Juliana E. Shaw, Felix Rivera-Molina, Anthony J. Koleske, Alanna Schepartz, Derek K. Toomre, *Nat. Commun.* **2020**, *11*, 4271.
- [120] P. Jonkheijm, D. Weinrich, H. Schroder, C. M. Niemeyer, H. Waldmann, *Angew. Chem.* **2008**, *47*, 9618-9647.
- [121] S. Li, G. Li, B. Gao, S. P. Pujari, X. Chen, H. Kim, F. Zhou, L. M. Klivansky, Y. Liu, H. Driss, D. D. Liang, J. Lu, P. Wu, H. Zuilhof, J. Moses, K. B. Sharpless, *Nat. Chem.* **2021**, *13*, 858-867.
- [122] E. Zhang, Y. Shi, J. Han, S. Han, *Anal. Chem.* **2020**, *92*, 15059-15068.
- [123] J. M. Baskin, C. R. Bertozzi, *QSAR Comb. Sci.* **2007**, *26*, 1211-1219.
- [124] B. Josephson, C. Fehl, P. G. Isenegger, S. Nadal, T. H. Wright, A. W. J. Poh, e. J. Bower, A. M. Giltrap, L. Chen, C. Batchelor-McAuley, G. Roper, O. Arisa, J. B. I. Sap, A. Kawamura, A. J. Baldwin, S. Mohammed, R. G. Compton, V. Gouverneur, B. G. Davis, *Nature* **2020**, *585*, 530-537.
- [125] E. M. Sletten, C. R. Bertozzi, *Angew. Chem.* **2009**, *48*, 6974-6998.
- [126] Y. Zhang, K.-Y. Park, K. F. Suazo, M. D. Distefano, *Chem. Soc. Rev.* **2018**, *47*, 9106-9136.
- [127] M. Fernandez-Suarez, H. Baruah, L. Martinez-Hernandez, K. T. Xie, J. M. Baskin, C. R. Bertozzi, A. Y. Ting, *Nat. Biotechnol.* **2007**, *25*, 1483-1487.
- [128] C. R. B. Ellen M. Sletten, *Org. Lett.* **2008**, *10*, 3097-3099.
- [129] A. P. Alexander Kuzmin, Margreet A. Wolfert, Vladimir V. Popok, *Bioconjugate Chem.* **2010**, *21*, 2076-2085.
- [130] C. G. Gordon, J. L. Mackey, J. C. Jewett, E. M. Sletten, K. N. Houk, C. R. Bertozzi, *J. Am. Chem. Soc.* **2012**, *134*, 9199-9208.
- [131] E. M. S. John C. Jewett, Carolyn R. Bertozzi, *J. Am. Chem. Soc.* **2010**, *132*, 3688-3690.

- [132] T. Riedel, F. Surman, S. Hageneder, O. Pop-Georgievski, C. Noehammer, M. Hofner, E. Brynda, C. Rodriguez-Emmenegger, J. Dostálek, *Biosens. Bioelectron.* **2016**, *85*, 272-279.
- [133] H. Lisalova, E. Brynda, M. Houska, I. Visova, K. Mrkvova, X. C. Song, E. Gedeonova, F. Surman, T. Riedel, O. Pop-Georgievski, J. Homola, *Anal. Chem.* **2017**, *89*, 3524-3531.
- [134] H. Vaisocherova-Lisalova, F. Surman, I. Visova, M. Vala, T. Springer, M. L. Ermini, H. Sipova, P. Sedivak, M. Houska, T. Riedel, O. Pop-Georgievski, E. Brynda, J. Homola, *Anal. Chem.* **2016**, *88*, 10533-10539.
- [135] C. J. Huang, N. D. Brault, Y. Li, Q. Yu, S. Jiang, *Adv. Mater.* **2012**, *24*, 1834-1837.
- [136] A. de los Santos Pereira, N. Y. Kostina, M. Bruns, C. Rodriguez-Emmenegger, C. Barner-Kowollik, *Langmuir* **2015**, *31*, 5899-5907.
- [137] A. de los Santos Pereira, T. Riedel, E. Brynda, C. Rodriguez-Emmenegger, *Sens. Actuators B* **2014**, *202*, 1313-1321.
- [138] C. Rodriguez Emmenegger, E. Brynda, T. Riedel, Z. Sedlakova, M. Houska, A. B. Alles, *Langmuir* **2009**, *25*, 6328-6333.
- [139] M. Forinova, A. Pilipenco, I. Visova, N. S. Lynn, Jr., J. Dostalek, H. Maskova, V. Honig, M. Palus, M. Selinger, P. Kocova, F. Dycka, J. Sterba, M. Houska, M. Vrabцова, P. Horak, J. Anthi, C. P. Tung, C. M. Yu, C. Y. Chen, Y. C. Huang, P. H. Tsai, S. Y. Lin, H. J. Hsu, A. S. Yang, A. Dejneka, H. Vaisocherova-Lisalova, *ACS Appl. Mater. Interfaces* **2021**, *13*, 60612-60624.
- [140] A. A. P. Sara V. Orski, Selvanathan Arumugam, Leidong Mao, Vladimir V. Popik, and, J. Locklin, *J. Am. Chem. Soc.* **2010**, *132*, 11024-11026.
- [141] V. Parrillo, A. de los Santos Pereira, T. Riedel, C. Rodriguez-Emmenegger, *Anal. Chim. Acta* **2017**, *971*, 78-87.
- [142] A. R. Kuzmyn, L. W. Teunissen, P. Fritz, B. van Lagen, M. M. J. Smulders, H. Zuilhof, *Adv. Mater. Interfaces* **2022**, *9*, 2101784.
- [143] B. Yang, Y. Wang, M. Vorobii, E. Sauter, M. Koenig, R. Kumar, C. Rodriguez - Emmenegger, M. Hirtz, *Adv. Mater. Interfaces* **2022**, *9*, 2102325.
- [144] C. Rodriguez-Emmenegger, S. Janel, A. de los Santos Pereira, M. Bruns, F. Lafont, *Polym. Chem.* **2015**, *6*, 5740-5751.
- [145] I. Banerjee, R. C. Pangule, R. S. Kane, *Adv. Mater.* **2011**, *23*, 690-718.
- [146] C. Rodriguez-Emmenegger, E. Hasan, O. Pop-Georgievski, M. Houska, E. Brynda, A. B. Alles, *Macromol. Biosci.* **2012**, *12*, 525-532.

- [147] C. Rodriguez-Emmenegger, E. Brynda, T. Riedel, M. Houska, V. Subr, A. B. Alles, E. Hasan, J. E. Gautrot, W. T. Huck, *Macromol. Rapid Commun.* **2011**, *32*, 952-957.
- [148] J. Zempleni, S. S. Wijeratne, Y. I. Hassan, *Biofactors* **2009**, *35*, 36-46.
- [149] C. Liu, H. Wu, Y. Mao, W. Chen, S. Chen, *Cancer Cell Int.* **2021**, *21*, 254.
- [150] R. Loomba, S. L. Friedman, G. I. Shulman, *Cell* **2021**, *184*, 2537-2564.
- [151] B. Sangro, P. Sarobe, S. Hervas-Stubbs, I. Melero, *Nat. Rev. Gastroenterol Hepatol* **2021**, *18*, 525-543.
- [152] M. Pinter, R. K. Jain, D. G. Duda, *JAMA Oncol.* **2021**, *7*, 113-123.
- [153] H. Wu, M. D. Wang, L. Liang, H. Xing, C. W. Zhang, F. Shen, D. S. Huang, T. Yang, *Small* **2021**, *17*, 2005236.
- [154] S. Daher, M. Massarwa, A. A. Benson, T. Khoury, *J. Clin. Transl. Hepatol.* **2018**, *6*, 69-78.
- [155] M. S. Grandhi, A. K. Kim, S. M. Ronnekleiv-Kelly, I. R. Kamel, M. A. Ghasebeh, T. M. Pawlik, *Surg. Oncol.* **2016**, *25*, 74-85.
- [156] N. Tsuchiya, Y. Sawada, I. Endo, K. Saito, Y. Uemura, T. Nakatsura, *World J. Gastroenterol.* **2015**, *21*, 10573-10583.
- [157] M. Vorobii, N. Y. Kostina, K. Rahimi, S. Grama, D. Soder, O. Pop-Georgievski, A. Sturcova, D. Horak, O. Grottke, S. Singh, C. Rodriguez-Emmenegger, *Biomacromolecules* **2019**, *20*, 959-968.
- [158] F. Li, J. Han, L. Jiang, Y. Wang, Y. Li, Y. Dong, Q. Wei, *Biosens. Bioelectron.* **2015**, *68*, 626-632.
- [159] T. Kumada, H. Toyoda, T. Tada, S. Kiriya, M. Tanikawa, Y. Hisanaga, A. Kanamori, J. Tanaka, C. Kagebayashi, S. Satomura, *J. Gastroenterol.* **2014**, *49*, 555-563.
- [160] K. S. Yukari Yamagataa, Kenji Nakamura, Fumiyo Henmia,, S. M. Shinji Satomuraa, Masatoshi Tanakab, *Clin. Chim. Acta* **2003**, *29*, 59-67.
- [161] W. W. Zhu, J. J. Guo, L. Guo, H. L. Jia, M. Zhu, J. B. Zhang, C. A. Loffredo, M. Forgues, H. Huang, X. J. Xing, N. Ren, Q. Z. Dong, H. J. Zhou, Z. G. Ren, N. Q. Zhao, X. W. Wang, Z. Y. Tang, L. X. Qin, Q. H. Ye, *Clin. Cancer Res.* **2013**, *19*, 3944-3954.
- [162] X. Chen, Y. Ba, L. Ma, X. Cai, Y. Yin, K. Wang, J. Guo, Y. Zhang, J. Chen, X. Guo, Q. Li, X. Li, W. Wang, Y. Zhang, J. Wang, X. Jiang, Y. Xiang, C. Xu, P.

- Zheng, J. Zhang, R. Li, H. Zhang, X. Shang, T. Gong, G. Ning, J. Wang, K. Zen, J. Zhang, C. Y. Zhang, *Cell Res.* **2008**, *18*, 997-1006.
- [163] E. G. E. El-Ahwany, L. Mourad, M. M. K. Zoheiry, H. Abu-Taleb, M. Hassan, R. Atta, M. Hassanien, S. Zada, *Arch. Med. Sci.* **2019**, *15*, 1454-1461.
- [164] R. Chaiteerakij, B. D. Addissie, L. R. Roberts, *Clin. Gastroenterol. Hepatol.* **2015**, *13*, 237-245.
- [165] L. Jiang, F. Li, J. Feng, P. Wang, Q. Liu, Y. Li, Y. Dong, Q. Wei, *RSC Adv.* **2016**, *6*, 24373-24380.
- [166] Q. Xie, X. Weng, L. Lu, Z. Lin, X. Xu, C. Fu, *Biosens. Bioelectron.* **2016**, *77*, 46-50.
- [167] L. Chuang, J. Y. Hwang, H. C. Chang, F. M. Chang, S. B. Jong, *Clin. Chim. Acta* **2004**, *348*, 87-93.
- [168] L. Jiang, J. Han, F. Li, J. Gao, Y. Li, Y. Dong, Q. Wei, *Electrochim. Acta* **2015**, *160*, 7-14.
- [169] W. Li, X. Jiang, J. Xue, Z. Zhou, J. Zhou, *Biosens. Bioelectron.* **2015**, *68*, 468-474.
- [170] K. Tawa, F. Kondo, C. Sasakawa, K. Nagae, Y. Nakamura, A. Nozaki, T. Kaya, *Anal. Chem.* **2015**, *87*, 3871-3876.
- [171] J. Li, D. Liu, D. Zhou, L. Shao, X. Chen, H. Song, *Talanta* **2021**, *225*, 122074.
- [172] Y. Wang, G. Zhao, H. Wang, W. Cao, B. Du, Q. Wei, *Biosens. Bioelectron.* **2018**, *106*, 179-185.
- [173] P. Preechakasedkit, W. Siangproh, N. Khongchareonporn, N. Ngamrojanavanich, O. Chailapakul, *Biosens. Bioelectron.* **2018**, *102*, 27-32.
- [174] Z. Luo, Q. Qi, L. Zhang, R. Zeng, L. Su, D. Tang, *Anal. Chem.* **2019**, *91*, 4149-4156.
- [175] M. Heiat, M. Negahdary, *Microchem. J.* **2019**, *148*, 456-466.
- [176] B. Su, Y. Wang, H. Pei, Z. Sun, H. Cao, C. Zhang, Q. Chen, X. Liu, *Anal. Methods* **2020**, *12*, 4742-4748.
- [177] E. Berganza, M. P. Ebrahimkutty, S. K. Vasantham, C. Zhong, A. Wunsch, A. Navarrete, M. Galic, M. Hirtz, *Nanoscale* **2021**, *13*, 12642-12650.
- [178] A. L. Hernandez, S. P. Pujari, M. F. Laguna, B. Santamaria, H. Zuilhof, M. Holgado, *Sensors* **2021**, *21*, 8156.
- [179] B. Sivaraman, R. A. Latour, *Langmuir* **2012**, *28*, 2745-2752.

- [180] I. V. Hana Vaisocherová-Lísalová, Maria Laura Ermini, TomášŠpringer, Xue Chadtová Song, Jan Mrázek, Josefína Lamačová, N. Scott Lynn Jr., Petr Šedivák, Jiří Homola, *Biosens. Bioelectron.* **2016**, *80*, 84-90.
- [181] M. Garay-Sarmiento, L. Witzdam, M. Vorobii, C. Simons, N. Herrmann, A. de los Santos Pereira, E. Heine, I. El-Awaad, R. Lütticken, F. Jakob, U. Schwaneberg, C. Rodriguez-Emmenegger, *Adv. Funct. Mater.* **2021**, *32*, 2106656.
- [182] D. Brunel, V. Jangid, E. Sanchez Adaime, D. Duché, A. K. Bharwal, M. Abel, M. Koudia, T. Buffeteau, C. Lebouin, J. J. Simon, R. M. Sauvage, G. Berginc, L. Escoubas, D. Gigmes, F. Dumur, *Appl. Surf. Sci.* **2021**, *566*, 150731.
- [183] S. Haziza, N. Mohan, Y. Loe-Mie, A.-M. Lepagnol-Bestel, S. Massou, M.-P. Adam, X. L. Le, J. Viard, C. Plancon, R. Daudin, P. Koebel, E. Dorard, C. Rose, F.-J. Hsieh, C.-C. Wu, B. Potier, Y. Herault, C. Sala, A. Corvin, B. Allinquant, H.-C. Chang, F. Treussart, M. Simonneau, *Nat. Nanotechnol.* **2016**, *12*, 322-328.
- [184] I. Rehor, H. Mackova, S. K. Filippov, J. Kucka, V. Proks, J. Slegerova, S. Turner, G. Van Tendeloo, M. Ledvina, M. Hruby, P. Cigler, *Chempluschem* **2014**, *79*, 21-24.
- [185] G. Gao, Q. Guo, J. Zhi, *Small* **2019**, *15*, e1902238.
- [186] U. T. Uthappa, O. R. Arvind, G. Sriram, D. Losic, J. Ho Young, M. Kigga, M. D. Kurkuri, *J. Drug Delivery Sci. Technol.* **2020**, *60*, 101993.
- [187] H. Huang, M. Liu, R. Jiang, J. Chen, L. Mao, Y. Wen, J. Tian, N. Zhou, X. Zhang, Y. Wei, *J. Colloid Interface Sci.* **2018**, *513*, 198-204.
- [188] L. N. Nie, A. C. Damle, V. G. Sharmin, R. Evans, E. P. P. Hemelaar, S. R. van der Laan, K. J. Li, R. Perona Martinez, F. P. Vedelaar, T. Chipaux, M. Schirhagl, R., *Sci. Adv.* **2021**, *7*, eabf0573.
- [189] K. Fox, P. A. Tran, D. W. M. Lau, T. Ohshima, A. D. Greentree, B. C. Gibson, *Mater. Lett.* **2016**, *185*, 185-188.
- [190] H. Lai, M. H. Stenzel, P. Xiao, *Inter. Mater. Rev.* **2019**, *65*, 189-225.
- [191] M. Barzegar Amiri Olia, P. S. Donnelly, L. C. L. Hollenberg, P. Mulvaney, D. A. Simpson, *ACS Appl. Nano Mater.* **2021**, *4*, 9985-10005.
- [192] K. Turcheniuk, V. N. Mochalin, *Nanotechnology* **2017**, *28*, 252001.
- [193] S. Sotoma, F.-J. Hsieh, H.-C. Chang, *J. Chin. Chem. Soc.* **2018**, *65*, 1136-1146.
- [194] J. Vavra, I. Rehor, T. Rendler, M. Jani, J. Bednar, M. M. Baksh, A. Zappe, J. Wrachtrup, P. Cigler, *Adv. Funct. Mater.* **2018**, *28*, 1803406.

- [195] K. Kvakova, M. Ondra, J. Schimer, M. Petrik, Z. Novy, H. Raabova, M. Hajduch, P. Cigler, *Adv. Funct. Mater.* **2022**, 2109960.
- [196] T. Rendler, J. Neburkova, O. Zemek, J. Kotek, A. Zappe, Z. Chu, P. Cigler, J. Wrachtrup, *Nat. Commun.* **2017**, 8, 14701.
- [197] S. Claveau, M. Kindermann, A. Papine, Z. V. Diaz-Riascos, X. Delen, P. Georges, R. Lopez-Aleman, O. M. Tirado, J. R. Bertrand, I. Abasolo, P. Cigler, F. Treussart, *Nanoscale* **2021**, 13, 9280-9292.
- [198] H. Tinwala, S. Wairkar, *Mater. Sci. Eng. C* **2019**, 97, 913-931.
- [199] M. Mumtaz, N. Hussain, S. Salam, M. Bilal, *J. Mater. Sci.* **2022**, 57, 8064-8099.
- [200] S. K. Sarkar, A. Bumb, X. Wu, K. A. Sochacki, P. Kellman, M. W. Brechbiel, K. C. Neuman, *Biomed. Opt. Express* **2014**, 5, 1190-1202.
- [201] L. J. Su, M. S. Wu, Y. Y. Hui, B. M. Chang, L. Pan, P. C. Hsu, Y. T. Chen, H. N. Ho, Y. H. Huang, T. Y. Ling, H. H. Hsu, H. C. Chang, *Sci. Rep.* **2017**, 7, 45607.
- [202] V. K. A. Sreenivasan, E. A. Ivukina, W. Deng, T. A. Kelf, T. A. Zdobnova, S. V. Lukash, B. V. Veryugin, O. A. Stremovskiy, A. V. Zvyagin, S. M. Deyev, *J. Mater. Chem.* **2011**, 21, 65-68.
- [203] L. Marcon, Z. Kherrouche, J. Lyskawa, D. Fournier, D. Tulasne, P. Woisel, R. Boukherroub, *Chem. Commun.* **2011**, 47, 5178-5180.
- [204] A. Krueger, D. Lang, *Adv. Funct. Mater.* **2012**, 22, 890-906.
- [205] P. Karami, S. Salkhi Khasraghi, M. Hashemi, S. Rabiei, A. Shojaei, *Adv. Colloid Interface Sci.* **2019**, 269, 122-151.
- [206] J. Neburkova, J. Vavra, P. Cigler, *Curr. Opin. Solid. St. M.* **2017**, 21, 43-53.
- [207] R. Li, T. Vedelaar, A. Mzyk, A. Morita, S. K. Padamati, R. Schirhagl, *ACS Sens.* **2022**, 7, 123-130.
- [208] H. Lai, M. Lu, F. Chen, J. Lalevée, M. H. Stenzel, P. Xiao, *Polym. Chem.* **2019**, 10, 1904-1911.
- [209] J. Slegerova, M. Hajek, I. Rehor, F. Sedlak, J. Stursa, M. Hruby, P. Cigler, *Nanoscale* **2015**, 7, 415-420.
- [210] H. S. Jung, K. C. Neuman, *Nanomaterials* **2021**, 11, 153.
- [211] E. Roeven, A. R. Kuzmyn, L. Scheres, J. Baggerman, M. M. J. Smulders, H. Zuilhof, *Langmuir* **2020**, 36, 10187-10199.

- [212] A. R. Kuzmyn, A. T. Nguyen, L. W. Teunissen, H. Zuilhof, J. Baggerman, *Langmuir* **2020**, *36*, 4439-4446.
- [213] E. van Andel, S. C. Lange, S. P. Pujari, E. J. Tijhaar, M. M. J. Smulders, H. F. J. Savelkoul, H. Zuilhof, *Langmuir* **2019**, *35*, 1181-1191.
- [214] Y. Shi, M. Liu, K. Wang, H. Huang, Q. Wan, L. Tao, L. Fu, X. Zhang, Y. Wei, *Appl. Surf. Sci.* **2015**, *357*, 2147-2153.
- [215] C. Zhao, L. Li, J. Zheng, *Langmuir* **2010**, *26*, 17375-17382.
- [216] S. Dedisch, F. Obstals, A. los Santos Pereira, M. Bruns, F. Jakob, U. Schwaneberg, C. Rodriguez - Emmenegger, *Adv. Mater. Interfaces* **2019**, *6*, 1900847.
- [217] M. Vorobii, A. de los Santos Pereira, O. Pop-Georgievski, N. Y. Kostina, C. Rodriguez-Emmenegger, V. Percec, *Polym. Chem.* **2015**, *6*, 4210-4220.
- [218] A. I. Lopez-Lorente, *Anal. Chim. Acta* **2021**, *1168*, 338474.
- [219] J. Wu, Y. Qu, Q. Yu, H. Chen, *Mater. Chem. Front.* **2018**, *2*, 2175-2190.
- [220] C. Ananthanawat, T. Vilaivan, W. Mekboonsonglarp, V. P. Hoven, *Biosens. Bioelectron.* **2009**, *24*, 3544-3549.
- [221] K. Nawattanapaiboon, W. Kiatpathomchai, P. Santanirand, A. Vongsakulyanon, R. Amarit, A. Somboonkaew, B. Sutapun, T. Srihirin, *Biosens. Bioelectron.* **2015**, *74*, 335-340.
- [222] X. Tao, X. Chang, X. Wan, Y. Guo, Y. Zhang, Z. Liao, Y. Song, E. Song, *Anal. Chem.* **2020**, *92*, 14990-14998.
- [223] A. Kasry, A. Nicol, W. Knoll, *Appl. Phys. B* **2021**, *127*, 68.
- [224] I.-W. P. Chen, C.-C. Chen, S.-Y. Lin, C.-h. Chen, *J. Phys. Chem. B* **2004**, *108*, 17497-17504.
- [225] K. Gajos, P. Petrou, A. Budkowski, K. Awsiuk, A. Bernasik, K. Misiakos, J. Rysz, I. Raptis, S. Kakabakos, *Analyst* **2015**, *140*, 1127-1139.
- [226] S. Reisewitz, H. Schroeder, N. Tort, K. A. Edwards, A. J. Baeumner, C. M. Niemeyer, *Small* **2010**, *6*, 2162-2168.
- [227] V. Vamvakaki, N. A. Chaniotakis, *Electroanalysis* **2008**, *20*, 1845-1850.
- [228] M. C. Pirrung, *Angew. Chem.* **2002**, *41*, 1276-1289.
- [229] A. Opdahl, D. Y. Petrovykh, H. Kimura-Suda, M. J. Tarlov, L. J. Whitman, *Proc. Natl. Acad. Sci. USA* **2007**, *104*, 9-14.

- [230] A. W. Peterson, R. J. Heaton, R. M. Georgiadis, *Nucleic Acids Res.* **2001**, *29*, 5163-5168.
- [231] S. Watcharinyanon, D. Nilsson, E. Moons, A. Shaporenko, M. Zharnikov, B. Albinsson, J. Martensson, L. S. Johansson, *Phys. Chem. Chem. Phys.* **2008**, *10*, 5264-5275.
- [232] S. M. Schreiner, D. F. Shudy, A. L. Hatch, A. Opdahl, *Anal. Chem.* **2010**, *82*, 2803-2810.
- [233] M. Mrksich, *Chem. Soc. Rev.* **2000**, *29*, 267-273.
- [234] T. N. Ly, S. Park, S. J. Park, *Sens. Actuators B* **2016**, *237*, 452-458.
- [235] G. M. Das, S. Manago, M. Mangini, A. C. De Luca, *Nanomaterials* **2021**, *11*, 2679.
- [236] L. Sun, S. Svedhem, B. Akerman, *Langmuir* **2014**, *30*, 8432-8441.
- [237] Linette M. Demers, C. A. Mirkin, R. C. Mucic, R. A. Reynolds, R. L. Letsinger, R. Elghanian, G. Viswanadham, *Anal. Chem.* **2000**, *72*, 5535-5541.
- [238] M. E. Minaei, M. Saadati, M. Najafi, H. Honari, *Electroanalysis* **2016**, *28*, 2582-2589.
- [239] S. A. Jadhav, *J. Phys. Org. Chem.* **2017**, *30*, e3611.
- [240] S. M. M. Dadfar, S. Sekula-Neuner, U. Bog, V. Trouillet, M. Hirtz, *Small* **2018**, *14*, 1800131.
- [241] J. Escorihuela, M. J. Banuls, R. Puchades, A. Maquieira, *J. Mater. Chem. B* **2014**, *2*, 8510-8517.
- [242] S. M. M. Dadfar, S. Sekula-Neuner, V. Trouillet, M. Hirtz, *Adv. Mater. Interfaces* **2018**, *5*, 1801343.
- [243] J. Escorihuela, M. J. Banuls, S. Grijalvo, R. Eritja, R. Puchades, A. Maquieira, *Bioconjug. Chem.* **2014**, *25*, 618-627.
- [244] R. Kumar, S. Weigel, R. Meyer, C. M. Niemeyer, H. Fuchs, M. Hirtz, *Chem. Commun.* **2016**, *52*, 12310-12313.
- [245] J. Chen, C. Yu, Z. Shi, S. Yu, Z. Lu, W. Jiang, M. Zhang, W. He, Y. Zhou, D. Yan, *Angew. Chem.* **2015**, *54*, 3621-3625.
- [246] S. C. Luo, H. Xie, N. Chen, H. H. Yu, *ACS Appl. Mater. Interfaces* **2009**, *1*, 1414-1419.
- [247] C.-Y. Lee, P.-C. T. Nguyen, D. W. Grainger, L. J. Gamble, D. G. Castner, *Anal. Chem.* **2007**, *79*, 4390-4400.

- [248] D. Y. Petrovykh, H. Kimura-Suda, L. J. Whitman, M. J. Tarlov, *J. Am. Chem. Soc.* **2003**, *125*, 5219-5226.
- [249] C.-Y. Lee, P. Gong, G. M. Harbers, D. W. Grainger, D. G. Castner, L. J. Gamble, *Anal. Chem.* **2006**, *78*, 3316-3325.
- [250] A. S. Yeri, L. Gao, D. Gao, *J. Phys. Chem. B* **2010**, *114*, 1064–1068.
- [251] R. Benters, C. M. Niemeyer, D. Wöhrle, *ChemBioChem* **2001**, *2*, 686-694.
- [252] S. M. D. Paul, D. Falconnet, S. p. Pasche, M. Textor, A. P. Abel, E. Kauffmann, R. Liedtke, M. Ehrat, *Anal. Chem.* **2005**, *77*, 5831-5838.
- [253] J. Movilli, A. Rozzi, R. Ricciardi, R. Corradini, J. Huskens, *Bioconjugate Chem.* **2018**, *29*, 4110-4118.
- [254] Y. Huang, B. B. Stogin, N. Sun, J. Wang, S. Yang, T. S. Wong, *Adv. Mater.* **2017**, *29*, 1604641.
- [255] M. Hirtz, M. Lyon, W. Feng, A. E. Holmes, H. Fuchs, P. A. Levkin, *Beilstein J. Nanotechnol.* **2013**, *4*, 377-384.
- [256] J. Kim, P. Seidler, L. S. Wan, C. Fill, *J. Colloid Interf. Sci.* **2009**, *329*, 114-119.
- [257] J. Ederer, P. Janoš, P. Ecorchard, J. Tolasz, V. Štengl, H. Beneš, M. Perchacz, O. Pop-Georgievski, *RSC Adv.* **2017**, *7*, 12464-12473.
- [258] D. R. Bortz, E. G. Heras, I. Martin-Gullon, *Macromolecules* **2011**, *45*, 238-245.
- [259] L. Xu, F. Yao, J. Luo, C. Wan, M. Ye, P. Cui, Y. An, *RSC Adv.* **2017**, *7*, 4746-4752.
- [260] C. W. M. Füner, P. Koidl, *Appl. Phys. Lett.* **1998**, *72*, 1149-1151.

## Appendix

### Appendix A: List of abbreviations

Abbreviation	Full name
SPT	Surface patterning tool
NLP	Nanolithography platform
SPL	Scanning probe lithography
DPN	Dip-pen nanolithography
$\mu$ CS	Microchannel cantilever spotting
SAM	Self-assembled monolayer
AAC	Alkyne–azide cycloaddition
SPAAC	Strain-promoted alkyne–azide cycloaddition
CuAAC	Copper-catalyzed alkyne–azide cycloaddition
AAPBs	Azide-bearing antifouling polymer brushes
SIP	Surface-initiated polymerization
ATRP	Atomic transfer radical polymerization
RAFT	Reversible addition fragmentation transfer
OCT	Cyclooctyne
MOFO	Monofluorinated cyclooctyne
DIFO	Difluorocyclooctyne
DIBO	Dibenzocyclooctyne
BCN	Bicyclononyne
DBCO/DIBAC	Dibenzoazacyclooctyne
BARAC	Biarylazacyclooctynone
NOFO	Nonfluorocyclooctyne

ALP	Acryless cyclooctyne
DIMAC	Dimethoxyazacyclooctyne
OEGMA	Oligo(ethylene glycol)methyl ether methacrylate
GMA	Glycidyl methacrylate
DMSO	Dimethyl sulfoxide
APTES	(3-Aminopropyl)triethoxysilane
DBCO-Tamra	Dibenzylcyclooctyne-PEG <sub>4</sub> -5/6-tetramethylrhodamine
DBCO-Biotin	Dibenzylcyclooctyne-PEG <sub>4</sub> -biotin conjugate
BCN-FAM	5-Carboxyfluorescein-PEG <sub>3</sub> -BCN
BCN-Biotin	Biotin-PEG <sub>3</sub> -BCN
Rhodamine-NHS	5-(and-6)-carboxytetramethylrhodamine
Anti-AFP	AFP polyclonal antibody
AFP	Alpha-fetoprotein
APTES	(3-Aminopropyl)triethoxysilane
DMF	N,N-dimethylformamide
PBS	Phosphate-buffered saline
BSA	Bovine serum albumin
MEMO	3-Methacryloxypropyltrimethoxysilane
MMA	Methyl methacrylate
BSA-FITC	Bovine serum albumin-FITC
HPMA	N-(2-hydroxypropyl) methacrylamide
AlkMA	N-propargyl acrylamide
AIBN	Azobis(isobutyronitrile)
PBAG	Poly(Bisphenol A-co-epichlorohydrin), glycidyl end-capped

---

DBCO-NHS	Dibenzylcyclooctyne-PEG4-NHS ester
DNA	Deoxyribonucleic acid
Hby	Hybridization
DDI	DNA-directed immobilization
ssDNA	Single-stranded DNA
SA	Streptavidin
FITC	Fluorescein isothiocyanate
Cy3	Cyanine 3
Cy5	Cyanine 5
AF647	Alexa Fluor™ 647
AF488	Alexa Fluor™ 488
Tamra	Tetramethylrhodamine
Ra	Root-mean square roughness
WCA	Water contact angle
AFM	Atomic force microscopy
XPS	X-ray photoelectron spectroscopy

---

## Appendix B: List of Figures

**Figure 1.1.** Applications of modified surfaces.

**Figure 1.2.** Schematic representation of different chemical modification techniques for surface characteristics modulation.

**Figure 1.3.** Schematic drawing of SAMs forming with various reactive terminals. a) Substrate selection, b) substrates pre-treatment, coating with gold or hydroxylation, c) self-assembled process, d) formed SAMs.

**Figure 1.4.** Schematic drawing of the anchoring moieties on plasma treated surfaces (the oxide surface means the surfaces are treated by O<sub>2</sub> plasma or other hydroxylation techniques).

**Figure 1.5.** a) Schematic representations of different biofoulings and their adverse effects on the marine industry. b) Unspecific protein (streptavidin-Cy3) fouling on glass slides, the dot spots are the target area, and the other area are fully covered by the fouling protein (showing in red color).

**Figure 1.6.** Schematic drawing of the three main antifouling strategies.

**Figure 1.7.** Schematic mechanisms of protein repellency of polymer-based antifouling coatings.

**Figure 1.8.** Schematic drawing of “grafting to” and “grafting from” fabrication strategies for surface-grafting polymers.

**Figure 1.9.** Different types of alkyne-azide cycloaddition (AAC) reactions.

**Figure 1.10.** Mechanism scheme of CuAAC.

**Figure 1.11.** Reactivity chart of various strained alkyne reagents for SPAAC.

**Figure 1.12.** Timeline and milestones of development and biosensing applications of  $\mu$ CS-based techniques.

**Figure 1.13.** Schematic diagrams of the mechanisms and processes of scanning probe lithography, a) and b) ink transfer processes in DPN methodology for diffusive molecular inks and liquid inks, respectively; c) surface patterning tool (SPT), d) process of microchannel cantilever spotting ( $\mu$ CS) with a surface patterning tool.

**Figure 1.14.** Schematic representation of the thesis overview.

**Figure 2.1.** Schematic drawing of a) the growth process and chemical binding strategies for coupling to the AAPBs. b) Schemes of capturing arrays spotted by  $\mu$ CS to the polymer brush surface for (c) selective protein coupling. The insets show the DBCO and BCN derivatives used in the site-specific functionalization.

**Figure 2.2.** Static WCA of the surfaces in the sequential growing steps of polymer brushes. a) ATRP initiator, b) poly(OEGMA), c) poly(OEGMA-*b*-GMA), d) poly(OEGMA-*b*-GMA)-N<sub>3</sub>.

**Figure 2.3.** Surface topography of glass-based specimens at various stages within the polymer brush growth process imaged by AFM with tapping mode. a) ATRP initiator, b) poly(OEGMA), c) poly(OEGMA-*b*-GMA), d) poly(OEGMA-*b*-GMA)-N<sub>3</sub>, e) bare glass. Corresponding roughnesses are given in Table 2.1. All scale bars equal 1  $\mu$ m.

**Figure 2.4.** XP Spectrum of SAM initiator at Br 3d region.

**Figure 2.5.** a) XPS characterization at C 1s region of different surfaces, 1) ATRP initiator, 2) poly(OEGMA), 3) poly(OEGMA-*b*-GMA), 4) poly(OEGMA-*b*-GMA)-N<sub>3</sub>. b) XPS characterization at N 1s region of poly(OEGMA-*b*-GMA) before 3) and after 4) azide functionalization. The components result from corresponding chemical species are highlighted in red.

**Figure 2.6.** SPR measurements acquired at  $\lambda = 670$  nm showing unspecific protein adsorption from undiluted human blood plasma on poly(OEGMA) (black), poly(OEGMA-*b*-GMA)-N<sub>3</sub> (red), and biotin-bearing poly(OEGMA-*b*-GMA) brushes (blue).

**Figure 2.7.** Spotting of DBCO-Tamra and BCN-FAM on bare glass and on polymer brushes without azido functionalization. Exposure times are 5 ms for patterns after printing and 1 s for samples after washing, and scale bars are 100  $\mu\text{m}$ .

**Figure 2.8.** Dependence of a) feature size and b) relative fluorescence intensity on humidity of DBCO-Tamra on AAPBs; and c) fluorescent micrographs captured with exposure times of 5 ms on two diverse patterns printed at dwell time of 0.1 s but at two different relative humidity situations, 20% and 70%, respectively; d) the corresponding feature area distribution of the microarray in c) written at relative humidity of 20%. Scale bar is 50  $\mu\text{m}$ .

**Figure 2.9.** Dependence of a) feature dimension and b) relative fluorescence intensity on dwell time of DBCO-Tamra on AAPBs. c) Fluorescent images taken on two microarrays printed at relative humidity of 20% but dwell time of 0.1 and 1.5 s, with exposure time 5 ms. d) The corresponding feature dimension distribution of micropattern in c) written at dwell time 0.1 s. Scale bar is 50  $\mu\text{m}$ .

**Figure 2.10.** Dependence of a) feature size and b) relative fluorescence intensity on humidity of BCN-FAM on AAPBs; and c) fluorescent micrographs captured with exposure time 5 ms on two diverse patterns printed at dwell time of 0.5 s and at two different relative humidity situations, 20% and 70%, respectively; d) the corresponding feature area distribution of the microarray in c) written at relative humidity of 20%. Scale bar is 50  $\mu\text{m}$ .

**Figure 2.11.** Dependence of a) feature dimension and b) relative fluorescence intensity on dwell time of BCN-FAM on AAPBs. c) Fluorescent images taken on two microarrays printed at relative humidity of 20% and dwell time of 0.1 and 0.5 s, with exposure time 5 ms. d) The corresponding feature dimension distribution of micropattern in c) written at dwell time 0.5 s. Scale bar is 50  $\mu\text{m}$ .

**Figure 2.12.** Relationship of the relative fluorescence intensity with the reaction times and temperatures of the DBCO-Tamra microarrays on AAPBs, a) at 25°C, b) at 37°C; c) and d) are the corresponding fluorescent images to a) and b), respectively. Exposure time for images are 5 ms, and scale bars are 50  $\mu\text{m}$ .

**Figure 2.13.** Relationship of the relative fluorescence intensity with the reaction times and temperatures of the BCN-FAM micropatterns on AAPBs a) 25°C, b) at 37°C; c) is the corresponding fluorescent images to a) and b). Exposure times for images are 100 ms, and scale bar is 50  $\mu\text{m}$ .

**Figure 2.14.** Influence of ink concentration on relative fluorescence intensity of a) biotins (linked with DBCO or BCN) immobilized on AAPBs after incubating with streptavidin(SA)-Cy3 at 37°C, 15 min for DBCO-Biotin, and 37°C, 20 min for BCN-Biotin. Printing settings for DBCO-Biotin of humidity was 20% and dwell time was 0.1 s, for BCN-Biotin was 20% and 0.5 s, respectively. b) and c) are the corresponding fluorescent images after incubation of SA-Cy3 for DBCO-Biotin and BCN-Biotin, respectively, and exposure times are 50 ms, and scale bars are 50  $\mu\text{m}$ .

**Figure 3.1.** Schematic representation of a) the AAPBs synthesis progress, b) immobilization of DBCO-NHS ester capture arrays on AAPBs via  $\mu\text{CS}$ , c) AFP detection through direct binding strategy.

**Figure 3.2.** a) Relationship of the relative fluorescence intensity with different reaction times and temperatures of Alexa Fluor647 labeled streptavidin (SA-AF647) incubated on DBCO-NHS ester capture arrays on AAPBs, b) the corresponding fluorescent images at 37°C (right) and 25°C (left) with different reaction intervals, c) the feature size distribution (here denoted by spot diameter) on the sample treated at the optimum condition, 37°C/20 min. Exposure times for images are 1 s. Scale bars are 50  $\mu\text{m}$ .

**Figure 3.3.** Detection of AFP antigen. a) Relationship of the relative fluorescence intensity with different incubation times and temperatures of rhodamine-conjugated AFP on directly immobilized anti-AFP arrays on AAPBs, b) the corresponding fluorescent images with different reaction times at temperatures of 25°C (top) and 37°C (bottom). Exposure times for images are 100 ms. The scale bar is 50  $\mu\text{m}$ .

**Figure 3.4.** Isotype control experiments on IgG antibody functionalized arrays (direct binding regime). a) Coupled with FITC linked 2nd antibody. Images captured at b) red and c) green channel after incubation of AFP-rhodamine on IgG antibody functionalized arrays. Exposure times of the samples are 1 s. Scale bars are 100  $\mu\text{m}$ .

**Figure 3.5.** Negative control experiments on AAPB surfaces. Bright field images of the DBCO-NHS ester arrays on AAPB substrate, a) after printing by  $\mu\text{CS}$ , and b) after washing with PBS. c) Image captured at red channel after incubation of  $\text{NH}_2\text{-PEG}_4\text{-NH}_2$  and AFP-rhodamine sequentially on the sample shown in (a) and (b). The exposure times are 1 ms for a) and b), 100 ms for c). Scale bars are 100  $\mu\text{m}$ .

**Figure 3.6.** Sensitivity evaluation of AFP detection by antibody microarrays on AAPB substrates. The fluorescence intensity was collected on samples incubated with different concentrations of rhodamine labeled AFP, a) was based on the direct binding strategy (NHS/antibody/AFP), b) was based on the indirect binding strategy (biotin/streptavidin/biotin-antibody/AFP). All the reactions were implemented in the optimal situations. The above images are the corresponding fluorescent images concerning different AFP concentrations, and the cartons in the low right corner are the illustrations of the two regimes. c) and d) are the linear fitting curves of the detected fluorescence intensity at low concentrations ( $\leq 100 \mu\text{g/mL}$ ) corresponding to (a) and (b), respectively. The exposure times are 100 ms, the scale bars are 50  $\mu\text{m}$ .

**Figure 4.1.** Schematic illustration of the chemical structure and  $\mu$ CS functionalization strategy of the poly(HPMA-*b*-AlkMA) polymer brushes. a) The fabrication route of the methacrylate-based, alkyne-bearing antifouling polymer brushes. b) Creation of micropatterns by  $\mu$ CS on the reactive polymer brushes surface. c) Selective binding of a target protein to the site-specifically functionalized polymer brushes surface.

**Figure 4.2.** Corresponding static WCA (top) and AFM images (bottom) of glass-based samples. a) Bare glass, b) MMA-silanized, c) poly(HPMA-*b*-AlkMA) modified.

**Figure 4.3.** Corresponding static WCA (top) and AFM images (bottom) of diamond-based samples. a) Bare diamond, b) MMA-silanized, c) poly(HPMA-*b*-AlkMA) modified.

**Figure 4.4.** XPS characterization of different surfaces on glass substrates, a) at C 1s region, b) wide-scan spectra. The components resulting from corresponding chemical species are highlighted in red.

**Figure 4.5.** XPS characterization at N 1s region of poly(HPMA-*b*-AlkMA) surface on glass substrates.

**Figure 4.6.**  $\mu$ CS printed Tamra-azide dots on polymer brush modified glass substrates. Pictures were captured in a) bright field and b) fluorescence (in Cy3 channel, exposure times 55 ms) before the washing step, and c) bright field and d) fluorescence (in Cy3 channel, exposure times 500 ms) after washing. e) Comparison of the fluorescence intensity before and after washing (data was collected on the image (b) and (d)). Taken into account the prolonged exposure time, around one tenth of fluorescent molecules available in the ink immobilized on the polymer brush. Scale bars are 50  $\mu$ m.

**Figure 4.7.** a) Biotin-azide printed dots and b) later incubated with SA-Cy3 after blocking with BSA-FITC. c) Biotin-azide printed dots and d) later incubated with SA-Cy3, but without any blocking step. e) Fluorescence intensity (in Cy3 channel) comparison between the samples blocked and unblocked with BSA-FITC. Exposure times for the fluorescent images are 100 ms. Scale bars are 50  $\mu\text{m}$ .

**Figure 4.8.** Samples (the same ones shown in Figure 4.3) were a) unblocked or b) blocked with BSA-FITC before incubation with SA-Cy3. c) Fluorescence intensity (in FITC channel) comparison between the unblocked and the blocked samples. Exposure times are 1 s for both pictures. Scale bars are 50  $\mu\text{m}$ .

**Figure 4.9.** a) Optical image of  $5 \times 5$  matrices of biotin-azide (on the top left) and Cy5-azide (on the top right), and the pattern ( $10 \times 5$ ) at the bottom part consists of the alternating columns of biotin- and Cy5-azide. b) Cy5-azide arrays shown in Cy5 channel and with exposure time of 400 ms. c) Biotin-azide columns after binding with SA-Cy3 shown in Cy3 channel and with exposure time of 20 ms. d) Merged image by image (b) and (c). Scale bars are 100  $\mu\text{m}$ .

**Figure 4.10.** Fluorescence intensity (in Cy3 channel) of the samples incubated with SA-Cy3 with or without BSA blocking. Samples with a) different thicknesses and b) prepared at different ageing states of the underlying silane layer. The standard deviation was computed from 50 random spaces on unfunctionalized area for background, and 50 SA-Cy3 bound spots for target protein binding.

**Figure 4.11.** Fluorescent images of Alexa488-azide (green) micropatterns on a polymer-brush-coated diamond surface, a) after  $\mu\text{CS}$  printing (exposure time 5 ms), b) after washing (exposure time 500 ms), c) fluorescence intensity collected from image (a) and (b). Taking into account the prolonged exposure time after washing away the excess ink, around 1% of molecules available in the ink are immobilized to the diamond surface. Fluorescent images of SA (FITC conjugate, green) incubated biotin-azide micropatterns on polymer-brush-coated diamond surfaces, d) direct incubation of SA, and e) BSA (non-fluorescent) blocked prior to SA incubation (exposure time 1 s for both), f) fluorescence intensity of background and spotted area collected from image

(d) and (e). Interestingly, on the diamond surfaces BSA blocking even slightly increases the background intensity (through error bars still overlap). Scale bars are 50  $\mu\text{m}$  in all images.

**Figure 4.12.** Fluorescent image (FITC channel of a naked diamond surface (no brush) after incubation with SA-FITC showing a high unspecific adsorption of protein. The fluorescence intensity is  $(6255.96 \pm 561.45)$  a.u. at an exposure time of 1s.

**Figure 5.1.** a) Schematic diagram of the modification processes of DBCO- and PBAG-modified platforms, b) thiolated DNA probe microarrays patterned by  $\mu\text{CS}$  on modified platforms, c) hybridization and protein binding on DNA arrays.

**Figure 5.2.** Recording of static WCA on bare glass, hydroxyl (-OH), DBCO and PBAG platforms for three months after the modification.

**Figure 5.3.** Digital photos of the static WCA on the bare glass,  $\text{NH}_2$ -, DBCO-, Plasma-treated glass (hydroxyl -OH), PBAG- and gold-modified substrates.

**Figure 5.4.** AFM images of modified surfaces for roughness measurement. a) Bare glass,  $0.135 \pm 0.086$  nm; b) DBCO-modified surface,  $0.212 \pm 0.107$  nm; c)  $\text{NH}_2$ -modified surface,  $0.205 \pm 0.109$  nm; d) PBAG-modified surface,  $0.386 \pm 0.143$  nm; e) gold-coated plain surface,  $0.519 \pm 0.172$  nm. All scale bars are equal to 2  $\mu\text{m}$ .

**Figure 5.5.** XP spectra of different modified surface. a) XP wide spectrum of bare glass surface, b) high-resolution XP spectra at N 1s region of aminated-(bottom), PBAG-modified (middle), and DBCO-modified (top) surfaces, c) high-resolution XP spectra at C 1s region of aminated-(bottom), PBAG-modified (middle), and DBCO-modified (top) chips, d) high-resolution XP spectra at Au 4f region of gold-coated surface.

**Figure 5.6.** Hybridization of the target T2-Cy3 (red) with the probe PT2 dot arrays on different platforms, a) on PBAG surface, b) on DBCO surface, c) on gold surface (image captured in air), and d) on gold surface (image captured in PBS solution). e) Histogram of feature size (denoted by spot diameter) in DNA detection array on samples in image (a), (b) and (d). f) Summary of the relative fluorescence intensity (hybridized spots and background) collected on images (a), (b) and (d), respectively. The exposure times of the images are 1 s, and scale bars are equal to 100  $\mu\text{m}$ .

**Figure 5.7.** Fluorescent images of oligonucleotide arrays (PT2-FITC, green, left side) hybridized with fluorophore-tagged target oligomer T2-Cy3 (red, right side) on gold coated chips covered with a drop of PBS solution at a) pH 2, b) pH 7.4, c) pH 14, respectively; d) fluorescence intensities collected at green and red channels on pictures (a), (b) and (c), respectively. The exposure times are 1 s, and scale bars are 100  $\mu\text{m}$ .

**Figure 5.8.** Control experiments on bare glass substrate. a) Freshly printed PT1-FITC (green) array, b) the same sample after washing with PBS, c) the sample after incubation with T1-Cy3. The exposure times of a) is 300 ms, and of b) and c) are 1 s. Scale bars are 100  $\mu\text{m}$ .

**Figure 5.9.** Hybridization (Hyb) of two ssDNA targets one after another probe arrays containing long DNA sequences. a) Schematic drawing of hybridization protocol for image (b) and (c). The ssDNA targets b) T1-Cy3 (red) and c) T2-Cy5 (magenta) were incubated on PBAG-modified substrate after immobilization of PT1+P2 on the surface. d) Schematic drawing of hybridization protocol for image (e) and (f). Hybridization of e) T1 and f) T2 Cy3 (red) with the PT1+P2-FITC (green) probe array on DBCO-modified surface. g) Summary of the relative fluorescence intensity (spot area and background) collected on images (b) and (f). The exposure times are 1 s, and scale bars are 100  $\mu\text{m}$ .

**Figure 5.10.** Fluorescence images captured on PT1+P2-FITC (green) immobilized arrays on a) PBAG-treated and b) DBCO-terminated chips after hybridization with T1 and T2-Biotin. Incubation of SA-Cy3 (red) on c) PBAG substrate, and on d) DBCO substrate after hybridization with T1 and T2-Biotin. e) Schematic drawing of DNA hybridization and protein binding protocols. f) The relative fluorescence intensity probe (green) and streptavidin (red) collected on picture (a), (b), (c) and (d), respectively. The exposure times are 1 s, and scale bars are 100  $\mu\text{m}$ .

**Appendix C: List of Tables**

**Table 2.1.** Static water contact angle, thickness and roughness reports of the films of the surfaces.

**Table 4.1.** Summary of physical characterization (WCA, roughness and thickness) of the film coatings. Every mean value with standard deviation was counted from 3 random measurements.

**Table 5.1.** Static WCA, roughness, and ellipsometric thickness reports of different platforms (mean  $\pm$  standard deviation).

**Table 7.1.** List of materials and chemicals. All chemicals were used as received and without any further purification processes unless specified.

**Table 7.2.** Sequence of oligonucleotides.